TECHNISHE UNIVERSITÄT MÜNCHEN

Fakultät für Elektrotechnik und Informationstechnik
Lehrstuhl für Biologische Bildgebung

Silicon Photonics Sensors of Ultrasound for Optoacoustic Imaging

Rami Shnaiderman

Vollständiger Abdruck der von der Fakultät für Elektrotechnik und Informationstechnik der Technischen Universität München zur Erlangung des akademischen Grades eines

Doktor-Ingenieurs

genehmigten Dissertation.

Vorsitzender: Prof. Dr. Marc Tornow

Prüfer der Dissertation:

1. Prof. Dr. Vasilis Ntziachristos
2. Prof. Dr. Bernhard Wolfrum

Die Dissertation wurde am 29.09.2020 bei der Technischen Universität München eingereicht und durch die Fakultät für Elektrotechnik und Informationstechnik am 09.04.2021 angenommen.

To my family and friends

Abstract

Optoacoustic (Photoacoustic) imaging is an imaging method insensitive to photon scattering, enabling deep imaging inside tissues. This approach resolves the absorption of light based on the detection of ultrasound waves emitted from absorbers. Raster-scan optoacoustic mesosocpy (RSOM) uses ns-lasers and wide-field illumination to excite ultrasonic signals from multiple absorbers in tissue. Signal detection is done by scanning the ultrasound sensor over the sample and recording the signals in multiple positions, followed by image reconstruction algorithms.

RSOM offers penetration depth of several millimeters with resolutions of several tens of micrometers. The latter is often limited by the frequency response and the dimensions of the sensors' aperture. Improvement of the resolution requires point-like ultra-broadband ultrasound sensors, yet piezoelectric sensors traditionally employed in ultrasonography, and optoacoustic imaging loses sensitivity quadratically with size reduction. With apertures under few squares millimeter, piezoelectric sensors are no longer sufficiently sensitive for optoacoustic imaging.

Optical micro-fabricated ultrasound sensors such as polymer micro-ring resonators were demonstrated to attain high sensitivity with apertures of ~ 60 micrometers in diameter. Their sensitivity can be attributed to the large photo-elastic constants and the low Young's modulus of the polymer. At smaller sizes polymer sensors loose sensitivity because they cannot adequately confine light due to the low refractive index contrast of this platform (< 0.5).

In this thesis, we use the widely available silicon photonics platform for sensor miniaturization. This platform utilizes the silicon-on-insulator (SOI) wafers, which offer particularly high refractive index contrast (≈ 2.5). Our novel resonator design, the silicon waveguide-etalon detector (SWED), exploits the sub-micron light confinement in the cross-section of a rectangular silicon waveguide to achieve sensor aperture of 220 × 500 square nanometers. The low photo-elastic coefficients of

silicon are mitigated by directly exposing the optical mode in the waveguide to ultrasound. We study the effects of design and process variations on the sensor performance and perform full characterization of the sensor by exposing it to an ultrasonic point source. The SWED provides per area sensitivity that is 10^4 –fold higher than polymer micro-rings and 10^8 –fold higher than piezoelectric sensors. We demonstrate large bandwidth reaching 230MHz and the ability to shift it on-demand by more than 80MHz without reducing the relative sensitivity of each SWED in the respective frequency band.

We conduct the first ever reported imaging with a silicon photonics ultrasound sensor. The achieved lateral resolution of 16 μm, and axial resolution of 5 μm in RSOM is 2– and 6–fold better than that achieved by piezoelectric sensors. We also exploit the sub-micron aperture to perform the first-ever reported near-filed optoacoustic imaging, reaching acoustic λ/50 super-resolution, which is comparable to the resolution achieved by a high-end optical microscope with a 60× / NA=1.2 objective.

The demonstrated technology is suitable for manufacturing of low-cost ultra-dense sensor arrays, which can revolutionize ultrasonography and optoacoustic imaging.

Zusammenfassung

Optoakustische (Photoakustische) Bildgebung ist ein Bildgebungsverfahren, welches aufgrund der Unabhängigkeit von optischer Streuung große Tiefenabbildung in Gewebe ermöglicht. Diese Methode erfasst optische Absorption durch die Detektion von Ultraschallwellen, welche von Absorbern emittiert werden. Raster-Scan Optoakustische Mesosokpie (RSOM) verwendet ns-Laser und Weitfeldbeleuchtung für die Anregung von Ultraschallwellen mehrerer Absorber im Gewebe. Die Signaldetektion basiert auf dem Abrastern der Probe mit einem Ultraschalldetektor und der Aufzeichnung der Signale an mehreren Position gefolgt von Algorithmen zur Bildrekonstruktion.

RSOM bietet tiefe Bildgebung von mehreren Millimetern mit einer räumlichen Auflösung von einigen zehn Mikrometern. Letzteres ist meist durch die Frequenzantwort und die Abmessungen der Detektorapertur limitiert. Die Verbesserung der Auflösung benötigt Punktquellen-Ultrabreitband-Ultraschall Sensoren, doch die Sensitivität piezoelektrische Sensoren, wie typischerweise in Ultraschallsonographie und optoakustischer Bildgebung verwendet, verringert sich quadratisch mit der Verkleinerung. Bei Aperturen unterhalb weniger Quadratmillimeter werden piezoelektrische Sensoren nicht mehr ausreichend sensitiv für optoakustische Bildgebung.

Mikro-fabrizierte optische Ultraschallsensoren, wie etwa Polymer Mikroring Resonatoren, wurden bereits mit einer hohen Sensitivität bei Aperturen von ~60 Mikrometer Durchmesser gezeigt. Deren Sensitivität kann den hohen photo-elastischen Konstanten und dem geringen Polymer-bedingten Young's Modul zugerechnet werden. Bei kleinen Dimensionen verlieren Polymersensoren Sensitivität, da sie Licht durch den niedrigen Brechungsindex-Kontrast (<0.5) nicht adäquat eingrenzen können.

In dieser Arbeit verwenden wir die weit verfügbaren Silizium-Photonik Plattform zur Sensorminitiasierung. Diese Plattform verwenden einen Silizium-auf-Isolator (SOI) Wafer, der sich insbesondere durch einen hohen Brechungsindex-Kontrast (~2.5) auszeichnet. Unser neuartiges Resonatordesign, der Silizium-Wellenleiter-Etalon Detektor (SWED), erzielt die sub-Mikrometer Eingrenzung von Licht im Querschnitt des rechteckigen Silizium-Wellenleiters aus

um eine Sensorapertur von 220 × 500 quadratnanometern zu erhalten. Den niedrigen photo-elastischen Koeffizienten von Silizium wird durch die direkte Umwandlung der optischen Mode im Wellenleiter zu Ultraschall entgegengewirkt. Wir untersuchten die Effekte von Design und Prozessierungsvariationen auf die Sensorleistungsfähigkeit und führten eine vollständige Charakterisierung des Sensors im Vergleich zu Ultraschall Punktquellen Sensoren durch. Die Sensitivität pro Fläche von SWED liegt 10^4-fach höher als Polymer Mikroringe und 10^8-fach höher als Piezoelektrische Sensoren. Wir zeigen große Bandbreiten mit bis zu 230 MHz und der Möglichkeit diese auf Verlangen um mehr als 80 MHz zu verschieben, ohne dabei die relative Sensitivität der einzelnen SWED im dazugehörigen Frequenzband zu verringern.

Wir demonstrieren die allerste Bildgebung mit einem Silizium-Photonik Ultraschall Sensor. Die erreichte laterale Auflösung lag bei 16 µm, die axiale bei 5 µm, und damit 2- bzw. 6-fach besser als die der piezoelektrischen Sensoren. Darüberhinaus haben wir die sub-Mikrometer Apertur ausgenutzt, um zum ersten Mal Nahfeld-optoakustische Bildgebung durchzuführen und erreichten akustische λ/50 Hochauflösung, was vergleichbar mit der Auflösung hochwertiger optischer Mikrosope mit einem 60× / NA=1.2 Objektiv ist.

Die hier gezeigte Technologie eignet sich zur Fertigung kostengünstiger ultradichter Sensor-Arrays, was sowohl Ultraschallsonographie als auch optoakustischer Bildgebung revolutionieren kann.

Contents

Acknowledgements

This work would not have been possible without the guidance and support of several individuals who accompanied me during the last years and contributed their knowledge and assistance.

First and foremost, I would like to thank my supervisor Prof. Vasilis Ntziachristos who accepted me into his group and let me take part in groundbreaking research. Prof. Ntziachristos always encouraged me to think outside of the box and gave me the freedom to pursue unconventional scientific approaches. He showed me how to see a solution through the grid of traditional scientific disciplines. The experience I gained in the last years is invaluable.

Special thanks go to the following people:

Dr. Georg Wissmeyer – We shared an office and a lab for many years. I cherish the fruitful discussions we shared. The mutual work we did would not have been possible without his contribution.

Okan Ülgen – Despite joining this research at a later stage his contribution to this work was immense. His determination and resourcefulness helped to evolve this technology from a prototype to an application. I am thankful for working with him and look forward to many more fruitful projects.

Qutaiba Mustafa – For crucial contributions to this project enabling visualization of the measurements. He helped from keen scientific interest and I always have pleasure discussing science with him.

Dr. Andriy Chmyrov - For his patience and the open door, he is always ready to hear me out and give a knowledgeable advice. Dr. Chmyrov offered invaluable assistance that helped to elevate this research and achieve pioneering results.

Dr. Christian Zakian - His sincere scientific and moral support made it possible for this research to see the light of day.

Tai Anh La – My newest colleague, his unconditional assistance supported the whole group during the last stages of this work. His insightful questions always make me think and not to take things for granted.

Dr. Murad Omar, Dr. Stephan Kellenberger. Dr. Ludwig Prade, Dr. Dominik Soliman, and Dr. Markus Seeger are all accomplished scientists and talented engineers. Their assistance during the last years contributed in countless aspects to this work. It was a pleasure working with you and will always be a pleasure to have a beer with you.

I would also like to thank my colleagues at the institute of biological and medical imaging (IBMI), Helmholtz Zentrum München (HMGU), and Translatum: Ivan Olefir, Dr. Juan Pablo Werner, Dr. Hailong He, Andrei Berezhnoi, Zak Ali, Yuanhui Huang, Jaber Malekzadeh, Sarah Glasl, Uwe Klemm, Pia Anzenhofer, Mehdi Seyedebrahimi, Dr. Lukas Riobo, and Antonios Stylogiannis.

I would like to thank the entire administrative group of IBMI and Translatum. Especially Dr. Andreas Hillmair and Susanne Stern, my work on this project would not be possible without your support during these years, that often extended past the working relationship. Many thanks also to Lidia Seidl, Dr. Robert Wilson, Dr. Bettina Lehman, and Dr. Rolad Boha for continues support.

Many thanks and appreciation go to Dr. Chapin Rodriguez, your couching helped me to understand the strengths and weaknesses of my work, allowing me to communicate my research in a meaningful way.

My thanks also go to Prof. Georg Sergiadis and Prof. Daniel Razansky for helping me in difficult times. From Prof. Razansky group I would especially like to thank:

Dr. Xosé Luís Deán-Ben – For sharing with me from his vast knowledge and experience.

Dr. Hector Estrada – For helping to understand many theoretical aspects of this work. His door was always open and he was always happy to discuss science.

Dr. Johannes Rebling – For always be willing to share and assist in lab work.

List of figures

List of tables

List of abbreviations

π-FBG	π-phase shifted fiber Bragg grating
π-WBG	π-phase shifted waveguide Bragg grating
2D / 3D	2-dimensional / 3-dimensional
CMUT	Capacitive micromachined ultrasound transducer
CMT	Coupled-mode theory
CW	Continuous wave
FF	Far-field
FOV	Field of view
FWHM	Full width half maximum
IVUS	Intravascular ultrasound
MIP	Maximum intensity projection
MM	Multimode
NA	Numerical aperture
NF	Near-field
NEP	Noise equivalent pressure
PM	Polarization maintaining
RSOM	Raster-scan optoacoustic mesoscopy
SM	Single-mode
SNR	Signal-to-noise ratio
SOI	Silicon-on-insulator
SWED	Silicon waveguide etalon detector

1. Introduction

1.1 Biomedical imaging

Biomedical imaging is an essential tool for basic research and clinical diagnosis. Imaging takes critical role in drug discovery, monitoring disease progress, and discovery of new pathological features that help to better understand the disease and develop ways to cure or manage it. The different imaging modalities are based on different physical phenomena that define the contrast of the image. For example: attenuation of X-rays (X-ray imaging), relaxation properties of hydrogen atoms when excited with pulses of radio waves (Magnetic resonance imaging), ultrasound reflection from interfaces with different acoustic impedance (ultrasonography), reflection and absorption of photons (optical microscopy). The usability of a certain modality does not depend only on the imaging contrast but also on the spatial resolution, axial resolution, imaging depth, and toxicity (the permissible amount of energy that does not harm the tissue). Generally, there are tradeoffs between all of those parameters and optimization of one often means sacrifice of the other. **Figure 1.1** depicts current biomedical imaging modalities as a function of penetration depth and resolution [1]. An open gap is visible (**'The gap'; Fig. 1.1**) for resolutions better than 100 µm and penetration depths higher than 0.5 mm.

The optical regime of the electromagnetic spectrum is very interesting for probing medical information as visible light interact with the outer electrons of the molecules which determine the chemical properties. The short wavelengths of the visible spectrum can be focused to sub-micron diffraction limited spots, interrogating the tissue with high resolution and potentially closing the gap. However, light is scattered by microscopic structures and the high resolution can only be maintained for superficial depth of few hundreds of microns [1]. The penetration limit of such optical microscopy systems can be calculated from the transport mean free path (TMFP) which is defined as the mean propagation distance that it takes for photons to loose relation to the

propagation direction they had before entering the tissue and become diffusive [1]. For example, the TMFP of a human breast tissue is on the order of 0.8 mm.

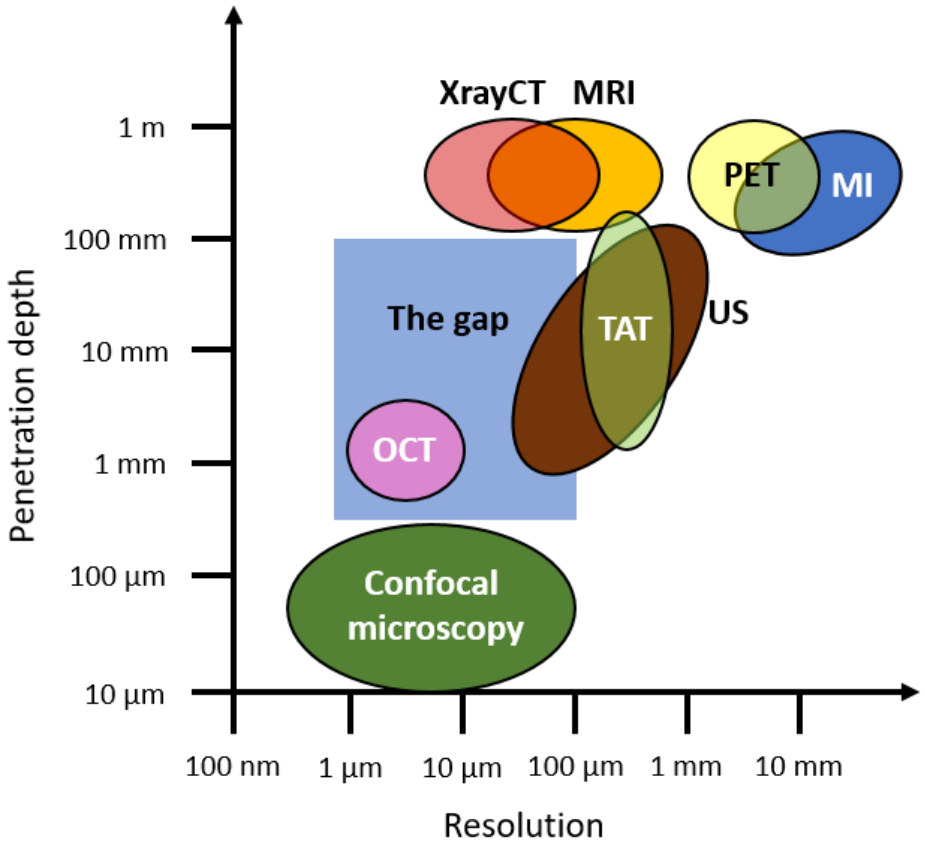

Figure 1.1 Modern biomedical imaging modalities: OCT - Optical Coherence Tomography; X-ray CT - X-ray Computed Tomography; US - Ultrasound; OAT - Optoacoustic Tomography; TAT - Thermoacoustic Tomography; MRI - Magnetic Resonance Imaging; PET - Positron Emission Tomography; MI - Microwave Imaging.

Such gaps as the gap in **Fig. 1.1** are usually covered by combining two adjacent technologies. In recent years optoacoustic tomography [2] and mesoscopy [3] were developed by combining the optical and acoustic modalities, enable imaging at depths larger than 10 × TMFP with resolutions of 30-200 µm. The principal of operation is based on resolving the origin of high frequency ultrasound waves (between few to hundreds of megahertz), generated by thermoelastic expansion of the absorbers in response to short nanosecond light pulses propagating through the tissue. The resolution is determined by the ability to resolve the ultrasound waves therefore it strongly depends on the bandwidth and the aperture of the ultrasound sensors. In addition, it is no longer limited by the optical scattering but by the frequency dependent attenuation of ultrasound, therefore it drops

with depth, but at much slower rate compared to optical microscopy. The main difference between optoacoustic tomography and mesoscopic is in the detection geometry and the ultrasound sensors applied. In tomography the detectors are usually placed on a circle around the object, this configuration is physically achieved by using sensor arrays similar to what is used in ultrasonography. The large number of sensors requires complex signal acquisition systems and the sensitivity requirements dictate large element size, both limit the bandwidth of the sensors to 10-20 MHz resulting in resolutions of 100 – 500 μm with penetration depths larger than 10 × TMFP. This modality is mostly suitable for full body imaging of small animals or ex vivo organs. In mesoscopy (also known as raster scan optoacoustic mesoscopy) a single high-frequency sensor is scanned over the object in a 2D plane. Because only a single channel is acquired and the distance of the sensor from the object can be arbitrary close there are no restrictions on the sensor performance or size. This modality is very successful in applications where access to the object is not available from all sides, and is already implemented in clinical diagnostics [4], [5].

1.2 Thesis objectives

The first objective of this work was to develop sensitive and wide bandwidth optical ultrasound sensors for ultrasonography and optoacoustic imaging using silicon-photonics integrated circuits (PICs), also known as the silicon-on-insulator (SOI) platform. The silicon photonics platform is particularly attractive because it exploits the high-throughput fabrication techniques that are widely used by the semiconductor industry, allowing easy scalability to large sensor arrays with typical cost of only few USD/mm^2. In addition, the availability of on-chip photodetectors [3], modulators [6], and light sources [7] that are completely compatible with the manufacturing processes of the sensors can lead in the future to a compact and monolithic powerful tool for basic research and diagnostics. Other optical sensors reported in the literature require complex and expensive techniques that are not suitable for mass production and are rarely available outside of specialized research facilities. In order to achieve this goal, it was required to study how process variations effect the performance of the PIC sensors and which design parameters (waveguide thickness, different claddings, strength of Bragg gratings, etc.) give the optimal performance. Full acoustic characterization of the sensors was done, this required development of new methods of high frequency sensors charecterization with ultrasonic point sources. Next, the silicon photonics clean-

room technology had to be successfully translated into a 'dirty' biomedical lab, and be compatible with various imaging systems (robustness, bio-computability, footprint) this required extensive development of the silicon chip connectorization, packaging, and optimization of the sensor interrogation system.

The second objective was to improve the resolution of raster-scan optoacoustic mesoscopy by exploiting the strong light confinement in the silicon photonics platform to minimize the sensor aperture and increase the detection bandwidth over state-of-the-art piezoelectric sensors. The intent was to prove that silicon photonics is sufficiently mature to be used unconventionally (outside the context of optical communications) for new applications and it has the potential to close the imaging gap even tighter (**Fig. 1.1**).

The third objective, defined only at a late stage of this work, was to demonstrate that the sub-micron aperture of the new sensor can achieve super-resolution in the near-field. It was achieved by developing a new imaging modality, the near-field scanning optoacoustic microscopy (NSOAM). In contrast to the optical analogy (near-field scanning optical microscopy) that offers optical reflection contrast, or the acoustic near-field microscopy that offers elastic contrast, NSOAM offers optical absorption contrast by sensing the evanescent field of absorbers with optical resolution.

1.3 Thesis outline

In **chapter 2** we describe the governing equations of the optoacoustic effect and ultrasonic propagation in tissue. We describe the pressure field generated by an ideal spherical absorber and correlate the size of the absorber to the pressure frequency and amplitude, which is an important property of optoacoustic imaging. We continue by describing the raster-scan optoacoustic mesoscopy and the effect of different detection geometries on image resolution. Followed by a discussion of common ultrasound sensors employed in optoacoustic imaging and how their performance effects image resolution.

In **chapter 3** we present some basic photonic components of the SOI platform, we discuss different variants and how the properties of each variant can be used in assembling large scale PICs with different functionality. We proceed by discussing the basic properties of Bragg and π-phase shifted

Bragg gratings with examples of such gratings implemented in silica fibers (π-phase shifted fiber Bragg gratings or π-FBGs) and SOI PICs (π-waveguide Bragg grating or π-WBGs). Later we characterize 16 π-WBG sensors manufactured during this study on 4 SOI chips. We examine the effects of design and process variations on the performance of the π-WBGs and compare the results to theoretical predictions. A commercial π-FBG and the manufactured π-WBG are used for ultrasound sensing. We experimentally characterize the sensors and derive theoretical models explaining the difference in performance of each platform, focusing on sensitivity, sensor size, frequency response, and bandwidth.

In **chapter 4** we introduce a new SOI-based sensor, the silicon waveguide-etalon detector (SWED). We develop a new concept of ultrasound sensing, by utilizes the sub-micron light confident in the cross-section of a rectangular waveguide. We demonstrate dramatic miniaturization of the sensor's aperture in comparison to 'traditional' design like micro-rings and π-WBG resonators. We characterize the sensitivity, bandwidth, and size of the SWED aperture and compare its performance to that of the π-FBG and π-WBG sensors. We perform raster-scan optoacoustic mesoscopy with the SWED of vasculature mimicking phantoms, and characterize the resolution achieved with the sensor.

In **chapter 5** we experimentally demonstrate that the SWED can achieve λ/50 acoustic super-resolution when imaging in the near-field. We use this approach to develop the novel near-field scanning optoacoustic microscopy (SNOAM), and proceed by imaging vasculature mimicking phantoms with a resolution of 650 nm.

In **Chapter 6** we discuss in depth the design and manufacturing methods of the π-WBG and the SWED sensors. We continue by describing the various systems developed during this work and used for characterization of the π-FBG, π-WBG, and SWED sensors, and imaging with the SWED sensor.

2. Optoacoustic imaging

The goal of this chapter is to provide brief introduction to the theoretical principles of optoacoustic imaging. This chapter focuses on the raster-scan optoacoustic mesoscopy and describe how sensor properties effect image resolution.

2.1 The optoacoustic effect

In optoacoustic imaging pulsed lasers are used to irradiate the object, the absorbed light by the object is converted to heat which in turn is converted to pressure. The pressure propagates away from the object as an ultrasonic wave [8]. In this chapter we discuss the mechanisms responsible for this effect, and investigate the amplitude and frequency emitted from an ideal spherical absorber.

Laser heating and initial pressure

When the object or a region with a characteristic dimension d_c is illuminated by a laser with pulse duration τ_L, the absorbed energy will increase the temperature of the object and induce thermal expansion of the volume V. The local fractional volume expansion of the heated object can be expressed as:

$$dV/V = -\kappa p + \beta T \qquad (2.1.1)$$

Where p is the change in pressure (pa), T is the change in temperature (Kelvin), β is the thermal coefficient of volume expansion (K^{-1}), and κ is the isothermal compressibility. The absorbed energy will propagate by heat diffusion and pressure propagation. The characteristic thermal diffusion time can be calculated from:

$$\tau_{th} = d_c^2/\alpha_{th} \qquad (2.1.2)$$

Where α_{th} is the thermal diffusivity, typically 0.1 mm^2/s for biological tissue, and d_c is the heated volume. The characteristic stress relaxation time can be calculated from [9]:

$$\tau_{st} = d_c/v_s \tag{2.1.3}$$

Where v_s is the speed of sound. When the laser pulse duration is $\tau_L < \tau_{st} < \tau_{th}$, the heat conduction and stress propagation during the laser pulse are negligible and the laser excitation is said to be in both thermal and stress confinement. In such case the fractional volume expansion is negligible as well and the energy is immediately converted to pressure. This initial pressure (p_0) can be calculated from **Eq. 2.1.1**:

$$p_0 = \beta T/\kappa \tag{2.1.4}$$

If all the absorbed optical energy is converted into heat the temperature rise can be expressed in terms of optical absorption and fluence [8]. Thus the initial pressure can be expressed as:

$$p_0 = \Gamma \mu_a \phi \tag{2.1.5}$$

Where μ_a is the optical absorption coefficient, ϕ is the optical fluence, and Γ is the Grueneisen parameter that is defined as:

$$\Gamma = \frac{\beta}{\kappa \rho C_v} = \frac{\beta v_s^2}{C_p} \tag{2.1.6}$$

Where ρ is the density, C_v and C_p are the specific heat capacities at constant pressure and volume. **Eq. (2.1.5)** can be used to estimate the maximum initial pressure emitted from absorbers when illuminated by the maximum permissible fluence in accordance with safety regulations. The maximum permissible visible-light laser fluence for human skin is defined by the American national standards institute (ANSI) to be 20 mJ/cm. Assuming fluence at this limit and that all of the light is absorbed by subcutaneous 100 % oxygenated blood vessels with μ_a = 100 cm^{-1} [10] and Γ = 0.14 [11] we get p_0 = 308 KPa. This value does not take into account diffraction and attenuation during propagation of the ultrasound from the absorber to the detector. In practice ultrasound sensors employed in optoacoustic imaging required to detect pressures lower than 100 Pa.

Pressure field in space and time

A more careful analysis that considers both pressure generation and propagation is described by the photoacoustic equation [9]:

$$\left(\nabla^2 - \frac{1}{v_s^2}\frac{\partial^2}{\partial t^2}\right)p(\vec{r},t) = -\frac{\Gamma}{v_s^2}\frac{\partial H(\vec{r},t)}{\partial t} \tag{2.1.7}$$

$p(\vec{r},t)$ donated the acoustic pressure at time t and location $\vec{r}$ and $H(\vec{r},t)$ denotes the heating function which is the thermal energy conversion per unit volume per unit time. The left side is the well-known acoustic wave equation and the right side is the side of the pressure source term. If the durations of the laser is of the order of few nanoseconds and the excitation is both in stress and thermal confinement the heating function can be written as:

$$H(\vec{r},t) = \mu_a(\vec{r})\phi(\vec{r})\delta(t) \tag{2.1.8}$$

In order to solve **Eq. 2.1.7** and find the pressure at any location in space and time we use the Green function approach. The green function is defined as the response of the differential equation to impulse source term at time t' and location $\vec{r}'$:

$$\left(\nabla^2 - \frac{1}{v_s^2}\frac{\partial^2}{\partial t^2}\right)G(\vec{r},t;\vec{r}',t') = \square G(\vec{r},t;\vec{r}',t') = -\delta(\vec{r}-\vec{r}')\delta(t-t') \tag{2.1.9}$$

Where $\square$ is the d'Alembert operator. The Green function of this operator is well known:

$$G(\vec{r},t;\vec{r}',t') = \frac{\delta(t-t'-|\vec{r}-\vec{r}'|/v_s)}{4\pi|\vec{r}-\vec{r}'|} \tag{2.1.10}$$

And it represents an impulse diverging spherical wave. Using the Green function, the general solution to **Eq. 2.1.7**:

$$p(r,t) = \int_V \int_t G(\vec{r},t;\vec{r}',t')\frac{\Gamma}{v_s^2}\frac{\partial H(\vec{r},t)}{\partial t}d\vec{r}'dt' \tag{2.1.11}$$

Substituting **Eq. 2.1.10** into **Eq. 2.1.11** and using the definition of the delta function we get:

$$p(r,t) = \frac{\Gamma}{4\pi v_s^2}\frac{\partial}{\partial t}\int_V \frac{1}{|\vec{r}-\vec{r}'|}H\left(\vec{r},t-\frac{|\vec{r}-\vec{r}'|}{v_s}\right)d\vec{r}' \tag{2.1.12}$$

Using **Eq. 2.1.5** and **Eq. 2.1.8** we can express the pressure as a function of the initial pressure:

$$p(\vec{r},t) = \frac{1}{4\pi v_s^2}\frac{\partial}{\partial t}\left[\int_V \frac{1}{|\vec{r}-\vec{r}'|}p_0(\vec{r}')\delta\left(t-\frac{|\vec{r}-\vec{r}'|}{v_s}\right)d\vec{r}'\right] \tag{2.1.13}$$

Eq. 2.1.13 can be understood as follows: an absorber of volume V emits initial pressure, we are sampling the generated pressure field at point $\vec{r}$ and a given time t. Each point in $\vec{r}'$ in the absorber is an infinitesimal emitter of ultrasound who's amplitude is determined by the initial pressure function $p_0(\vec{r}')$. The delta function assures that the contribution to the pressure at point $\vec{r}$ would be a superposition

of points $\vec{r}'$ in the absorber that are located at the same distance from $\vec{r}$. For such points $|\vec{r}-\vec{r}'| = v_s t$ therefore **Eq. 2.1.13** can be simplified:

$$p(\vec{r},t) = \frac{1}{4\pi v_s^2}\frac{\partial}{\partial t}\left[\frac{1}{v_s t}\int_V p_0(\vec{r}')\delta\left(t-\frac{|\vec{r}-\vec{r}'|}{v_s}\right)d\vec{r}'\right] \quad (2.1.14)$$

Knowing $p_0(\vec{r}')$ we can use **Eq. 2.1.13** to get the acoustic pressure at any point in time and space.

Ultrasound propagation in tissue

Similarly, to electromagnetic waves ultrasound waves can reflect and refract from interfaces. In optoacoustic imaging we mostly concerned with longitudinal waves because water that is used as coupling medium between tissue and the sensor does not support other waves like shear waves. The analogy to the optical refractive index in acoustic is the acoustic impedance of the medium:

$$Z = \rho v_s \quad (2.1.15)$$

Where ρ is the density of the medium and v_s is the speed of sound. For normal incidence on an interface between Z_1 and Z_2 the ratio of the reflected and transmitted wave intensity relative to the incident intensity is given by the reflection and transmission coefficients, respectively:

$$R = \left(\frac{Z_2 - Z_1}{Z_2 + Z_1}\right)^2 \quad (2.1.16)$$

$$T = \left(\frac{2Z_2}{Z_2 + Z_1}\right)^2 \quad (2.1.17)$$

If the wave is incident at an angle θ_1 to the normal to the interface, then it is reflected at the same angle θ_1 and refracted at an angle θ_2, given by the acoustic analogy to Snell's law:

$$\frac{\sin\theta_1}{v_{s,1}} = \frac{\sin\theta_2}{v_{s,2}} \quad (2.1.18)$$

In analogy to electro-magnetic waves ultrasound is also attenuated in tissue [12]. The frequency dependent attenuation coefficient follows a power law:

$$\alpha(f) = \alpha_{0f}|f|^n \quad (2.1.19)$$

Where f is the ultrasound frequency, α_{0f} is the attenuation constant, and n is a positive number. For water $\alpha_{0f} = 0.00217$ dBMHz^{-2}cm^{-1} and $n = 2$, while for tissue $\alpha_{0f} = 0.5$ dBMHz^{-2}cm^{-1} and $n = 1$.

Time- and frequency-domain characteristic of a spherical source

Under the condition of uniform illumination and constant light fluence within the object **Eq. 2.1.14** can be solved for various source geometries. A representative example is a sphere as it can represent micro- or nano-particles, often used for characterization of optoacoustic microscopy and mesoscopy systems good, or is a coarse approximation of a blood cell, which is the most studied absorber in the optoacoustic imaging field.

Assuming a sphere of radius a, absorption coefficient μ_a, uniform illumination with fluence ϕ, and no reflections at the interface boundaries with the surroundings medium $Z_{sphere} \approx Z_{\text{medium}}$. The solution of **Eq. 2.1.14** under those conditions yields the time dependent pressure field at point $\vec{r}$ from the center of the sphere [13]:

$$p(\vec{r}, t) = \frac{a\mu_a \Gamma \phi}{2r}(1 - \hat{\tau})\Theta_{0,2}(\hat{\tau}) \tag{2.1.20}$$

Where $\hat{\tau}$ is the dimensionless retarded time:

$$\hat{\tau} = \frac{v_s}{a}\left(t - \frac{r - a}{v_s}\right) \tag{2.1.21}$$

And $\Theta_{0,2}(\hat{\tau})$ is a boxcar function such that $\Theta_{0,2}(\hat{\tau}) = 1$ for $\hat{\tau} \in [0,2]$ and 0 otherwise. **Eq. 2.1.20** shows that the amplitude of the emitted signals is directly proportional to the size of the object as larger objects absorb more energy (that is assuming the uniform illumination assumption is still valid), and is inversely proportional to the distance from the object as expected due to diffraction. Using **Eq. 2.1.20** and setting $v_s = 1500$ m/s (the speed of longitudinal waves in water) and $\mu_a \Gamma \phi / 2 = 1$ we simulated the ultrasonic signals emitted from spheres of different radii.

As predicted above spheres with larger radius emit stronger signals (**Fig. 2.1a**). By calculating the Fourier transform of the signals in **Fig. 2.1a** we can find the emission frequency spectrum of the spheres. From **Fig. 2.1b** we see that the dependence of the peak frequency with side is $f_c \sim 0.8 v_s / 2a$, while the emitted bandwidth (-3 dB around f_c) for all the spheres is $\sim 140\%$ of

fractional bandwidth. Those results do not take into account the frequency dependent attenuation of ultrasound in tissue but they already point to the immense requirements form the ultrasound sensors. For high resolution imaging the sensors have to be extremely sensitive to high frequencies which is difficult to achieve with current technology. Large sensing elements are more sensitive but usually are of lower frequency response because the pressure variations at the sensing element with acoustic wavelengths smaller than that element tend to average to zero and produce no detectable signal. This becomes even a greater challenge when imaging absorbers deep in the tissue as high frequencies tend to attenuate stronger when propagating to the detector. In addition, the sensors have to be very broadband in order to cover a wide range of absorber sizes found in the tissue (form blood capillaries not much larger than a single blood cell to large vessels of few hundreds microns in diameter).

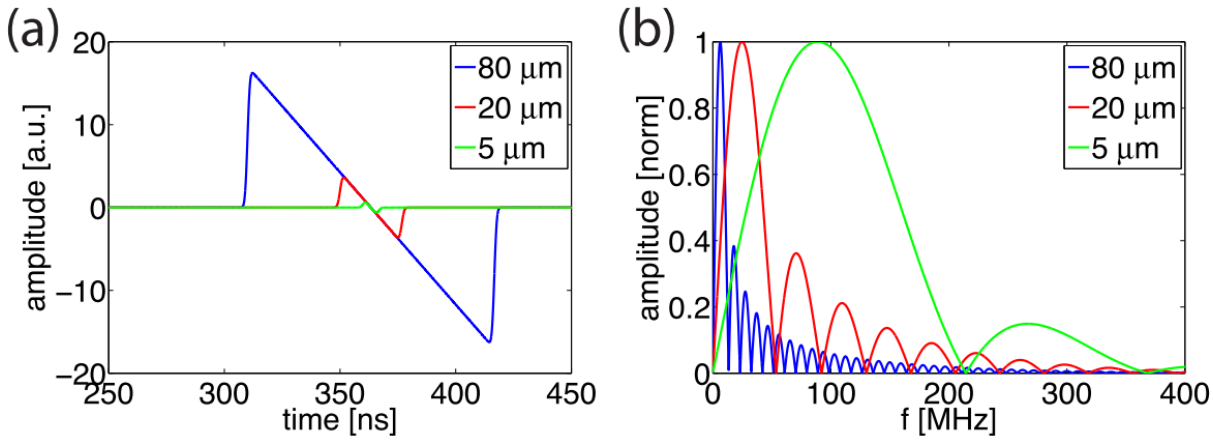

Figure 2.1 Pressure amplitude and spectrum emitted from spherical absorbers. **(a)** amplitude of the time domain ultrasonic signal emitted from spheres of various radii. **(b)** frequency content of the signals in **(a)** normalized to the amplitude of the peak frequency of the largest sphere.

2.2 Raster-scan optoacoustic mesoscopy (RSOM)

Full view (360º) optoacoustic tomography is not always possible because the access might not be available from all directions in clinical applications. Instead the object can be raster-scanned, such imaging approach is sometimes called as planar geometry tomography or is better known as raster-scan optoacoustic mesoscopy (RSOM) [3]. Although raster-scanning will generate worse resolutions than tomography [14] in many cases this approach is unavoidable. In RSOM a single

element is scanned above the sample while the sample is illuminated by short pulses of light which give rise to spatial distribution of acoustic pressure inside the tissue, simultaneously excited by the thermoplastic expansion of the absorbers.

In RSOM the sensor is scanned in a two dimensional plane (*x*- and *y*- axis), at each coordinate a time trace is acquired which corresponds to the depth of the image, also known as an A-scan. A line scan is performed when one of the coordinates is kept constant, also known as a B-scan. After sufficient number of B-scans were acquired that cover all the region of interest, a three-dimensional tomographic method is used to project the collected signal into a 3D grid and form a 3D image. It is important to perform sufficiently long B-Scans so the object is scanned through the whole acceptance angle of the sensor, failing to do so would deteriorate the image resolution and is known as the finite scanning range problem [15]. The scanning step has to be smaller than the acoustic lateral resolution achieved by the sensors and the sampling rate has to be sufficiently fast to sample the highest frequency detected by the sensor (see next sections) in order to avoid deterioration of the image resolution.

Image reconstruction

When the whole object is illuminated the absorbers emit ultrasound simultaneously, the detected pressure as a function of time in each A-scan contains contributions from all the absorbers in the object. In order to provide visualization of the absorber distribution within the tissue image reconstruction has to be performed. The most commonly used reconstruction algorithm is the time domain back-projection [16]. The measured signal by the detector are back-projected to the absorbing volume from the measurement surface that encloses the volume. This surface can be a sphere, infinite cylinder, infinite place, etc. In planar RSOM geometry if the scanning plane is not sufficiently large in respect to the detection angle of the sensor the achieved resolution will deteriorate compared to the theoretical resolution limit (see next section).

The measured pressure signals are back-projected to the imaging region of interest, the initial pressure $p_0(\vec{r}')$ at position $\vec{r}'$ can be found by inverting **Eq. 2.1.14** [16]:

$$p_0(\vec{r}') = \int_{\Omega_0} \frac{d\Omega}{\Omega_0} \left(2p(\vec{r}, t) - 2t \frac{\partial p(\vec{r}, t)}{\partial t} \right) |_{t=|\vec{r}'-\vec{r}|/v_s} \tag{2.1.22}$$

The initial pressure is expressed as a function of the pressure $p(\vec{r}, t)$ detected by the detector at position $\vec{r}$ over time *t*. **Eq. 2.1.22** can be understood as follows: for each detector position $\vec{r}$ on the scanning plane, the pixels of the image that are located at a distance $|\vec{r}' - \vec{r}|$ from the sensor (in a 3D volume) are assigned a value equal to the signal measured in time $t = |\vec{r}' - \vec{r}|/v_s$ minus the derivative. All those pixels are then weighted by $d\Omega/\Omega_0$ which is the solid angle subtended from point $\vec{r}'$ by the sensor at point $\vec{r}$. The final image is produced by summing over all the coordinated the senor was measuring at during the raster-scan. The first term in **Eq. 2.1.22** is called the delay and sum algorithm and it gives the same weight for all the frequencies, while the derivative term gives a higher weight to the higher frequencies.

Unfocused detection

When a sensing element is raster-scanned above the sample the lateral resolution of the reconstructed image in the *xy* plane would be strongly dependent on the aperture of the element. If the aperture is larger than the emitted ultrasonic wavelength the sensor would induce lateral blurring on the image. In the axial direction (depth) the resolution depends on the ability of the sensor to distinguish two succeeding signals in time. For a sensor with aperture diameter of ϕ_d and a cutoff frequency of f_{cutoff} the lateral and axial resolution are given by [17]:

$$R_L = [(R_A)^2 + (\phi_d)^2]^{1/2} \tag{2.1.23}$$

$$R_A \approx 0.8 v_s / f_{cutoff} \tag{2.1.24}$$

Consider for example the intravascular ultrasound probe (IVUS, commercially available from Boston Scientific). This piezoelectric transducer has rectangular aperture of 1 × 0.8 mm^2, but can be approximate as circular with $\phi_d \approx 1$ mm. With bandwidth of 15 MHz we would expect axial resolution of $R_A \approx 80$ µm (**Eq. 2.1.24**) when imaging in skin or water ($v_s = 1500$ m/s). The lateral resolution on the other hand (**Eq. 2.1.23**) would be equal to the aperture $R_L \approx \phi_d$. Despite the relatively high frequency response of the IVUS, RSOM imaging with it would result in srong lateral blurring. In order to take full advantage of the bandwidth the aperture must be smaller than the acoustic wavelength $\phi_d \ll \mathbf{0.8} v_s / f_{cut}$. In such case the sensor is said to be a point sensor and the image resolution is isometric $R_A \approx R_L$.

Focused detection

The sensitivity of commonly used piezoelectric detectors is proportional to the surface area of the active element, this means that for point detectors the sensitivity approaches zero. To overcome this limitation focused detectors were developed that employ either acoustic lenses or spherically shaped elements [3]. In this manner the sensitivity is increased due to the large area of the active element while the focal spots act as a virtual sensor that mimics the aperture of a point sensor, offering improved resolution [18]. The resolution of focused transducers is defined by the waist diameter of the of the acoustic field at the focal spot. The lateral and axial resolutions are given by [19]:

$$R_L = 0.71 \frac{v_s}{NA_s \cdot f_c} \tag{2.1.25}$$

$$R_A = 0.88 \frac{v_s}{\Delta f} \tag{2.1.26}$$

Where NA_s is the numerical aperture of the sensor, f_c is the central frequency, and Δf is the bandwidth of the sensor. State-of-the-art focused sensors offer high sensitivity and resolutions of $R_L \approx 30$ µm and $R_A \approx 15$ µm [3], but their large footprint makes applications like endoscopy, intravascular difficult.

2.3 Ultrasound sensors

The performance and properties of ultrasound sensors are of the strongest effect on image quality in optoacoustic mesoscopic. As was indicated in previous section the detection bandwidth and sensor size effect image resolution and the sensitivity effects the imaging depth and the SNR (or contrast) of the image. In this section we briefly survey several sensor platforms and discuss the pros and cons of each platform.

Piezoelectric sensors

In optoacoustic imaging and ultrasonography signals are traditionally acquired with piezoelectric sensors. This is the result of abundance of piezoelectric materials in nature, in addition to the well-established manufacturing processes and proven robustness of the technology. Ultrasound is detected when the piezoelectric crystal converts stress to voltage and vice versa. The resonance frequency (f_c) of such transducers is inversely proportional to the thickness of the sensing element [20]:

$$f_c = \frac{v_s}{2l} \tag{2.1.27}$$

Where v_s is the speed of sound and l is the thickness of the sensing element. A common piezoelectric crystal used in clinical transducers is the Lead (Plumbum) Zirconium Titanate (PZT), the acoustic impedance of this crystal is $Z_{PZT} \sim 30$ MRayls which is very far from the acoustic impedance of tissue, commonly $Z_{tissue} \sim 1.5$ MRayls. The high impedance contrast results in reflection of a large portion of the ultrasound wave in the interface (**Eq. 2.1.16**). In order to improve the detection and ultrasound emission efficiently of piezoelectric sensors matching and backing layers can be applied onto the sensing element. The acoustic impedance of the matching layer has to be carefully selected in order to optimize transmission of ultrasound, examples are layers that their impedance is the geometric mean between the impedance of the sensor and the surrounding [21]. Another example is a layer with a gradient acoustic impedance [21], which is the acoustic analogy of the optical GRIN lens. **Table 2.1** describes 3 commonly used examples of piezoelectric based sensors. An observation can be made that small unfocused piezoelectric elements are not very sensitive relative to their size, in addition they lose sensitivity when miniaturized.

Capacitive micro-machined sensors

Capacitive micro-machined ultrasound transducers are manufactured using the CMOS mass-production processes in the semi-conductor foundries. It's compose of a thin membrane suspended over a cavity in the silicon wafer. Both the membrane and the substrate are connected to electrodes, creating a capacitor. Ultrasound that perturbs the membrane change the capacitance of the CMUT and can be detected. Alternatively applying alternating voltage forces the membrane to vibrate and produce ultrasound [22]. The frequency response of the CMUTs is dominated by the mechanical

resonance of the bandwidth. Despite the small size the CMUTs exhibit high sensitivity but their low bandwidth is unattractive for optoacoustic imaging.

Transducer	Size (μm^2)	Bandwidth (MHz)	NEP ($mPa/Hz^{1/2}$)
Olympus panametrics V214-BB-RM (spherically focused)	30×10^6 ~37 (virtual sensor)	50	0.2
Precision acoustic needle hydrophone (unfocused)	1×10^6	12	14.4
Boston scientific IVUS (unfocused)	0.8×10^6	15	450
CMUT	0.4×10^4	5	1.8
MRR	$\pi(30)^2$	280	5.6
Fabry-Pérot etalon	$\pi(11)^2$ (interrogation spot)	22	78
π-FBG	10×270	30	25

Table 2.1 Properties of piezoelectric, micromachined, and optical sensors of ultrasound [23].

Optical sensors

There is a wealth of technologies allowing optical-based detection of sound [23]. In optoacoustic imaging optical detection has a fundamental advantage over piezoelectric detection because sensors can be miniaturized without sacrificing sensitivity [23]. **Table 2.1** describes 3 commonly used examples of optical resonator-based based sensors. Micro-fabricated resonator-based sensors are especially attractive, as their small sizes lead to unparalleled detection bandwidths without loss of sensitivity. Polymer micro-ring resonators (MRR) fabricated with imprint lithoraphy have been demonstrated with diameters as small as 60 µm and bandwidths reaching more than 280 MHz [24]. Their optical transparency and small size offer easy integration into existing microscopy systems [25], [26] and endoscopes [27]. On the contrary the piezoelectric IVUS, which is utilized in intravascular and endoscopic applications, is ~300 –fold larger than

the MRR and at the same time 80 –fold less sensitive. It is important to note that the detection bandwidth of the IVUS is 19 – fold smaller than that of the MRR. If the detection bandwidth of the MRR would have been narrowed (by analog or digital filtering for example) it's sensitivity would greatly increase. Another example is the Fabry-Pérot (FP) etalon sensors made of a 40 μm thick polymer film deposited on a glass slide [28]. The FP sensor is interrogated by a free beam and the sensor size is defined by the diameter of this beam in the polymer film. Unlike the MRR the resonator is not confined laterally, by using galvanometric mirrors it is possible to perform fast scanning of the interrogation beam and image the object without moving it or the sensor with mechanical stages. The bandwidth and the size of the interrogation spot are mostly defined by the thickness of the FP film, which is limited by the process uniformity. Nevertheless, this configuration offers improved resolution over unfocused piezoelectric sensors and good sensitivity despite the extreme miniaturization. FP etalon sensors are very attractive for imaging of large objects, where time rather than the resolution are of importance. For example, in vivo imaging of anesthetized mice or limbs of a human patient.

Optical resonator-based sensors were also implemented in optical fibers, again without loss of sensitivity. Two Bragg gratings with a gap between them were written in the fiber's core by exposure to UV and used as distributed reflectors. This resonator configuration also known as the π-phase-shifted fiber Bragg grating (π-FBG). π-FBG sensors are very attractive for endoscopic and intravascular applications and can be easily integrated into such systems alongside other fibers that are already used for light collection and delivery.

In optical resonator-based sensors ultrasound waves are detected when shifts in the resonance wavelength occur in response to phase changes due to variation in the cavity length and the photo-elastic effect. The extent of the resonance shift depends on photo-elastic constants and the Young modulus of the sensor. Polymer sensors with large photo-elastic constants and low Young's modulus are more sensitive compared to silica fiber sensors (**Table 2.1**). The resonance shift is further amplified by the Q-factor of the resonance, therefore resonators that can strongly confine light and achieve high Q-factors are desirable.

Interrogation of optical resonance-based sensor is described in **Fig. 2.2** (in this figure the light is pumped to the sensor through an optical fiber or a waveguide but free space variants also exist). CW laser pumps light into the sensor's cavity (**'Cavity'; Fig. 2.2**) abstracted as a Fabry-Pérot etalon with two parallel reflectors (**'Optical reflectors'; Fig. 2.2**). The laser is connected to the sensor trough an optical fiber (**'Fiber'; Fig. 2.2**) and an interface (**'Interface; Fig. 2.2**). For fiber sensors the interface can be just an FC/PC or an FC/APC fiber connector, for MRR it can be an adiabatic taper that interconnects between the fiber and the

polymer bus waveguide of the MRR. To improve the sensitivity, the laser is tuned off-resonance to the point of the maximum slope of the resonance curve (dashed curve in **'WL setting'; Fig. 2.2**) ensuring maximum amplification of the phase variations in response to incident ultrasound waves (**'US'; Fig. 2.2**). The optical reflected intensity modulations are routed by the fiber circulator (**'CR'; Fig. 2.2**) to the photodiode (**'PD'; Fig. 2.2**) and recorded by an oscilloscope photodiode (**'oscilloscope'; Fig. 2.2**).

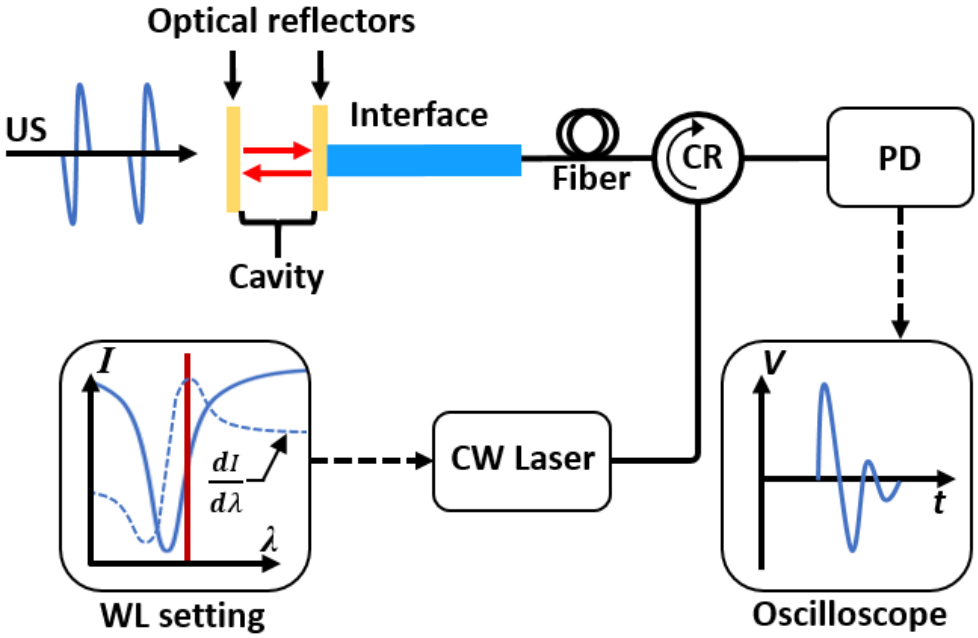

Figure 2.2 Schematic of a common optical sensor interrogation setup. CR, fiber circulator; CW, continuous wave; PD, photodiode; WL, wavelength; US, ultrasound. The dashed curve in 'WL setting' indicates the slope of the resonance as a function of wavelength, and the red horizontal line indicates the off-resonance tuning of the CW laser.

3. Silicon-on-insulator ultrasound sensors

This chapter provides introduction to the basic photonics components in the silicon photonics platform. We also discuss properties of Bragg gratings and π-phase shifted Bragg gratings in the fiber and silicon photonics platform. We experimentally characterize the sensors and derive theoretical models explaining the difference in performance of each platform focusing on sensitivity, sensor size, frequency response and bandwidth

3.1 Introduction to silicon photonics

Advances in the microelectronics industry enable tremendous levels of miniaturizations, as predicted by Moore‘s law [29]. Electronic integrated circuits (IC) which are the basis of modern technology are constantly reduced in size, cost, and power consumption. State of the art single element is already sized less than few dozens of nanometers. In the recent decades, a great amount of research was done toward harnessing the 60 years of technological development in the microelectronic industry and extending it for fabrication of micro-mechanical systems (MEMS) and photonics integrated circuits (PICs) [30], [31].

The translation of optical components to the framework of microfabrication has several major benefits: First, miniaturization of components leads to construction of dense arrays or realization of complex layouts with ultra-small footprints. For example, a silicon waveguide manufactured on a silicon-on-insulator (SOI) wafer can have a cross section as small as $220 \times 450\ nm^2$ [32], and complex structures as neural networks for machine learning applications were downsized to a single chip [33], [34] – eliminating the interconnect barriers [35] and allowing computation with the speed of light. Second, confinement of light in dimensions smaller than the wavelength allows for study and utilization of the enhanced interaction of light and molecules or nano-particles for construction of on-chip Bio-sensors [36] and lab-on-chip [37]. And finally, reproducibility and mass production using cheap and well-established processes.

Our work was realized using the SOI platform, better known as *Silicon Photonics*. A typical wafer consists of several layers: Si substrate of ~700μm, SiO_2 *buried oxide* (BOX) of ~1.5μm acting as the bottom cladding, Si layer of 220 nm which is the media the photonic structures are etched from or imprinted on, and a top cladding usually consisting of ~1.5mm of SiO2. Depending on the application other materials with varying thicknesses like I-line photoresist or air can also be used as the cladding (increased exposure is desired in application like bio-sensors and minimizing exposure is essential for low-loss applications in optical telecommunications).

Silicon photonics is one of the most active research fields today. It is extremely attractive due to compensability with existing mass-production processes in the microelectronic foundries making this platform cheap and highly scalable. Another advantage is that silicon is transparent in the optical C-band (around the 1500 nm wavelength) therefore a large variety of cheap photodetectors and laser sources is available as this band as it is widely utilized in telecommunication and fiber technology.

Current research in Silicon photonics focuses in development of novel optical components unique to this platform and integration of large-scale PICs, alongside development of new and improvement of existing manufacturing processes [38]. Today access to the SOI platform is available also to small companies and R&D labs in the form of a multi-wafer projects (MWPs). In an MWP the production costs are shared between the costumers by sharing the space in the lithography mask. After the wafer is manufactured each die (a copy of the mask containing all the projects) is diced in order to separate each project and the corresponding chips are shipped to the costumers without them knowing what kind of projects they were in neighborhood to. This work is a result of MWP offered by the ePIXfab consortium [39] which is available in the European Union for more than a decade.

3.2 Motivation

The lateral resolution of state of the art optoacoustic imaging systems employing focused piezoelectric-based sensors is limited to ~ 30 μm [3] while the lateral resolution of purely acoustic modalities like ultrasonography and elastography, employing piezoelectric-based sensor arrays, is limited to ~ 400 μm [40]. In order to improve those figures the employed ultrasound sensor has to

be highly sensitive (NEP < 100 Pa), have high detection bandwidth (> 50 MHz), and have ultra-small size or aperture (< 30 μm) [23]. This is particularly challenging in optoacoustic imaging where the amplitude of the emitted ultrasonic signal scales directly with the size of the imaged absorber and the frequency content of the emitted ultrasonic signal scales inversely. Hence a suitable sensor has to have large bandwidth and a good signal to noise ratio (SNR) over all of the bandwidth, which is often not possible with piezoelectric-based sensors. In addition, in order to avoid smearing of the image by the sensor due to finite-size sensor aperture, the aperture has to be smaller than the imaged object. This is impossible to achieve as the sensitivity of piezoelectric-based sensors scales directly with the size of the sensing element. For example, sub-mm piezoelectric elements used for intervascular ultrasound imaging (IVUS) suffer from reduced bandwidth of ~ 20 MHz and a sharp drop in sensitivity. The NEP of the IVUS is 3 orders of magnitude higher than large piezoelectric-based sensors or optical resonator-based ultrasound sensors [41], resulting in lateral resolution deterioration to ~ 200 μm [42].

For sensors sized under 1 mm^2 optical resonator-based sensors have already surpassed piezoelectric-based sensors in terms of sensitivity and bandwidth. Polymer micro-ring resonators (MRR) with diameters of ~ 60 μm were demonstrated with NEP of 6 Pa and detection bandwidth reaching 300 MHz [24]. Further miniaturization and improvement in imaging performance is not possible due to high optical bending losses in the polymer platform. In the case of MRRs the large bandwidth cannot be fully exploited and the image will be smeared by the size of the sensor resulting in lateral resolution larger than 60 μm. In order to image objects as small as human blood cells without smearing, the sensor has to be further miniaturized reaching aperture smaller than ~ 7 μm. As a consequence, we need to explore a different platform for construction of optical resonator-based sensor. When choosing a platform several important aspects of the platform have to be considered:

1. **Miniaturization** – The smaller is the optical resonator and the stronger is the light confinement the smaller is the sensor aperture and the larger is the detection bandwidth, both resulting in improved imaging resolution.
2. **Optical phase sensitivity** – The lower are the optical losses in the resonator the stronger is the light confinement and the Q-factor. The latter defines the optical phase sensitivity of the sensor [43] and is directly proportional to detection sensitivity of ultrasound waves (see **Section 3.4.4**).

3. **Acoustic phase sensitivity –** Elasto-mechanical and elasto-optical properties of the platform determine the amount of the optical phase gained when ultrasound waves incident on the sensor. Specifically, the Young modulus and the elasto-optic coefficients determine the amount of structural deformation of the optical resonator [43] and the acoustic impedance of the material determines the fraction of the ultrasonic waves reflected from the sensor due to impedance mismatch with the surrounding medium. Both of those parameters contribute to the sensitivity of the sensor to detection of ultrasound waves (see **Section 3.4.4**).
4. **Sensor arrays and multiplexing –** For in vivo imaging of biological processes fast imaging system are required. Raster-scanning of a single sensor is limited by mechanical movement of the translation stages and can be slow. The ability of the platform to support multiplexing of large arrays ensures fast imaging times and higher sensitivity of the imaging system.

The SOI platform offers particularly high optical refractive index contrast $\Delta n \approx 2.5$ [44], while other commonly used platforms for sensing like silica fibres and polymer PICs, offer only $\Delta n \approx 0.001$ and $\Delta n < 0.5$ respectively [24]. This means that silicon photonics optical component can be greatly miniaturized compared to implementation of the same components in silica fibres or polymer. Single-mode silicon waveguides optimized for the 1550 nm wavelength were demonstrated with sub- wavelength light confinement along the cross-section of the waveguide. Indeed, the standard cross-section of such a waveguide measures 200×500 nm^2 which is respectively 7.5 and 3 – fold smaller than the optical wavelength. On the contrary, the core of a single-mode optical fibre measure ~ 9 μm in diameter which is 6 – fold larger than the wavelength, and the cross-section of a typical polymer waveguide measured 1×1 μm^2 which is only 1.5 – fold smaller than the wavelength. When considering the **miniaturisation** aspect, the SOI would be the platform of choice

The sub-wavelength light confinement in the polymer and SOI platform induces additional optical losses. While propagation losses in a single mode silica fibre at 1500 nm wavelength can be as small as 0.2 dB/Km the propagation losses polymer and silicon waveguides can be as large as 1-2 dB/cm. In imprinted polymer waveguides the main mechanism of propagation loss is absorption [45] while for the silicon waveguide it is the process dependent side-wall roughness, inducing

scattering of the propagating mode [46]. The high losses in those platforms are mitigated by large index contrast relative to the silica fibre platform, enabling stronger light confinement along the optical axis by stronger Bragg gratings with larger coupling coefficient (see **Section 3.4**). The resulting Q-factor of a π-shifted Bragg grating implemented in SOI was measured to be 1.5×10^4, and for imprinted polymer MRR sensor submerged in water Q-factor of 2×10^4 was measured [47]. Those values are only an order of magnitude smaller than the Q-factor of 1.8×10^5, measured for a π-shifted Bragg grating implemented in a silica fiber [48], despite having propagation losses that are larger by 5-6 orders of magnitude compared to the silica fiber. Another type of losses to consider are optical bending losses. While the high-index contrast of the SOI allows to realize compact and dense PICs due to the ability to achieve 90° band of the waveguide over a radius as small as 1-2 μm with losses as small as 0.013 dB/90° band [49], the polymer platform suffers from high banding losses due to weak confinement of the optical mode and high leakage at the band [50]. The latter means that in order to maintain high Q-factors and high sensitivity imprinted MRR sensors are practically limited to diameters not smaller than ~60 μm. These high bending losses have wider implications generally resulting in large device footprint and limited integration density of polymer platform, making it less attractive for construction of dense PICs.

In conclusion, the expected optical phase sensitivity of the SOI and polymer platform are similar and somewhat weaker than of the silica fiber platform, but the extent of **miniaturization** offered by the SOI cannot be achieved by other platform, hence making SOI the platform of choice when considering **optical phase sensitivity**.

When considering the elastic material properties of the platforms the polymer platforms has a decisive advantage as the Young modulus is 2-3 orders of magnitude smaller and the photo-elastic constants are 1-2 orders or magnitude larger than for silica and silicon [51]. This means that when ultrasound waves are incident on a polymer sensor its structural deformation and the change of the effective refractive index through elaso-optic effect are much stronger, hence the optical phase gained by a polymer resonator-based sensor will be much higher than the phase gained by a silicon resnonator-based sensor with exactly the same optical phase sensitivity. In addition, the acoustic impedance of polymers is close to acoustic impedance of tissue and water (commonly used as coupling medium in optoacoustic imaging) while the acoustic impedance of silicon is 15 – fold larger, resulting in ~80% of the ultrasonic waves incident on the silicon sensor being reflected and

not propagating into the sensor.

π-shifted Bragg grating sensor realized in a single mode silica fiber was demonstrated with NEP = 400 Pa [48], which is 2 orders of magnitude worse than the NEP of a polymer MRR despite the Q-factor of the silica resonator was an order of magnitude larger than of the polymer MRR. Because of the above reasons previous realizations of ultrasound sensors in the SOI platform ended in failure to detect longitudinal ultrasonic waves [52] or required etching of membrane under the sensor to enhance sensitivity, resulting in bandwidth < 1 MHz which renders those sensors unusable for imaging applications [53]. It is clear that in regard to **acoustic phase sensitivity** the polymer is the platform of choice, in **Section 4** of this work we show that it is possible to circumvent those disadvantages of the SOI platform by a novel resonator design that directly exposes the optical mode to ultrasound without inducing additional optical losses. The achieved sensitivity is on the same order of magnitude as the sensitivity of polymer MRR sensors, while the efficiency of the transduction mechanism (sensitivity normalized by the sensing aperture) is 3 orders of magnitude larger than that of the polymer MRR sensors.

Piezoelectric sensors array of several hundreds of elements were demonstrated with density of 9.5 detectors/mm^2 but technical challenges prevent manufacturing of sensitive arrays with bandwidths above 30 MHz [3], which limits the imaging resolution to values larger than ~50 μm. In addition, piezoelectric sensors are consisting of several parts that are manufactured separately (e.g. amplifiers, acoustic lenses) and their integration is difficult and if not executed flawlessly will reduce performance.

Optical polymer resonator-based arrays were not demonstrated at all due to unattractive device size. The polymer platform lacks active functionality like light emission, amplification, modulation etc. Hence polymer MRR sensors will always have to rely on optical coupling to external light sources and detectors, which greatly increases cost and complexity when. On the other hand, due to the strong light confinement the SOI platform can support PICs with inter-device distance as small as ~1-2 μm. Even with conservative spacing of ~ 10 μm an SOI array of π-shifted Bragg grating sensors can achieve densities an order of magnitude larger than piezoelectric sensors and four orders of magnitude larger than polymer MRRs. The availability of on-chip photo detector [54] and light sources [7], [55] that can be manufactured simultaneously alongside the sensors means that multiplexing in the SOI platform is easy and was already demonstrated for optical links [56]. Hence when considering **arrays and multiplexing** the SOI is again the platform of choice.

In conclusion, our motivation in using SOI platform for sensor development can be summarized in the following advantages over piezoelectric-based sensors and other platforms commonly used for optical-based sensing (i.e. polymer PICs and silica fibres):

1. Miniaturization to sub-micron dimensions without loss in performance leading to improved imaging resolution.
2. Resonators with high Q-factors are attainable contributing to improved sensitivity of the sensor.
3. Small device footprint with high integration density alongside availability of on-chip light sources and photodetectors leading to construction of dense arrays.

This thesis aims to use those advantages in order to develop a novel optical SOI-based sensor of ultrasound for imaging applications, which surpasses in its performance state of the art piezoelectric and optical sensors. The unique optical resonator design circumvents the disadvantageous elastic properties of silicon showing a transduction mechanism that is 3 orders of magnitude more efficient than polymer MRR.

3.3 Silicon Photonics components

In this section we survey several of the most common photonic elements or building blocks used in construction of large scale layouts in silicon photonics. Each building block is a product of a collective research effort of many years followed by an optimization for the characteristic layer structure of the standardized SOI wafer. Standardization allows each participant of the MWP to use the same collection of building blocks (the so called ‘design kit’) enabling constructions of reproducible on-chip PICs with predictable performance.

The building blocks can be divided into passive elements: waveguides, tapers, fiber coupler [57], array waveguide gratings (AWG) [58], Bragg gratings [59], switches and multi-mode interferometers (MMI) [60], and active elements: photodiodes [54], lasers [7], and modulators [6].

In this work we used only passive elements from the design kit of IMEC fabrication facility (Leuven, Belgium), survey of the properties of active elements can be found elsewhere [32]. The elements used were: waveguides – carries light and interconnects other elements; tapers – for connecting two waveguides with a different cross-section adiabatically (without inducing losses

and exciting higher order or leaky optical modes); Bragg-gratings – for frequency filtering or sensing applications; fiber couplers – the interface between the on-chip waveguides and optical fibres used to carry light into and out of the chip.

3.3.1 Waveguides

Multimode waveguides are not desirable as a building blocks in particular for PICs used for optical communication or signal processing applications. The performance of the PICs can be compromised by the presence of multiple modes, inducing undesirable effects such as intermodal dispersion or optical signal distortion. The cross-sections of the most wide-spread single mode waveguides are presented in **Fig. 3.1**.

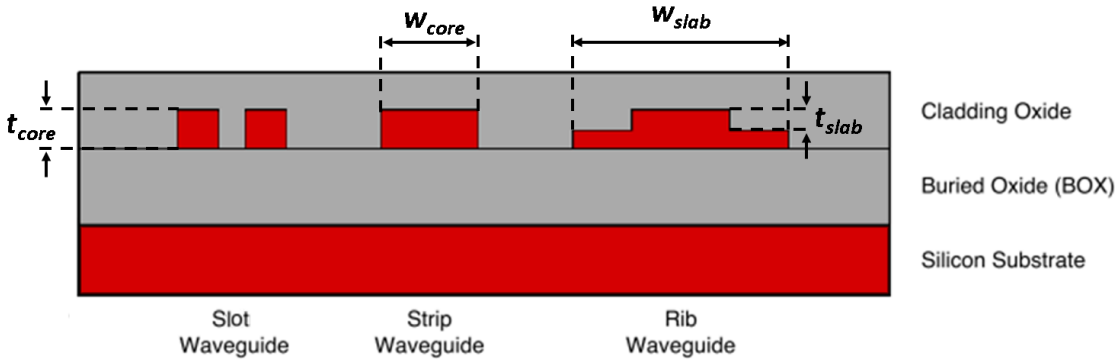

Figure 3.1 Cross-section of the most commonly used waveguide types in silicon photonics with typical SiO2 cladding. Left – Slot waveguides. Middle – Strip waveguides also known as photonic wires. Right – Rib waveguides also known as photonic wires.

Strip waveguides or photonic wires (**Fig. 3.1** – centre) are the simplest kind of a waveguide requiring only one etching step to manufacture. They have been shown to confine modes with cross-section as small as 200 x 200 nm and maintained single mode with w_{core} = 500 nm for air cladding and w_{core} = 450 nm for SiO2 cladding [32].

Fig. 3.1a and **Fig. 3.1b** respectively depict the Transverse Electric (TE) and the Transverse Magnetic (TM) electric field profiles of the optical mode of a w_{core} = 500 nm and t_{core} = 220 nm waveguides with an SiO2 cladding. The field profiles were calculated using a vectorial mode solver [61], [62]. From **Fig. 3.1** we can easily see that stronger field confinement in the waveguide core occurs for the TE mode. The exposure of the field to the waveguide wall roughness [63] and the

cladding directly effects the propagation and bending losses [49]. Propagating TE mode has considerable evanescent field around the sidewalls therefore their propagation losses are dominated by the sidewall roughness. At excitation wavelength of 1.55μm strip waveguides with TE mode have been reported with propagation losses of 1.5 dB/cm [64]. The bending losses of TE mode are negligible compared to those of the TM mode, allowing bending radius as small as 2.5 mm [32]. This makes the TE mode the preferable choice for reducing layout footprint and increasing element density.

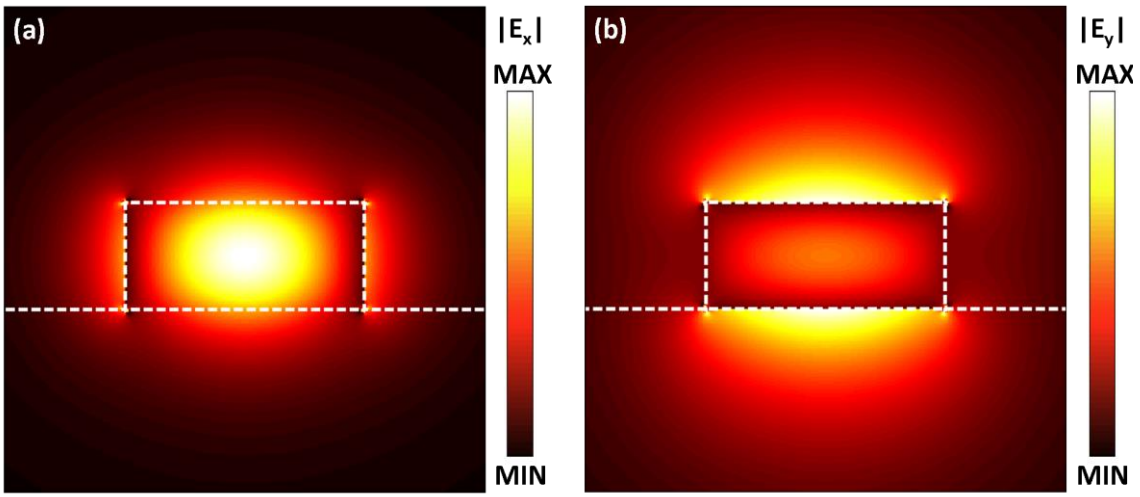

Figure 3.2 Normalized electric field profile over an area of 1 x 1 μm for a Si stripe waveguide with a cross-section of 220 x 500nm and an SiO_2 cladding. Dashed white lines indicate the boundaries of the waveguide **(a)** The TE and **(b)** the TM fundamental modes at wavelength of 1.55μm.

The higher confinement of the TE mode is expressed by a higher mode effective refractive index (n_{eff}). For the TE polarization (**Fig. 3.2a**) n_{eff} was calculated to be 2.452 and for the TM polarization (**Fig. 3.2b**) it is 1.782. We can estimate the propagation constant (β) of each mode according to the following equation:

$$\beta = k_0 n_{eff} \tag{3.3.1}$$

We can see that for the TE and TM modes $\beta_{TE} \neq \beta_{TM}$ meaning that the waveguide is strongly polarization dependent. The high birefringence can cause polarization beating of the modes, hence external excitation of only one mode is preferable for many applications. For our applications of sensing longitudinal ultrasonic waves with optical resonators it is also preferable to excite the TE mode as the energy density in the bulk of the cavity is higher for this

mode, hence more photonics will be effected by the perturbation of the cavity resulting in higher detector sensitivity. TM mode has been demonstrated to have higher sensitivity for detection of surface acoustic waves [65].

For applications that require lower propagation losses than what the strip waveguide can offer one can consider the rib waveguide geometry (**Fig. 3.1** - right). Such waveguides are manufactured by a two-step etching process: deep etch (220 nm – IMEC standard) to define the slab and a shallow etch (70 nm – IMEC standard) to define the ridge (rib). Single mode operation is ensured for w_{ridge} < 750 nm [66]. **Fig. 3.3** depicts the electric field profiles of the TE optical mode of a rib waveguide with $Si0_2$ cladding and the following parameters: w_{ridge} = 500 nm, t_{ridg} = 220 nm, w_{slab} = 1200 nm, t_{slab} = 220 nm. The overlap between the electric field and the sidewalls is very low resulting in reduced losses. Propagation losses for the rib waveguide have been reported to be as low as 0.3 dB/cm [66].

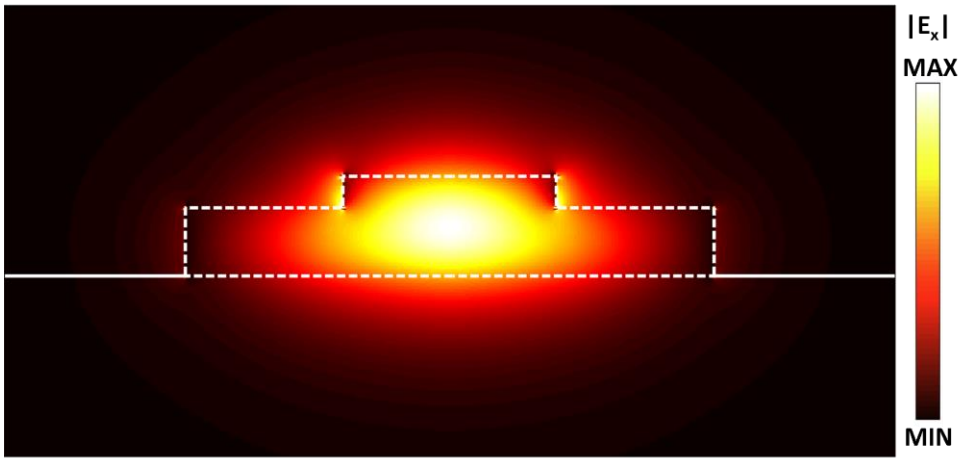

Figure 3.3 Normalized electric field profile over an area of 1 x 2 μm for a Si rib waveguide with SiO_2 cladding. The waveguide has strip dimensions of 70 x 500 nm and slab dimensions of 150 x 1200 nm Dashed white lines indicate the boundaries of the waveguide.

For applications that require the optical mode to have high exposure to the surrounding media it is worth to consider slot waveguides (**Fig. 3.1** – left). Such waveguides implemented for bio-sensing have shown improved sensitivity due to the enhanced light-matter interaction [67]. In this scheme, the optical mode is confined to the slot between the two cores and is exposure to an aquatic environment. Presence of molecules would result in local changes to the refractive index of the slot resulting in changes in the n_{eff} and detection.

3.3.2 Adiabatic tapers

Waveguides in different devices across the PIC are likely to be designed with different cross-sections in order to optimize performance. Tapers are sections of waveguide with a varying width that are used to efficiently couple between two different optical waveguides. It is achieved adiabatic transformation of the mode meaning: by gradually changing the size and the shape of first-order mode propagating through the taper to match the size and the shape of the first-order mode in the target waveguide, while undergoing relatively little mode conversion to higher-order modes or radiation modes (leaky modes). This adiabatic operation can be realized by increasing/decreasing the size of the taper cross-section very slowly.

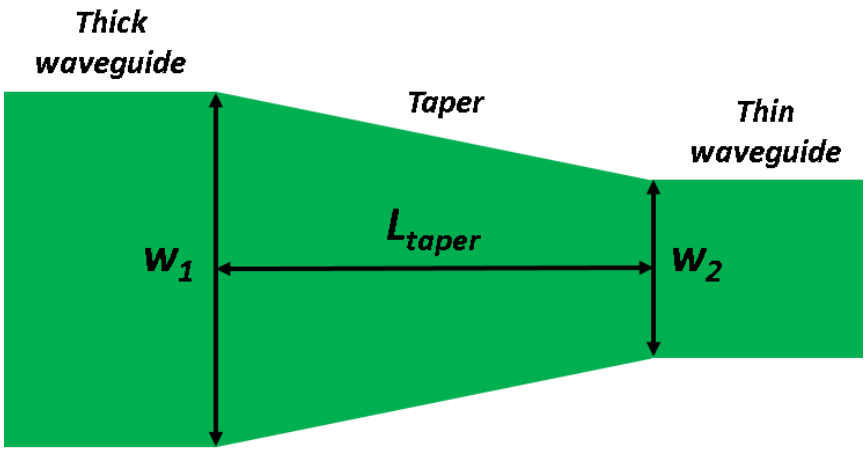

Figure 3.4. General schematic of a waveguide taper with length L_{taper} connecting two waveguides with widths w_1 and w_2.

Fig. 3.4 depicts a schematic of a taper with length L_{taper} connecting two waveguides with widths w_1 and w_2. The larger the ratio w_1/w_2 is the longer L_{taper} has to be in order to achieve high coupling efficiencies, which may induce additional propagation losses. This tradeoff between the coupling efficiency and propagation losses must be considered when designing PICs. For two silicon waveguides with t_{core} = 220 nm a taper of L_{taper} = 120 μm is required in order to connect two waveguides with w_1 = 12 μm and w_2 = 500 nm with transmission efficiency of 98% [68]. For the same waveguide thickness L_{taper} = 1.5 μm is sufficient to achieve efficiency of 96% for w_1 = 2 μm and w_2 = 500 nm [68].

More sophisticated tapers are required to connect between strip and rib waveguides. One design takes advantage of the lower propagation losses of a straight rib waveguide and combines it with a circular strip section that has lower bending losses in order to realize low loss 90 ° turn [66]. The connection between the strip and rib waveguides is achieved by adiabatically changing the slab section of the rib waveguide over L_{taper} = 15 μm. Tapers are also used as spot-size convertors when connecting the silicon photonics waveguides with external fibres [69].

3.3.3 Fiber couplers

Fibre couplers (grating couplers) address the need to couple light from an external source to the PIC. The most common scenario is coupling between a single mode optical fibre or a fibre array and a planar silicon strip waveguide. The couplers principle of operation is based on optical diffraction gratings: when light is incident on a grating it is diffracted due to the groves. When the geometrical path difference between the light diffracted by successive grooves is equal to the wavelength (λ) the diffracted light will be in phase. By varying the grating parameter and the incident angle it is possible to engineer the grating spectral response and the diffraction angle [57].

The most common type of a fibre coupler is a 1D weak waveguide grating (**Fig. 3.5**) where a shallow etch of the silicon (**Fig. 3.5**; *ed* ~ 70 nm) is used in order to create a planar diffraction grating with a period of Λ. Assuming a grating with a fill factor of 0.5 the effective refractive index of the grating section can be approximated as $n_{eff} \cong (n_{eff,e} + n_{eff,u})/2$, where $n_{eff,e}$ and $n_{eff,u}$ are the effective indexes of the etched and un-etched grating sections. The typical size of such grating is ~ 20 × 20 μm^2 with several tens of periods. The diffracted light has to be coupled into a single waveguide (**Fig. 3.5**; 'WG') with a width as small as 450nm, which requires the use of adiabatic tapers (**Fig. 3.5**; 'WG') at least 100 μm long [70]. For such a grating we can write the following Bragg condition (or the phase matching condition):

$$k_{in} \sin\theta + m2\pi/\Lambda = \beta \tag{3.3.2}$$

Where $k_{in} = 2\pi n_{clad}/\lambda_0$ is the wavenumber ion the cladding of the incident light, λ_0 is the wavelength in vacuum, θ is the angle of incidence, *m* is the diffraction order, and β (defined in **Eq.**

3.3.1) is the propagation of the light leaving the grating and entering the taper section. From **Eq. 3.3.2** we can calculate the resonance wavelength of the first diffraction order:

$$\lambda_0 = \Lambda(n_{eff} - n_{clad} \sin\theta) \tag{3.3.3}$$

Assuming SiO2 cladding, TE mode, and grating width of 18 μm we calculate $n_{eff,e} = 2.548$ and $n_{eff,e} = 2.856$. With grating $\Lambda = 630$ nm and near normal incidence $\theta = 10°$ we get $\lambda_0 \cong$ 1542 nm. **Fig. 3.6** depicts the measured spectral response of a grating with identical parameters, the measured resonance wavelength is ~1538 nm. The 4nm deviation from the designed resonance wavelength can be explained by manufacturing non-uniformities resulting in variation in the fill factor, the period of the grating, the thickness of silicon [71], and by inaccuracies in aligning the angle of incidence [72]. In fact, the gratings are very sensitive to the angle of incidence. Changing the angle only by half a degree to $\theta = 10.5°$ results in 8 nm shift of the resonance wavelength .

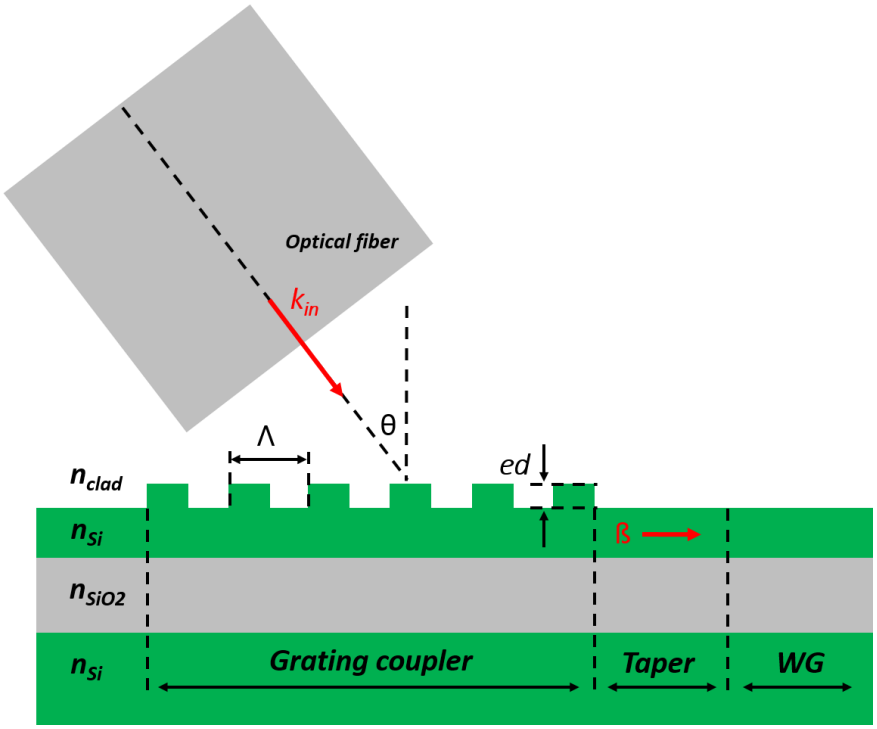

Figure 3.5 Schematic of an 1D SOI grating coupler. n_{clad}, refractive index of the cladding; n_{Si}, refractive index of the silicon grating; n_{SiO2}, refractive index of the silica substrate; *ed*, depth of the shallow etch; WG, waveguide; Λ, grating period; θ, angle of incidence; k_{in}, wavenumber of the incident light in the cladding; β, propogation constant of the diffracted light.

Grating couplers are strongly polarization dependent through n_{eff}, by using polarization maintaining fibres (PM) it is possible to excite different modes in the waveguide by appropriate

design of the coupler and rotation of the PM fibre [65]. Polarization independent gratings were also demonstrated by using subwavelength structures to create 2D grating [73]. Their application is not widespread because the birefringence of the silicon waveguide (see **Section 3.3.1**) is not desirable for most applications and it is usually avoided by coupling only a single polarization. The need for long taper sections can also be avoided by curving the grating lines thus focusing the diffracted light directly into the waveguide, resulting in more compact design [70]. Grating couplers were also utilized for bio-sensing [74], [75].

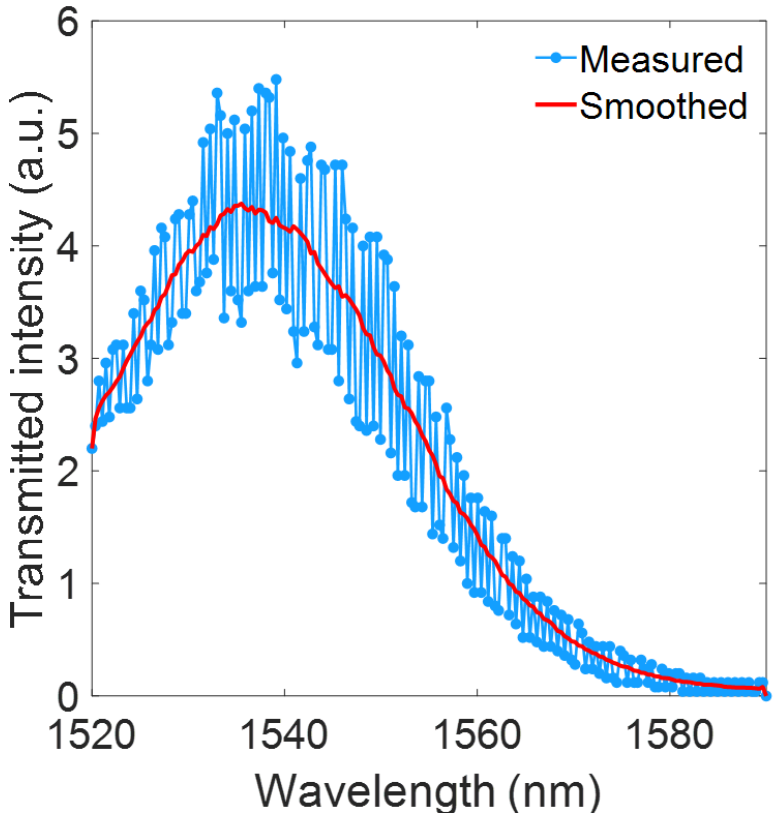

Figure 3.6 Spectral responses of an SOI fiber coupler grating with top oxide cladding and silicon thickness of 220 nm, fill factor of 0.5, $ed \sim 70$ nm, $\Lambda = 630$ nm, $\theta = 10°$.

3.3.4 Bragg gratings

In PICs Bragg gratings are constructed from the waveguides by periodically corrugating one of the waveguides dimensions. Due to the change in one of the spatial dimensions the corrugated section

has a different n_{eff}. Technically the simplest implementation is to increase the width of a strip waveguide periodical - side-wall corrugation (**Fig. 3.7**). For a strip waveguide with w_{core} = 500 nm and t_{core} = 220 nm, with SiO2 cladding, TE mode excitation, and rectangular corrugation, we get $n_{eff,1}$ = 2.452 for the uncorrugated section and $n_{eff,2}$ = 2.55363 for a section with corrugation of Δw = 40 nm. The change in the effective refractive index in this case Δn = 0.1 is larger by a factor of 100 than the achievable index of $\Delta n = 0.001$ for state-of-the-art germanosillicate fibers. The increased index contrast means that stronger Bragg reflectors can be achieved in the SOI platform over shorter lengths compared to the fiber optic platform (typically for SOI $L_{Bragg} = 100$ – 200 μm and $L_{Bragg} \sim 2$ mm for fibers).

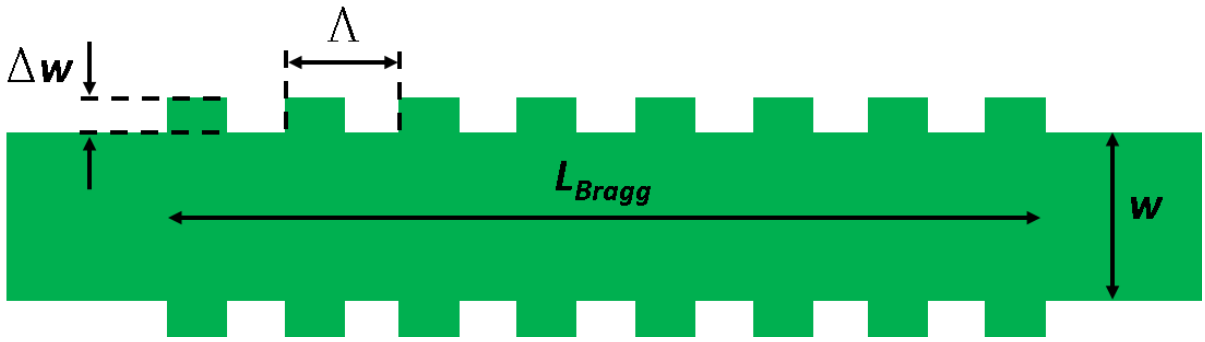

Figure 3.7. General schematic of a waveguide with width w containing a Bragg grating with length L_{Bragg}. The grating is created by adding side-wall corrugation to the waveguide with corrugation depth Δw and period of Λ.

If the corrugation is not too strong and there is no much change in the spatial distribution of the mode when propagating from section to section, the CMT still holds and the equations in **Section 3.4.1** can be used to describe the properties of the SOI Brag gratings. Yet the high refractive index of the SOI platform makes all the building blocks and especially the Bragg gratings (where the corrugation is in the order of few tens of nm) highly sensitive to dimensional variations and require high-resolution fabrication processes. This means that the equations in **Section 3.4.1** cannot be used to precisely pre-determine the properties of the Bragg gratings prior to manufacturing, but they can be used for rough estimation. Often many manufacturing iterations and optimizations processes are required to achieve the desired properties of an SOI Bragg grating.

One of the strongest effects is the non-uniformity in the silicon wafer thickness and the wafer polishing process [76], which can lead to variations of up to ±10 nm in the device thickness and

as a consequence a strong shift in λ_B. For the waveguide discussed above with n_{eff} = 2.452 for t_{core} = 220 nm and grating period of $\Lambda =$ 320 nm we expect a device with λ_B =1569 nm (**Eq. 3.4.1)**. When considering the potential thickness variations, we get $n_{eff} = 2.48803$ for $t_{core} =$ 230 nm and $n_{eff} = 2.41408$ for $t_{core} = 210$ nm. Meaning that practically λ_B can be anywhere between 1592 nm and 1545 nm. In addition, the etching process used in manufacturing of SOI devices typically results in angled sidewalls of the waveguides. The cross-section of the manufactured waveguide is slightly trapezoid instead of perfect rectangular. Hence in practice n_{eff} is smaller resulting in a blue shift in λ_B. Blue shifts as large as 11 nm have been reported [77] potentially locating λ_B for the Bragg grating discussed above can anywhere between 1581 nm and 1534 nm.

Another important dimensional variation is a result of the commonly used deep-ultraviolet lithography process (which is more attractive than electron beam lithography for commercial mass-production). The corrugation depths used for creating the Bragg gratings are usually smaller than the resolution limit of the lithography process, resulting in rounding of the rectangular corrugation and forcing it to be more similar to a sinusoidal shape [78]. Practically, this effect lowers the coupling coefficient of the manufactured Bragg grating. For the grating discussed above with rectangular corrugation of Δw = 40 nm the design coupling coefficient is κ =1295 cm^{-1} (**Eq. 3.4.5)**, while the measured coefficient is only κ =288 cm^{-1} [79].

The lowered κ strongly effect the bandwidth of the Bragg grating (**Eq. 3.4.10**). In order to estimate this effect we first need to calculate the group index at the Bragg wavelength using **Eq. 3.4.4**. $dn_{eff}/d\lambda =$ -0.001025 was calculated for the waveguide discussed above by linearly fitting the simulated n_{eff} as a function of the wavelength (**Fig. 3.8**). The effective refractive index for the waveguide in hands at $\lambda = 1550$ nm is $n_{eff} = 2.452$. Inserting those values into **Eq. 3.4.4** yields a theoretical group index of $n_g = 4.04$. The theoretical bandwidth of the grating can be calculated from **Eq. 3.4.10**, assuming a grating length of $L_{Bragg} = 125$ μm and accounting only for the effect of the lowered κ (ignoring the unpredictable shift in λ_B) we calculate $\Delta\lambda = 26$ nm for $\kappa = 1295$ cm^{-1} and $\Delta\lambda = 7$ nm for $\kappa = 288$ cm^{-1}. We note that because for the manufactured grating $\kappa L_{Bragg} = 3.6$ we are in the strong grating regime, hence as discussed in **Section 3.4.1** lowering κ (either as part of the design or as a side effect of the manufacturing) will result in narrowing of the bandwidth.

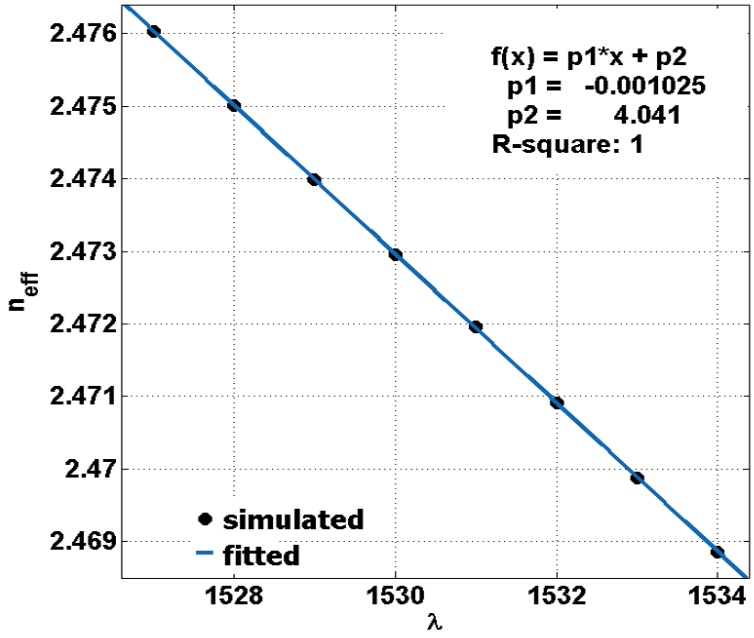

Figure 3.8 Dependence of the effective refractive index on the wavelength. The calculation was made for a strip silicon waveguide with oxide cladding and TE mode. t_{core} = 220 nm; w_{core} = 500 nm.

Bragg gratings were also implemented in the rib waveguide geometry [77] by corrugating either the slab or strip side-walls, and in slot waveguide geometry [67] by corrugating the outer side-walls. Alternative approaches to side-wall corrugation for creating Bragg gratings include etching holes on the top of the waveguide [80] and placing cylindrical pillars along the sides of the waveguides [81]. Those approaches are not wide-spread as they are technically more challenging and often are not compatible with the commercially wide-spread CMOS fabrication process.

3.4 Bragg gratings for ultrasound sensing

In this section we start by surveying the basic physics of Bragg gratings and continue to a more complex phase shifted Bragg grating resonators. We discuss in detail how grating parameters affect the optical field distribution and the spectral response of the gratings. We continue by discussing the application of phase shifted Bragg gratings to ultrasound sensing, we analyse in depth the performance of the sensor considering:

1. Sensitivity

2. Sensor size
3. Frequency response and bandwidth

We show how these performances are effected when the sensor is realized in different platforms due to the different range of grating parameters supported by each platform. We compare theoretical analysis to experimental characterization of a commercially available π-phase shifted fibre Bragg grating (π-FBG) realized in a single mode PM maintaining fibre (PWS-CUS-1549.07-7000MHz-PM1550-0-1.5, Teraxion) and a π-phase shifted waveguide Bragg grating (π-WBG) realized using a silicon strip waveguide on an SOI wafer with I-line resist as top cladding. For design and manufacturing of the π-WBG sensor see **Sections 6.1 and 6.2**. For principles of signal read-out from optical sensors see **Section 2.3**. For the characterization setup details see **Section 6.3** and **Section 6.4.**

3.4.1 Properties of Bragg gratings

Bragg gratings are a form of waveguide-embedded resonators with multitude of applications in photonics, ranging from sensors [82] to spectral filters [83]. The Bragg grating is realized by periodically modulating the effective refractive index (n_{eff}) of the waveguide in the direction of the optical axis. The modulation is achieved by varying the material properties of the waveguide (common for optical fibers - achieved by periodic exposure of the silica to UV light) or the physical dimensions of the waveguide (common for Si waveguides).

The most common type of a Bragg grating is the uniform Bragg grating, where the period of the grating is constant with various refractive index profiles (**Fig. 3.9**): rectangular, sinusoidal, triangular, etc. Such gratings are most commonly used in filtering and sensing applications. Here, the traveling light is weakly reflected at each boundary as predicted by Fresnel equations [84], and the overall reflected light from all the periods will add up, in other words the Bragg grating acts as a spatially distributed optical reflector. The reflection is wavelength dependent as constructive interference of the reflected light occurs only for a resonance wavelength or a narrow band around it (depending on the sharpness of the boundary).

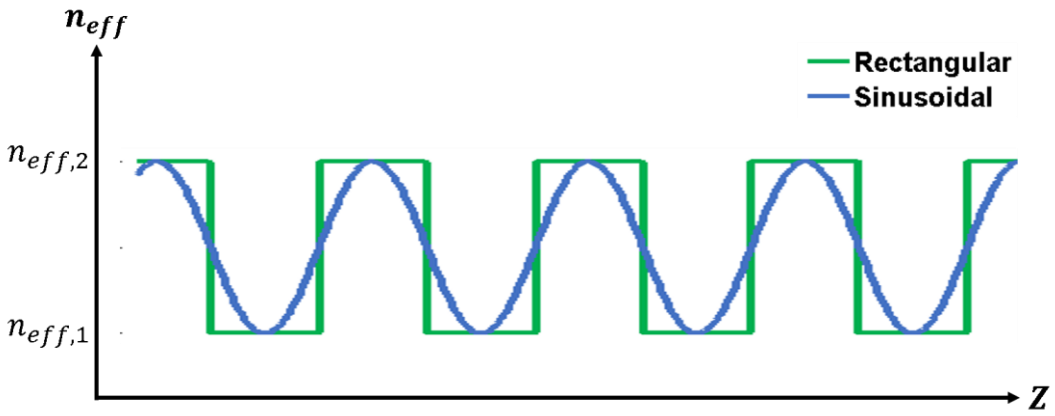

Figure 3.9 Two examples of a refractive index profile along the optical axis (Z) of a uniform Brag grating. The n_{eff} is varied between $n_{eff,1}$ and $n_{eff,2}$ with a sharp boundary – rectangular profile (green) and with a smooth boundary – sinusoidal profile (blue).

The resonance wavelength or Bragg wavelength (λ_B) can be calculated by implementing the Bragg law for a boundary in one period (Λ) of the Bragg grating. Assuming the incident and reflected light have the same n_{eff} (the two modes are identical):

$$\lambda_B = 2\Lambda n_{eff} \tag{3.4.1}$$

We can also define the Bragg propagation constant:

$$\beta_B = 2\pi n_{eff}/\lambda_B \tag{3.4.2}$$

When pumping light into the Bragg grating the driving mode is not necessary equal to the induced mode, we can define the phase mismatch or the detuning:

$$\Delta\beta = \beta - \beta_B = \frac{2\pi n_{eff}(\lambda)}{\lambda} - \frac{2\pi n_{eff}(\lambda_B)}{\lambda_B} \approx -\frac{2\pi n_g}{\lambda_B}\left(\frac{\lambda_B - \lambda}{\lambda_B}\right) \tag{3.4.3}$$

Where $(\lambda_B\text{-}\lambda)/\lambda_B$ is the wavelength detuning and n_g is the group index of the waveguide and it accounts for dependency of n_{eff} on the wavelength. For efficient energy transfer we have to fulfil the phase matching condition [85] meaning $\Delta\beta = 0$, therefore $\lambda = \lambda_B$. The group index (n_g) of the waveguide can be calculated from [84]:

$$n_g(\lambda) = n_{eff}(\lambda) - \lambda\frac{dn_{eff}}{d\lambda} \tag{3.4.4}$$

Using the coupled mode theory (CMT) and assuming lossless grating [83] we can calculate the coupling coefficient (κ) of the grating which can be interpreted as the amount of reflection per unit length. For rectangular index profile we get [59]:

$$\kappa = 2\Delta n/\lambda_B \tag{3.4.5}$$

Where $\Delta n = n_{eff,2} - n_{eff,1}$ is the variation in the effective refractive index (**Fig. 3.9**). For sinusoidal index profile κ is weaker by a factor of $\pi/4$ [59]:

$$\kappa = \pi\Delta n/2\lambda_B \tag{3.4.6}$$

The CMT also predicts the reflection coefficient of a Bragg grating as a function of the wavelength, or in other words the spectral response:

$$r = \frac{-i\kappa \sinh(\gamma L_B)}{\gamma \cosh(\gamma L_B) + i(\Delta\beta/2)\sinh(\gamma L_B)} \tag{3.4.7}$$

Where,

$$\gamma^2 = \kappa^2 - (\Delta\beta/2)^2 \tag{3.4.8}$$

and L_B is the grating length or the overall number of periods.

Using **Eq. 3.4.7** we can simulate the characteristic spectral response of a uniform Bragg grating. **Fig. 3.10** depicts the spectral responses of gratings with $\kappa L_B = 2$ (green curve) and $\kappa L_B = 8$ (blue curve). The grating parameters where chosen to be: $L_B = 125$ μm, $\lambda_B = 1550$ nm, $n_g = 4.04$. The spectral response consists of a reflectivity band (also known as a band-gap or stop-band when discussing transmission through the Bragg grating) cantered at the Bragg wavelength with side-lobes.

The maximum achievable reflection from a grating (the peak of the band gap) can be calculated when $\Delta\beta = 0$ or $\lambda = \lambda_B$ is inserted into **Eq. 3.4.7**:

$$R_{max} = tanh^2(\kappa L_B) \tag{3.4.9}$$

For $\kappa L_B > 3$ the grating is in the "strong grating regime" [86] with reflectivity close to R_{max}. Increasing L_B will not result in improved reflectivity as light does not reach the far end of the grating (increasing κ is not always technically possible).

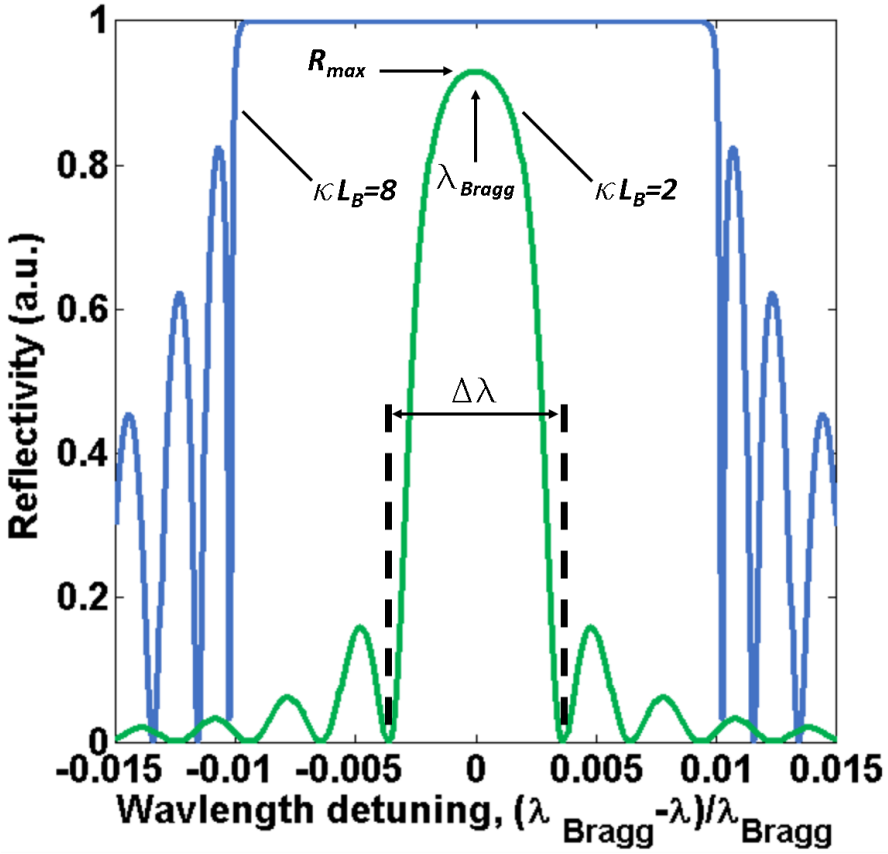

Figure 3.10 Spectral responses of Bragg grating with $\kappa L_B = 2$ and $\kappa L_B = 8$ as a function of wavelength detuning. The grating parameters where chosen to be $L_B = 125$ μm, $\lambda_B = 1550$ nm, $n_g = 4.04$. The peak of the band gap (R_{max}) is centered on the Bragg wavelength (λ_B). The distance between the first two nulls in the spectral response is the grating's bandwidth ($\Delta\lambda$).

The bandwidth of the Bragg grating (the distance between the first two nulls in the spectral response) can be determined also by using the CMT:

$$\Delta\lambda = \frac{\lambda_B^2}{\pi n_g(\lambda_B)}\sqrt{\kappa^2 + (\pi/L_B)^2} \tag{3.4.10}$$

Having a smaller bandwidth is adventurous for some applications as filtering. For gratings with $\kappa L_B < 1$ the grating's bandwidth is almost independent of κ and is inversely proportional to L_B, hence increasing the length would result in narrower bandwidth. For gratings with $\kappa L_B > 10$ the

grating bandwidth is linear with κ and almost independent of L_B, Hence by reducing κ it is possible to narrow the bandwidth of a strong grating [86].

Other notable types of Bragg gratings are the apodized or the chirped Bragg grating and the sampled Bragg grating. The apodized Bragg grating is created when the period of the grating is modified by a constant rate. This results in λ_B being varied with position and the spectral response has no side-lobes with multiple reflection bands. Such gratings have important applications in pulse stretching and compression [87] and dispersion compensation [88]. Sampled Bragg gratings have a sampling function with a period bigger than the grating period applied to the uniform Bragg grating. The sampling function creates sections of the waveguide with no corrugation embedded between the corrugated sections, the result is convolution between the spectral response of the uniform Bragg grating and the sampling function. The sampled Bragg grating exhibit comb-like spectral response and have applications in tunable semiconductor lasers to achieve wide tuning range [89].

3.4.2 Properties of phase shifted Bragg grating

Phase shifted Bragg gratings are optical resonators having the general structure of a Fabry-Perot interferometer (FPI). The resonator is constructed by introducing a defect in the periodicity of a Bragg grating, or alternatively, by bringing two Bragg gratings close together. Each of the Bragg gratings acts as a distributed reflector and is analogous to the mirrors of a FPI, while the defect in the periodicity is the cavity of the FPI. Various cavity lengths where explored and implemented for imaging: from cavities as long as 11.5 cm [90] to sub-micron cavities [52], [91]. The shortest possible cavity length that still fulfils the requirement of constructive interference is equivalent to half of the Bragg wavelength in the waveguide or an acquired round-trip phase shift of π. Such Bragg gratings are called π-phase shifted Bragg gratings and they are the focus of this work. Practically as the Bragg wavelength in the waveguide equals twice the length of the period (**Eq. 3.4.1**) the cavity length would equal the length of one period. **Fig. 3.11** shows a rectangular and a sinusoidal refractive index profiles of a uniform π-phase shifted Bragg gratings.

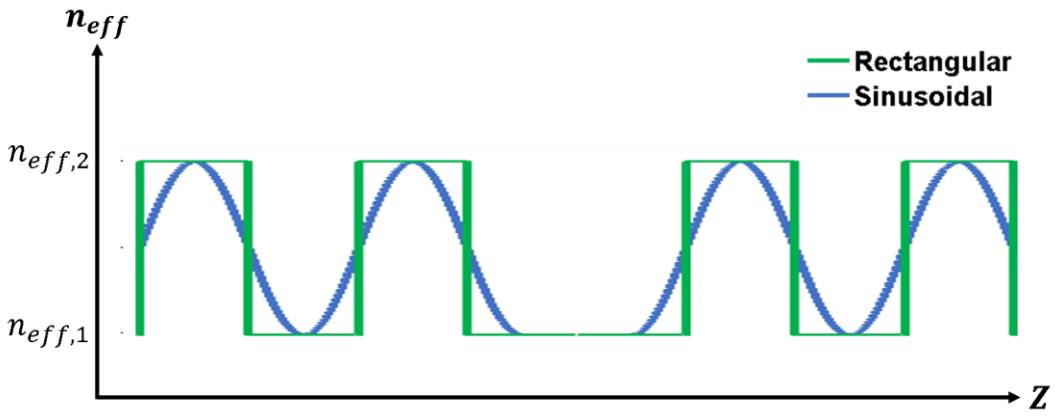

Figure 3.11 Two examples of a refractive index profile with a phase shift along the optical axis (Z) of a uniform Brag grating. The n_{eff} is varied between $n_{eff,1}$ and $n_{eff,2}$ with a sharp boundary – rectangular profile (green) and with a smooth boundary – sinusoidal profile (blue).

We can use the CMT to predict the spectral response of the π-phase shifted Bragg gratings:

$$r = \frac{\Delta\beta}{\kappa}\left[\left(\frac{\gamma}{\kappa\tanh(\gamma L_B/2)} - \frac{i\Delta\beta}{2\kappa}\right)^2 - 1\right]^{-1} \tag{3.4.11}$$

Where $\Delta\beta$ is the detuning from **Eq. 3.4.3** and γ is defined in **Eq. 3.4.8**.

Using **Eq. 3.4.11** we can simulate the characteristic spectral response of a uniform π-phase shifted Bragg gratings. **Fig. 3.12** depicts the spectral responses of gratings with $\kappa L_B = 2$ (green curve) and $\kappa L_B = 8$ (blue curve). The grating parameters where chosen to be: $L_B = 125$ μm (the total length of the two Bragg grating sections), $\lambda_B = 1550$ nm, $n_g = 4.04$. The spectral response is a superposition of the responses of a Bragg grating (**Fig. 3.10**) and of an FPI, resulting in a band-gap and a narrow fringe, both cantered at the Bragg wavelength.

Similar to a Bragg grating (**Fig. 3.10**) the bandwidth of a uniform π-phase shifted Bragg grating increases with larger values of κL_B, while the bandwidth (at FWHM) of the resonance ($\Delta\lambda_R$) decreases due to the increased reflectivity and stronger confinement of light. To estimate the sharpness of the resonance we introduce the resonators quality factor (Q-factor):

$$Q = \lambda_R/\Delta\lambda_R \tag{3.4.12}$$

Where λ_R is the resonance frequency (in our case $\lambda_R = \lambda_B$).

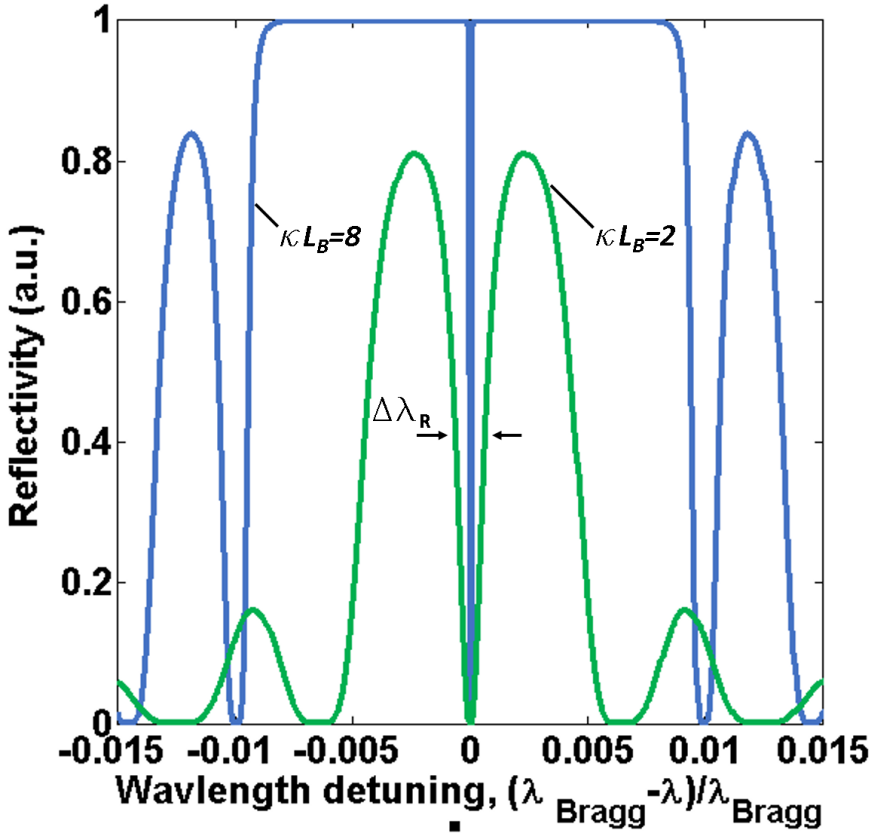

Figure 3.12 Spectral responses of a π-phase shifted Bragg grating with $\kappa L_B = 2$ and $\kappa L_B = 8$ as a function of wavelength detuning. The grating parameters where chosen to be $L_B = 125$ μm, $\lambda_B = 1550$ nm, $n_g = 4.04$. The resonance is centered around the Bragg wavelength (λ_B). ΔK is he FWHM of the resonance.

In general, the Q-factor of a FPI is determined by two loss mechanisms: coupling loss and the waveguide loss. It can be written in the following form [92]:

$$1/Q = 1/Q_L + 1/Q_I \tag{3.4.13}$$

$1/Q$ is the overall decay rate of the energy from the cavity, $1/Q_L$ is the energy decay rate due to any kind of dissipation, and $1/Q_I$ is the decay rate of energy along the propagation direction of the light. The intrinsic Q-factor strongly depends on κ [93]:

$$Q_I \cong \left(\frac{\pi}{4\kappa\Lambda}\right) \exp(\kappa L_B) \tag{3.4.14}$$

While the loss limited Q-factor is [59]:

$$Q_L = \frac{2\pi \cdot n_g \cdot 4.34}{\lambda \cdot 100 \cdot \alpha} \tag{3.4.15}$$

Where α is the is the waveguide propagation loss coefficient in units of [dB/cm]. Both of the Q-factors limit each other, when increasing one the total Q-factor will asymptotically approach the other. Hence, it is impossible to increase the total Q-factor of the π-phase shifted Bragg grating resonator just by designing stronger gratings with larger values of κL_B without tackling the propagation losses. We note that for a loss-less FPI the transmission maximum of the resonance is unity, loss will reduce the maximum transmission. This effect is most notable in strong grating: increasing κL_B will strongly reduce the maximum transmission though the Q-factor would still increase [59]. The can be explained by the fact that higher reflectivity of the distributed Bragg reflectors increases the photon life time in the cavity, meaning that effectively more loss is accumulated.

3.4.3 Phase shifted Bragg gratings in the SOI platform

Phase shifted Bragg gratings were already manufactured before in the SOI platform for application of optical filtering and signal processing, bio-sensing, gas-sensing, and microwave photonics [59]. The devices were created by combining two identical SOI Bragg gratings (see **Section 3.3.4**) with a waveguide section between them that functions as the optical cavity of the resonator. The Bragg gratings were realized by adding side wall corrugation to the strip [64], [79], [89] slot [67], and rib [77] waveguides. In the latter case the corrugation can be added either to the slab or strip parts of the waveguide.

The most commonly used type of devices are π-phase shifted waveguide Bragg gratings (π-WBG). Here, the lengths of the Bragg gratins are chosen to be equal so the reflectivity is equal and the light confinement in the cavity is optimal, resulting in sharpest resonances. The length of the cavity section is chosen to be the shortest possible, i.e. equal to the corrugation period, resulting in the strongest confinement of the optical field around the cavity section. Both of those requirements come from the need for miniaturized and high Q-factor resonator, which are attractive for sensing applications (see **Section 3.4.4**).

Ultrasound sensor constructed around a π-WBG realized in a strip waveguide with a cross-section of 220 x 500 nm, $L_B = 125$ μm, and an SiO_2 cladding of ~ 2 μm (commercially available from Teraxion, Québec, Canada) was attempted before [52]. The resulting sensor was dominated by surface acoustic waves propagating at the SiO2-water interface and generated at Rayleigh angles. The π-WBG sensor was insensitive to longitudinal ultrasonic waves required for image formation due to the large acoustic impedance mismatch between water and the SiO_2 cladding resulting in most of the waves being reflected from the interface. As the sensor was deeply embedded in the cladding the optical field in the resonator was not exposed to this interface which prevented detection.

In order to circumvent this problem, we designed and manufactured (for details see **Section 6.1** and **Section 6.2**) several π-WBGs based on strip and rib waveguides, with $L_B = 125$ μm and polymer top cladding of ~ 5 μm consisting of a standard I-line photoresist (exact model is not specified by the manufacturer). The refractive index of this resist in the near-infrared wavelengths is very close to the refractive index of SiO_2 but the acoustic properties of those materials are very different. The desirable Bragg wavelengths for the π-WBGs are ~ 1550 nm because around this wavelength both silicon and silica fibres offer minimal optical attenuation and there is a large range of tuneable light sources and erbium doped optical fibre amplifiers available.

Table 3.1 lists the design parameters used for each device. Devices A8, A9, B8, B9 are based on a strip waveguide with a cross section of 220 × 500 nm^2 and Λ = 320 nm, devices with similar parameters and identical manufacturing process were reported in [64], [79]. The simulated n_{eff} of such a waveguide is 2.452 and the expected Bragg wavelength is 1569 nm (**Eq. 3.4.1**) yet the reported Bragg wavelength for a π-WBGs with Δw = 40 nm is ~1561 nm [64]. The 8 nm shift is attributed to non-uniformities in the waveguide thickness due to nonmetric variations in wafer thickness and process non-uniformities. In fact, change of 10nm in the π-WBG thickness results in a more than 20 nm spectral shift of the resonance [79]. The design parameters of A8, A9, B8, B9 were chosen to be identical to [64] in order to account for possible shifts in the resonance wavelength due to process variations and acquire a Bragg wavelength as close as possible to 1550 nm.

Device #	Δw (nm)	w_{core} (nm)	w_{slab} (nm)	Λ (nm)	L_{cavity} (nm)
A2	100	450	700	300	300
A3	90	450	700	300	300
A4	80	450	700	300	300
A5	70	450	700	300	300
A6	60	450	700	300	300
A7	50	450	700	300	300
A8	25	500	-	320	320
A9	35	500	-	320	320
B2	110	450	700	300	300
B3	120	450	700	300	300
B4	130	450	700	300	300
B5	140	450	700	300	300
B6	150	450	700	300	300
B7	160	450	700	300	300
B8	30	500	-	320	320
B9	40	500	-	320	320

Table 3.1 Design parameters of π-WBG manufactured with top cladding made of standard I-line photoresist.

Devices A2-A7 and B2-B7 are based on a rib waveguide with slab cross section of 150 × 700 nm^2, ridge cross section of 70 × 450 nm^2. The ridge width was chosen to be under 750 nm in order to fulfil the single mode condition [66]. The simulated n_{eff} of such a waveguide is 2.55 which is larger than the n_{eff} of the strip waveguides resulting in larger Bragg wavelength of 1632 nm that is outside of the sweep range of the laser source. In order to compensate for the increase in resonance wavelength the period was reduced to Λ = 300 nm which would result in expected Bragg wavelength of 1530 nm.

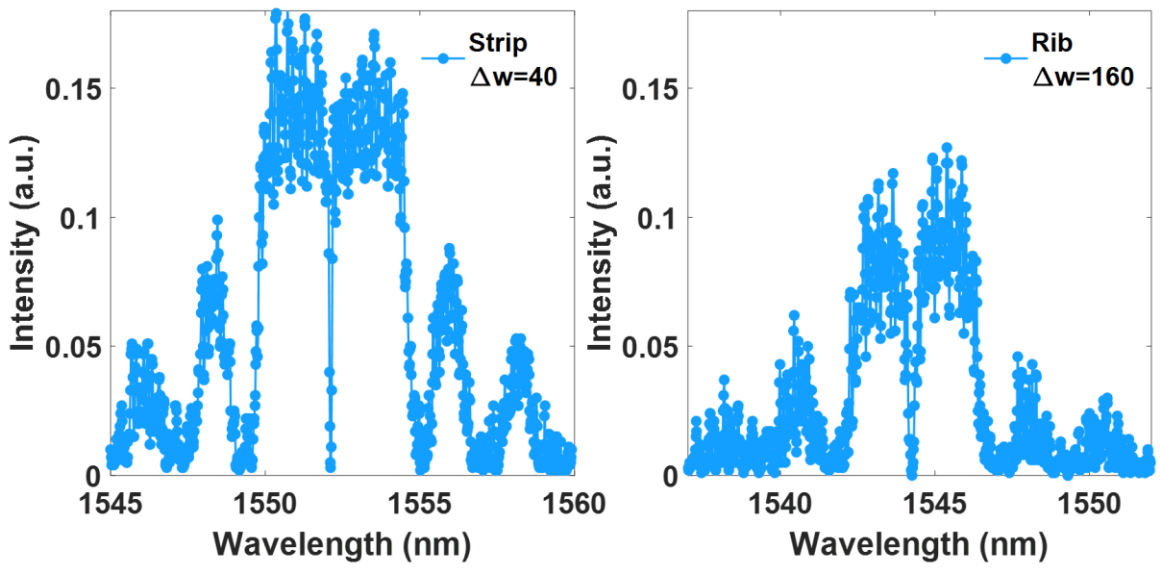

Figure 3.13 Reflection spectra of the strip and rib π-WBG devices. Strip parameters: cross section, 220 × 500 nm^2 ; Λ = 320 nm; Δw = 40 nm; $L_B = 125$ µm. Rib parameters: slab cross section, 150 × 700 nm^2 ; strip cross section, 70 × 450 nm^2 ; Λ = 320 nm; Δw = 40 nm; $L_B = 125$ µm.

Fig. 3.13 depicts two characteristic spectra of the strip and rib π-WBG, acquired from device B9 and device B7 respectively for details on optical measurement setup see **Section 6.3)**. As theoretically predicted (**Eq. 3.4.11**) the shape of the spectra consists of a bandgap with side lobes and in the middle of it a single resonance. The width of the bandgap, the sharpness of the resonance and the maximum value of the reflectivity depends on κL_B (**Fig. 3.12**). From the spectra it can be deduced that the rib π-WBG has weaker Bragg gratings, as in both devices $L_B = 125$ µm is identical, the difference originates in the weaker coupling coefficient of the rib grating. This is evident in the narrower bandgap, lower reflectivity, and wider resonance of the rib spectrum.

Fig. 3.14 depicts a top-view electron microscopy image of two section of a rib π-WBG. The rib and slab section are clearly visible. The red arrow indicates the location of the optical cavity and the corrugation, Δw, is indicated by the black arrows. The shape of the index profile significantly deviates from the designed rectangular profile and more closely resembles sinusoidal profile. This is attributed to fabrication imperfections during lithography process and can potentially be accounted for during design if process parameters are provided by the foundry or deduced by post-lithography simulations [78].

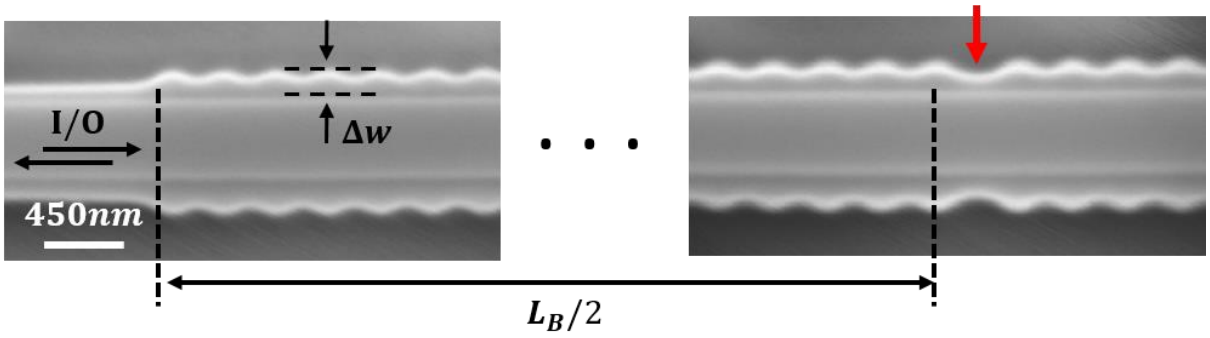

Figure 3.14 Electron microscopy image of two sections of a rib π-WBG. I/O, silicon rib waveguide guiding light into the π-WBG; Δw, corrugation; Red arrow, location of the optical cavity section. The image was acquired with the help of Dr. Fabio Del Giudice and Prof. Jonathan Finley at the facilities of the Walter Schottky institute, Technical university of Munich, Germany.

The deviation of the index profile from the design alongside other process non-uniformities results in significant performance mismatch between the designed and fabricated devices. **Fig 3.15** depicts measured optical parameters of the A8, A9, and B2-B9 devices located on four randomly selected chips from the same SOI wafer (for details on chip location on the SOI wafer and resonance uniformity across the wafer see **Appendix A**). The spectrum of devices A2-A7 showed no distinguishable resonance and very weak bandgap, indicating that corrugations under 100 nm of the rib waveguides with slab width of 700nm result in weak Bragg gratings.

Fig. 3.15a depicts the effect of Δw on the Bragg wavelength for the strip and rib π-WBGs. For both designs the stronger is the corrugation the larger is the Bragg wavelength. The corrugated sections are wider thus having larger n_{eff} which results in redshift of the Bragg wavelength (**Eq. 3.4.1**). The redshift is stronger for the strip design because the optical mode is less confined and is more strongly affected by the corrugation (**Fig. 3.3** vs **Fig. 3.2**). In both designs inter-chip variations in silicon thickness result in ~5 nm shift of the resonance wavelength regardless of Δw. **Fig. 3.15b** depicts the effect of Δw on the Q-factor of the resonance for the strip and rib π-WBGs. For both designs the stronger is the corrugation the larger is the Q-factor. Stronger corrugation results in larger n_{eff} contrast between the corrugated and un-corrugated section, increasing the coupling coefficient and the overall reflectivity of the grating (**Eq. 3.4.5**). This in turn narrows the resonance and increases the Q-factor (**Eq. 3.4.14**). The increase in the Q-factor with Δw is much stronger for the strip design, again because the optical mode is less confined. This can be explained by the exponential dependence of the Q-factor on the coupling coefficient (**Eq. 3.4.14**), which means that the rate at which the Q-factor increases with κ for stronger gratings (stronger κ) is faster

than for weak gratings (weaker κ). This can be also observed in the fluctuations of the Q-factor due to inter-chip variations in silicon thickness. The thickness variation result in variations of the n_{eff} of the corrugated and un-corrugated sections resulting in small fluctuations in κ between the devices. Strip devices with larger κ experience inter-chip fluctuations of the Q-factor as large as ~0.5×10^4, while the rib devices with weaker κ experience much weaker inter-chip fluctuations of ~ 0.1×10^4.

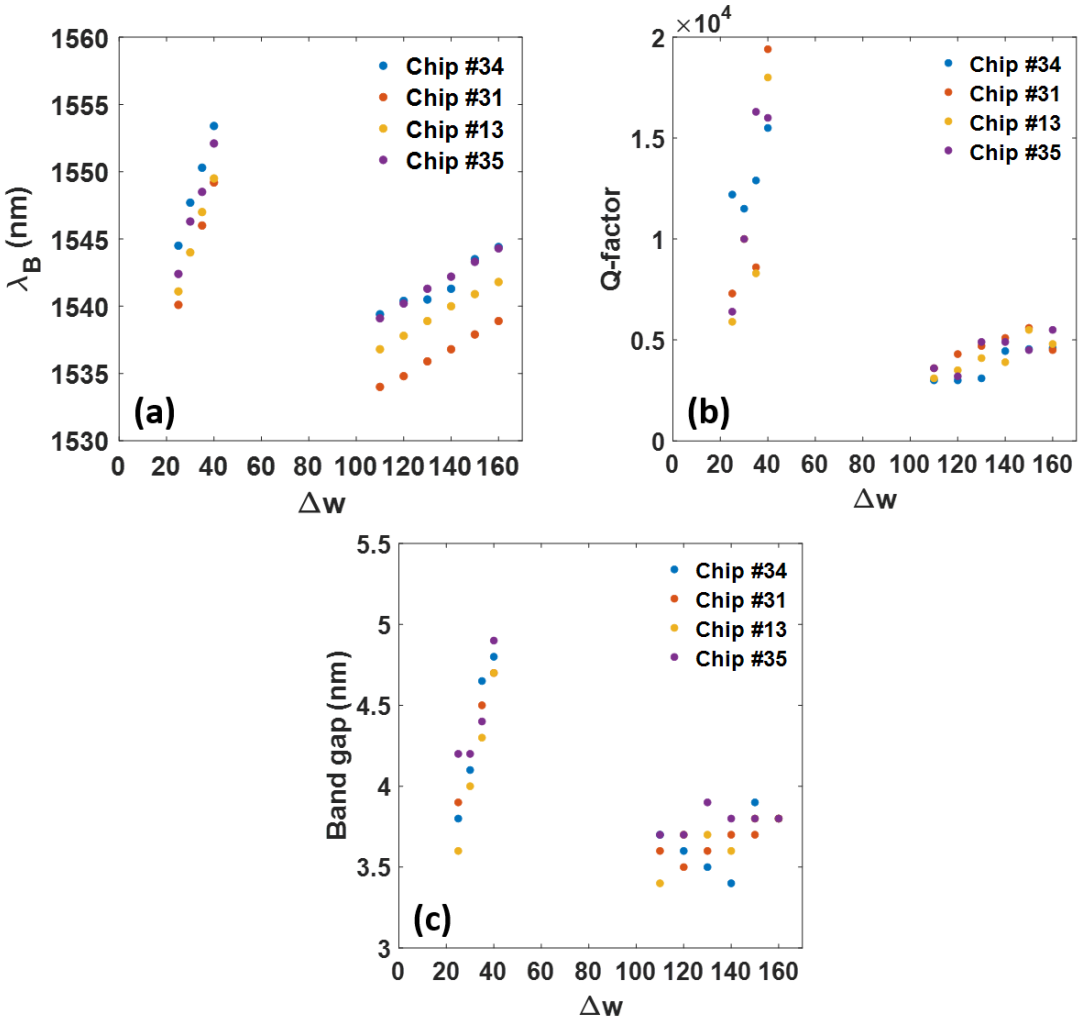

Figure 3.15 Measured optical parameters of the strip and rib π-WBG devices with resist cladding located on four randomly selected chips from the same SOI wafer **(a)** Bragg wavelength of the rib and strip π-WBGs as function of the corrugation. **(b)** Q-factor of the rib and strip π-WBGs as function of the corrugation. **(c)** Width of the bandgap of the rib and strip π-WBGs as function of the corrugation.

Fig. 3.15c depicts the effect of Δw on the Bragg band gap for the strip and rib π-WBGs. For both designs the stronger is the corrugation the wider is the bandgap (**Eq. 3.4.10**). The increase in

bandgap is stronger for the strip design again because of the weaker confinement of the mode in the waveguide. **Eq. 3.4.10** shows that for weaker κ the rate at which the bandgap increases with κ is slower than for the rate for stronger κ. For this reason, strip devices which have larger κ experience inter-chip fluctuation of the bandgap as large as ~0.7 nm, while the fluctuations of the rib design and more moderate and smaller than 0.5 nm.

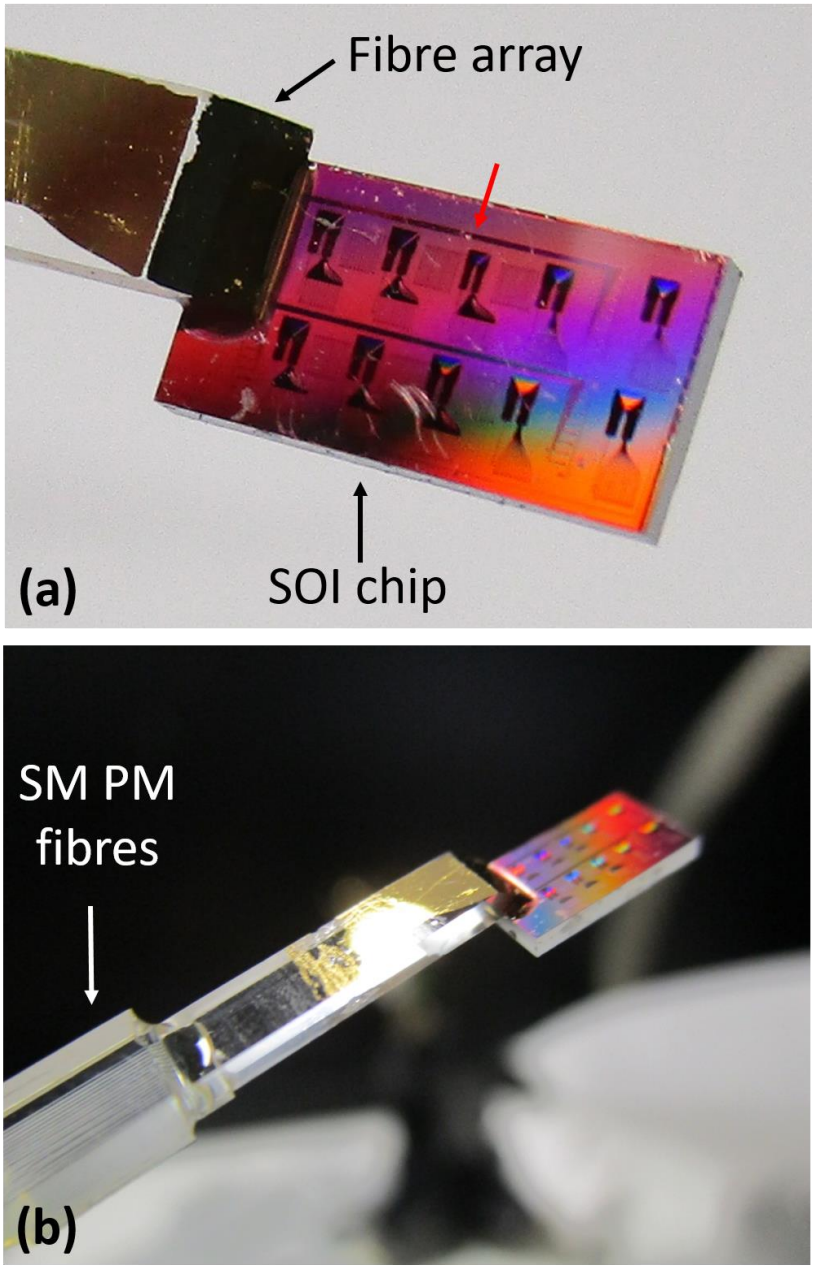

Figure 3.16 Photographs of the SOI chip with the π-WBGs connectorized to a SM PM fibre array. **(a)** The red arrow indicated the location of the π-WBGs. During acoustic characterization this side was exposed to ultrasound. **(b)** individual fibres are visible emerging from the array.

In conclusion, all the rib devices resulted in weaker gratings compared to the strip devices due to the fact that the optical mode is more confined in the rib design and is less sensitive to variations that occur on the side walls. The strongest Q-factor achieved in the rib design with strongest corrugation of Δw = 160 nm could be compared only to the weakest Q-factor achieved for the strip design with weakest corrugation of Δw = 25 nm. Here the choice of the rib design with the lower propagation losses for achieving larger values of the Q-factor (**Eq. 3.4.14**) did not justify itself. In the future, rib waveguides with slab width under 700 nm or corrugation of the strip section [77] could be considered for improving the optical parameters of the rib π-WBGs.

After optical characterization of the π-WBG and before moving to characterization of acoustic performance in the next chapter it is required to perform permanent connecterization (see S**ection 6.2.3** for details) of the π-WBG to an optical fibre for stable readout of the sensor during charecterization experiments that are performed in aquatic and turbulent environment (see **Section 6.5** for details). **Fig. 3.16a** and **Fig. 3.16a** depicts the SOI chip with the location of the π-WBG devices marked by red arrow. The attached fibre array is visible on the left side of the chip, individual SM PM fibres are also visible emerging from the array. Only a single fibre was connectorized to a single Strip π-WBG with Δw = 40 nm. The latter device was chosen because it has the highest Q-factor from all manufactured devices.

3.4.4 Ultrasonic detection with phase shifted Bragg gratings

π-phase shifted Bragg gratings were studied extensively for imaging applications. Several key parameters are crucial for high quality image formation: Sensitivity to ultrasound – especially when imaging small absorbers that produce weak ultrasonic signals or absorbers at depths that attenuate high frequency ultrasound. Combination of the both limits imaging depth; Detection bandwidth – bandwidth mismatch between the generated signal and the detector directly effects the sensitivity. Sensor size- small detection element size is important for high resolution imaging, as the sensitivity is inversely proportional to the doctor size the trade-off between the two parameters poses a great challenge in detector design. In this chapter, we will survey the relation between the properties of π-phase shifted Bragg and those parameters.

Sensitivity

The sensitivity to pressure (S) of an optical resonator can be defined as the reflected optical power (P_R) modulation per unit of incident acoustic pressure (p) [43]:

$$S = \frac{dP_R}{dp} = \frac{dP_R}{d\phi} \cdot \frac{d\phi}{dp} \tag{3.4.16}$$

where $\phi = 4\pi n_{eff} l/\lambda$ is the optical phase, n_{eff} is the effective refractive index of the waveguide, l is the resonator's length, and λ is the wavelength.

The $dP_R/d\phi$ term is the side slope of the resonance in the reflection spectra (**Fig. 2.2**) and it accounts for the amplification of the detected signal through the ability of the resonator to confine light. When tuning the interrogation laser to the FWHM of the resonance, any perturbation that shifts the resonance will induce variations in the reflected intensity. The sharper the slope is, the stronger are the variations. Hence π-phase shifted Bragg gratings are more sensitive with larger values of κL_B,or the Q-factor [48].

The $d\phi/dp$ term on the other hand, known as the acoustic phase sensitivity (S_ϕ), accounts both for the properties of the materials the detector is constructed from and the positioning of the detector relative to the acoustic source. This merit excludes tunable parameters that effect the SNR, like the Q-factor, acquisition system, etc. Hence, it is the most basic 'signature' of the detector's material composite and geometry. The phase sensitivity can be written as follows:

$$S_\phi = \frac{d\phi}{dp} = \frac{2\pi n_{eff} l}{\lambda} \cdot \left(\frac{1}{n_{eff}} \frac{dn_{eff}}{dp} + \frac{d\varepsilon_z}{dp} \right) = \frac{2\pi n_{eff} l}{\lambda} \cdot S_\lambda \tag{3.4.17}$$

where S_λ is the normalized sensitivity and ε_z is the strain along the optical axis.

The change in phase can be attributed to two mechanisms: change in n_{eff} of the waveguide due to density changes through the elasto-optic effect, and change in l due to strain experienced by the waveguide. The strain induced changes and elasto-optic induced changes compete with each other: Shrinkage of the waveguide dimension due to strain leads to reduction of n_{eff}, while the elasto-optic effect induced by the same strain increases n_{eff}.

As an example we can consider a π-WBG sensor embedded in silica cladding with TE mode exited

in two different sensing configurations. First when ultrasound is detected through the waveguide cross-section (**'forward detection'**) and second when ultrasound is detected perpendicular to the optical axis of the waveguide (**'side detection'**). As the Q-factor is identical in both cases it is sufficient to examine only S_λ at the different sensing configurations.

In the forward detection scheme, the acoustic wave is propagating along the optical axis, so the applied stress is $\sigma_z = P$, and the elastic deformation perpendicular to the optical axis is $\varepsilon_x = \varepsilon_y = 0$. Using the generalised Hooke's law and accounting for the elasto-optic effect in an isotropic cubic material, we obtain the following relationships:

$$\varepsilon_z = -\frac{(1+\nu)(1-2\nu)}{(1-\nu)E}P \tag{3.4.18}$$

$$\Delta n_x = \Delta n_y = \frac{(\nu C_1 + C_2)}{1-\nu}P \tag{3.4.19}$$

where Δn_x and Δn_y are the perturbations of the refractive index perpendicular to the optical axis; C_1 and C_2 are the elasto-optic constants; E is Young's modulus, and ν is the Poisson ratio. The values of those parameters for silicon and silica can be found in the literature [65]. The contribution of the strain component to S_λ was evaluated directly from **Eq. 3.4.18,** and the contribution due to change in n_{eff} was simulated using **Eq. 3.4.19** and a vectorial mode solver [61]. The normalised sensitivity was found to be $S_{\lambda,forward} = -5.5 \times 10^{-6}$ MPa^{-1}. The negative sign implies that the elastic waveguide deformation has a larger impact than the elasto-optic effect.

In the side detection scheme, the acoustic wave impedes on the waveguide perpendicularly; hence, $\sigma_y = P$ and $\varepsilon_x = \varepsilon_z = 0$. The normalised sensitivity for the side detection geometry was previously found to be $S_{\lambda,side} = 4.7 \times 10^{-6}$ MPa^{-1} [65]. In that case, the positive sign indicates the dominance of the elasto-optic effect.

Comparing the absolute value of the normalised sensitivity of the two detection geometries shows that the forward detection geometry is ~20% more efficient.

Dominance of the elastic deformation of the waveguide is also commonly the case of sensors constructed from soft polymer materials (smaller Young's modulus) [94]. In general, detectors constructed from polymers [94] tend to have larger values of S_λ by one order of magnitude compared to detectors constructed from silicon [65] or silica [41]. Yet, polymers are not always

the favourable material for detector construction as the achievable refractive index contrast in the polymer platform and the manufacturing techniques result in higher optical losses that affect the $dP_R/d\phi$ term and the sensor size (see **next Section**). The resulting Q-factors tend to be smaller by at least one order of magnitude [24] compared to other platforms like silica [41]. The trade-off between the two trends has to be carefully considered when choosing a platform for detector development.

Sensor size

Sensor size refers to the dimensions of the sensing element in the sensor. The area of the sensing element that is perpendicular to axis on which ultrasound propagates to the detector effects the sensitivity and the lateral resolution. The larger this area is the more pressure is collected and transformed to signal [23], but at the same this area is inversely proportional to the lateral resolution [8].

In π-phase shifted Bragg gratings the majority of the sensing occurs around the cavity section where most of the optical field is confined. Along the optical axis the optical field is not well confined by the cavity as the reflective surfaces of the FPI are distributed Bragg reflectors. The extent to which the field decays to e^{-1} of its maximum value, or the sensing length (L_S) along the optical axis (z), can be calculated using the CMT theory. The amplitude of the electric field along the optical axis of the π-phase shifted Bragg gratings can be written as [48]:

$$A(z) = (1 - |r|^2)^{-1} \cdot \exp(\frac{\kappa L_B}{2}) \cdot \exp(-\kappa \left| z - \frac{L_B}{2} \right|) \tag{3.4.20}$$

where r is defined by **Eq. 3.4.11**. The $\exp(\kappa L_B/2)$ term scales the amplitude and amplifies it exponentially with κL_B. From **Eq. 3.4.20** we can see that the intrinsic Q-factor (Q_I) also increases exponentially with κL_B, this indicates the direct relation between the amount of confined light around the cavity and the sensitivity the of π-phase shifted Bragg grating. The $\exp(-\kappa|z - \kappa L_B/2|)$ term is the decay of the electric field along the optical axis, L_S can be estimated from it to be κ^{-1}.

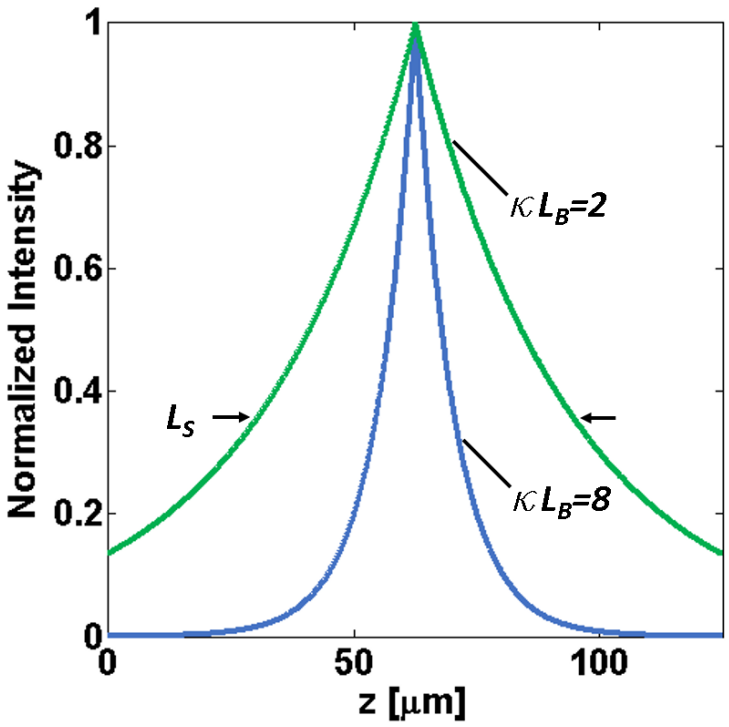

Figure 3.17 Spatial distribution of the optical field within the grating centered around the π-phase shifted section, for gratings with $\kappa L_B = 2$ and $\kappa L_B = 8$. The grating parameters where chosen to be $L_B = 125$ μm, $\lambda_B = 1550$ nm, $n_g = 4.04$. L_s is he FWHM of the spatial distributions, it corresponds to the sensing length of the π-phase shifted Bragg grating.

Using **Eq. 3.4.20** we can simulate the electric field distribution along the optical axis of a uniform π-phase shifted Bragg gratings. **Fig. 3.17** depicts the normalized intensity of the electric field of gratings with $\kappa L_B = 2$ (green curve) and $\kappa L_B = 8$ (blue curve). The grating parameters where chosen to be: $L_B = 125$ μm (the total length of the two Bragg grating sections), $\lambda_B = 1550$ nm, $n_g = 4.04$. We observe that for higher values of κL_B the optical field is more confined around the cavity and L_S is smaller, this can be attributed to the increase in the reflectivity of the Bragg gratings.

Fig. 3.18 depicts a simulation of the electric field distribution along the optical axis for for a π-FBG written in a single mode polarization maintaining fiber (SMF28) with $\kappa = 25.8$ cm^{-1} and $L_B = 2$ mm, and for for a π-WBG grating written in a Si strip waveguide (cross section of 220 × 500 nm^2 with SiO2 cladding) with $\kappa = 288$ cm^{-1} and $L_B = 125$ μm. The L_S for the π-FBG is calculated to be 388 μm while for the π-WBG it is only 35 μm. Those results are supports by experimental studies found in the literature: For the π-FBG with $\kappa = 25.8$ cm^{-1} the L_S was

measured to be ~300 μm which is in a good agreement to the predicted value of $\kappa^{-1} = 388$ μm [48]. For a π-WBG with $\kappa = 288$ cm^{-1} the L_S was measured to be ~100 μm while $\kappa^{-1} = 35$ μm [52].

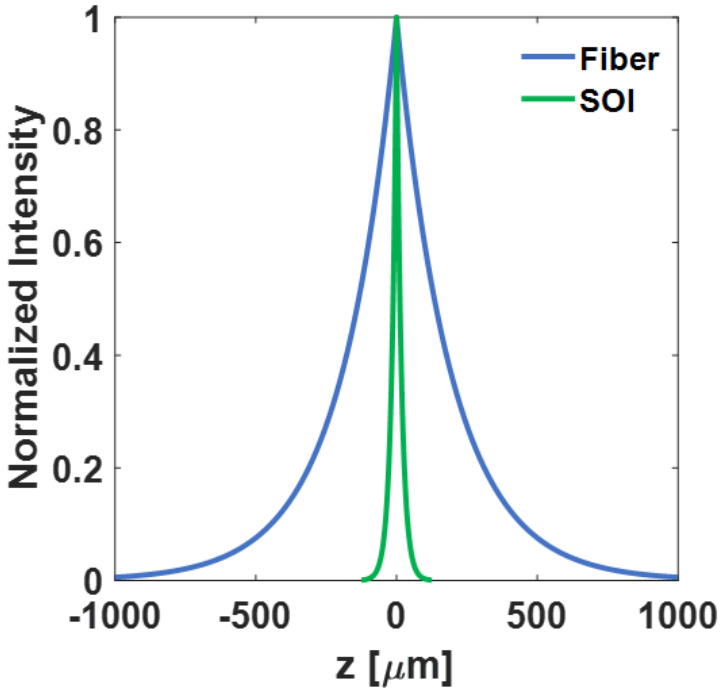

Figure 3.18 Spatial distribution of the optical field within the grating centered around the π-phase shifted section, for a grating realized in a single mode PM fiber with $\kappa L_B = 5.1$ and a grating realized in an SOI chip with $\kappa L_B = 7.2$.

We also experimentally verify the sensors size by scanning the sensors over an ultrasonic point source generated by focusing pulsed laser onto a piece of black tape (see **Section 6.3**), both of the sensors were positioned at the same distance with the optical axis of the Bragg grating parallel to the *x* axis (**Fig. 3.19a** and **Fig. 3.19d**). The recorded B-scans of the sensors along the *x* axis show that ultrasonic signal arrive exactly at the same time for a sections of ~ 100 μm and ~ 450 μm around the π-phase shifted section for the π-WBG and π-FBG respectively (**Fig. 3.19b** and **Fig. 3.19e**). Those values are in a good agreement to the results previously reported in literature and predicted by our theoretical analysis. The measured sensor sizes size in this dimension are much larger than the acoustic point source, and the uncertainty in the location of the point source is on the order or the sensor size, which could result in smearing of the image in this dimension The white arrow in **Fig. 3.19b** indicates signal generated directly at the Bragg grating due to absorption of stray laser light by the silicon chip. The B-scans along the *y* (**Fig. 3.19c** and **Fig. 3.19f**) show a

parabolic profile around the π-phase shifted section, indicating that in this dimension the sensor side is smaller or on the same order as the ultrasonic source.

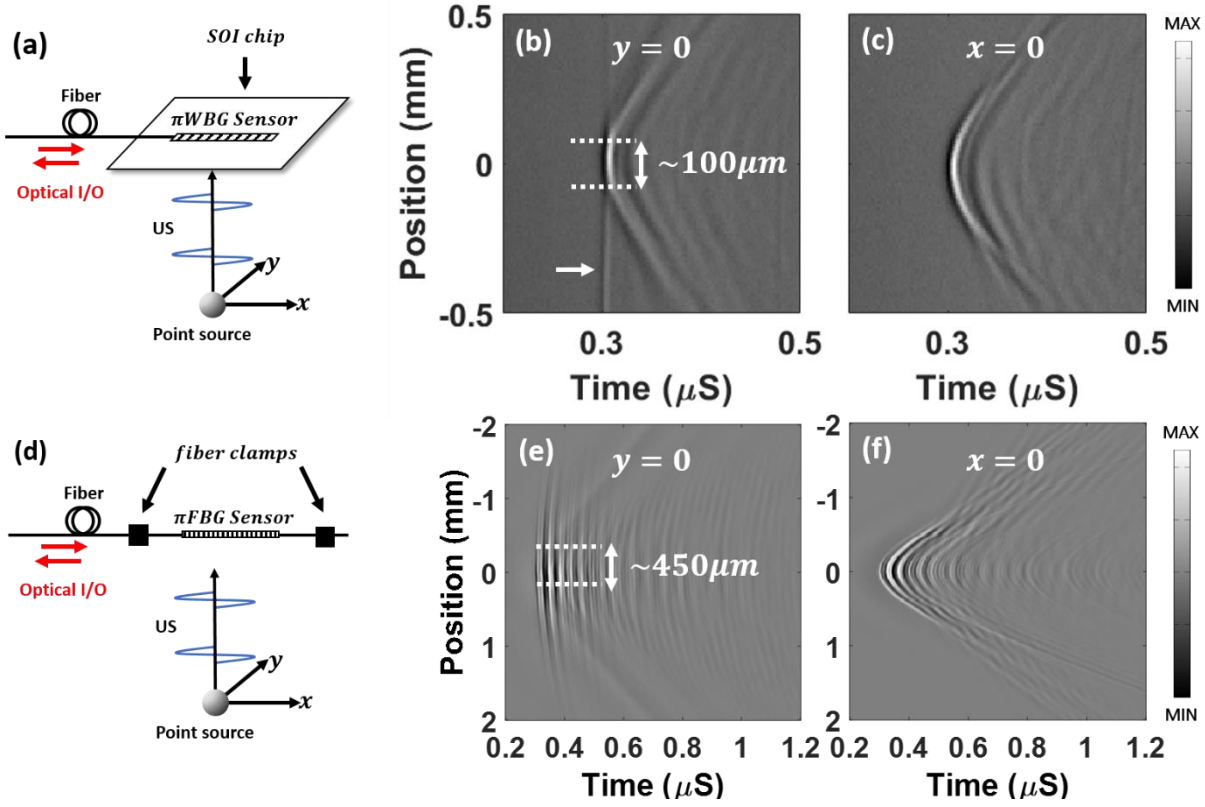

Figure 3.19 Measurement of the sensor size of π-WBG and the π-FBG sensors along the optical axis and perpendicular to the optical axis of the Bragg gratings. **(a)** Schematic of the π-WBG sensor relative to the ultrasound point source. The π-WBG sensor was facing the source. **(b)** and **(c)** B-scans of the π-WBG sensor on top of the point source along the *x* and y axes respectively. **(d)** Schematic of the π-FBG sensors relative to the ultrasound point source. **(e)** and **(f)** B-scans of the π-FBG sensor on top of the same point source along the *x* and y axes respectively.

Along the optical axis the sensor size is defined by the achievable κ in each platform, while perpendicular to the optical axis the sensor size is defined by the optical field distribution of the exited mode in the waveguide. The extend of this distribution can be approximated by the cross-section of the waveguides core. For the fibre platform it is ~ 8-9 μm and for the SOI platform it is 200-500 nm. Both the κ and the cross-section of the waveguides core are dependent on the achievable optical index contrast in each platform. Hence platforms like SOI that offer higher index contrast are preferable for construction of Bragg grating-based ultrasound sensors as smaller sensor size are attainable resulting in improved lateral resolution.

Comparison of the B-scans along the *x* and *y* axes of each sensor (**Fig. 3.19b** vs **Fig. 319c** and **Fig. 3.19e** vs **Fig. 3.19f**) indicates an inherent drawback of the π-phase Bragg grating-based design: One of the sensor dimensions would always be larger than the other, Which would always result in line sensors regardless of the achievable miniaturization. This means that imagine with such type of sensors would always result in anisotropic resolution and smearing of the image in one axis.

Frequency response and Bandwidth

The frequency response of a sensor to ultrasound signals is usually determined by the thickness of the sensing element. The boundaries between the sensing element and the surrounding or backing and matching layers from a resonator for acoustic waves. Constructive interference occurs when the thickness of the resonator (l) equals to half of the acoustic wavelength in that media. The resonance frequency can be determined from:

$$f_0 = v_0/2l \tag{3.4.21}$$

The bandwidth of the resonance is determined by the reflection coefficients at the boundaries (see **Eq. 2.1.16-17**) which are defined by the acoustic impedance of the different layers. In the case of optical resonator-based sensor the frequency response is determined by two concurrent processes [95]:

1. Optical resonance stability
2. Acoustic resonance formation

The first process accounts for the change in the amount of energy confined in the resonator due to the shift of the resonance wavelength as a result from change in the optical properties of the cavity due to interaction with the ultrasound wave. Time is required for the resonator to gradually accumulate energy and go back to the steady state. For resonators with higher Q-factor more energy is confined in the cavity hence their recovery takes longer. The resonance limited cutoff frequency (f_0) can be calculated from [95]:

$$f_c = \omega/Q \tag{3.4.22}$$

Where ω is the optical angular frequency and Q is the Q-factor. For the π-WBG and π-FBG sensors with Q ~ 10^5 and optical wavelength around 1550 nm the cutoff frequency is on the order of tens of GHz indicating that the optical resonance stability is negligible for those sensors.

The second process accounts for the interaction between the varies layers that form the sensor and the ultrasound waves. Here we must distinguish between optical interfaces and acoustic interfaces. Optical interfaces are formed by two materials with non-zero refractive index contrast (Δn) while acoustic interfaces are formed by two materials with non-zero acoustic impedance contrast (ΔZ). The stronger are the contrasts the stronger would be the optical and acoustic confinement and the sharper would be the resonances.

The optical refractive index of depends on the electromagnetic properties of the material (electric permittivity and magnetic permeability) while the acoustic impedance depends on elastic properties of the material (Young's modulus, Poisson's ratio, and the density). As there no direct relation between the two properties an optical interface might be invisible to sound in vica versa. This means that the optical cavity dimensions cannot often be considered as the thickness of the resonator and used as first approximation for l in **Eq. 3.4.21**.

A good example is an optical fibre: the index contrast between the core and the cladding in a standard SMF28 fibre is $\Delta n \approx 0.001$ which is sufficient to confine the optical mode in a waveguide with ~ 9 μm diameter. Yet, the acoustic impedance contrast between the core and the cladding is $\Delta Z \approx 0$ making this interface invisible to ultrasound. On the other hand, the acoustic impedance contrast between the cladding and the acrylic coating of the fibre is $\Delta Z \approx 11.35$ MRayl which results in the acoustic resonance frequency being determined by the diameter of the fibre cladding. For a fibre with standard diameter of 125 μm and $v_0 = 5570$ m/s for longitudinal acoustic waves in silica the resonance frequency is 22.2 MHz. The bandwidth depends on ΔZ and cannot be directly estimated from **Eq. 3.4.21.** Instead we use a model similar to ref. [96]. The frequency response ($P(k)$) of a sensor based on optical resonator embedded in the core of the fibre can be written as:

$$P(k) = \frac{1}{l}\int P_T \, dx \tag{3.4.23}$$

Where x is the dimension perpendicular to the optical axis of the fibre, k is the wavenumber, and the integration is performed all over the diameter of the cladding $l = w_{cladd}$ (**Fig. 3.20a**). P_T is the infinite sum of all the resonating waves in volume P_1 to P_i in **Fig. 3.20a. Fig. 3.20b** depicts the normalized frequency response of the fibre as a function of the fibre diameter. As expected, when the fibre diameter decreases the resonance frequency increases while the fractional bandwidth around that frequency stays the same as it mostly depends on ΔZ. **Fig 3.20c** depicts the simulated normalized frequency response of the same fibre with acrylic coating and when this coating is stripped and the fibre is submerged in water. Similar to optical resonators the bandwidth narrows and the resonance becomes sharper when ΔZ increases.

In order to perform the prediction of this model we measured the frequency response of a π-FBG sensor written in the same single mode fibre. The sensor recorded signal emitted from an ultrasonic point source generated by illuminating a 10 μm black polystyrene microsphere with a pulsed laser (see **Section 6.4**). The theoretical frequency content emitted from such a sphere is depicted in **Fig. 3.20d**, it was acquired using the model in ref. [13]. The measured and simulated frequency responses of the π-FBG sensor are depicted in **Fig. 3.20e**. In general, there is a good agreement between the two. When the frequency content of the microsphere is overlaid on the simulated response from **Eq. 3.4.23** the visibility of the theoretical peaks more closely resembles the peaks in the measured frequency response. This model can be improved if the acrylic layer is regarded as a matching layer and its frequency response is taken into account [21].

For the π-WBG sensor no similar model exists yet that can predict the frequency response of the sensor but it was experimentally measured to be ~ 50 MHz [52], this result was limited by the interrogation system. Higher bandwidth allows to resolve with finer accuracy the time difference between two ultrasonic signals arriving from two absorbers at different depths, therefore the axial distance between the absorbers can be determined more accurately and the axial resolution is increased [8]. When the sensor is translated laterally relative to the ultrasonic source the detection bandwidth and the resonance frequency would shift toward the lower frequencies [95], this is because the effective thickness of the sensor as seen from the source is increased.

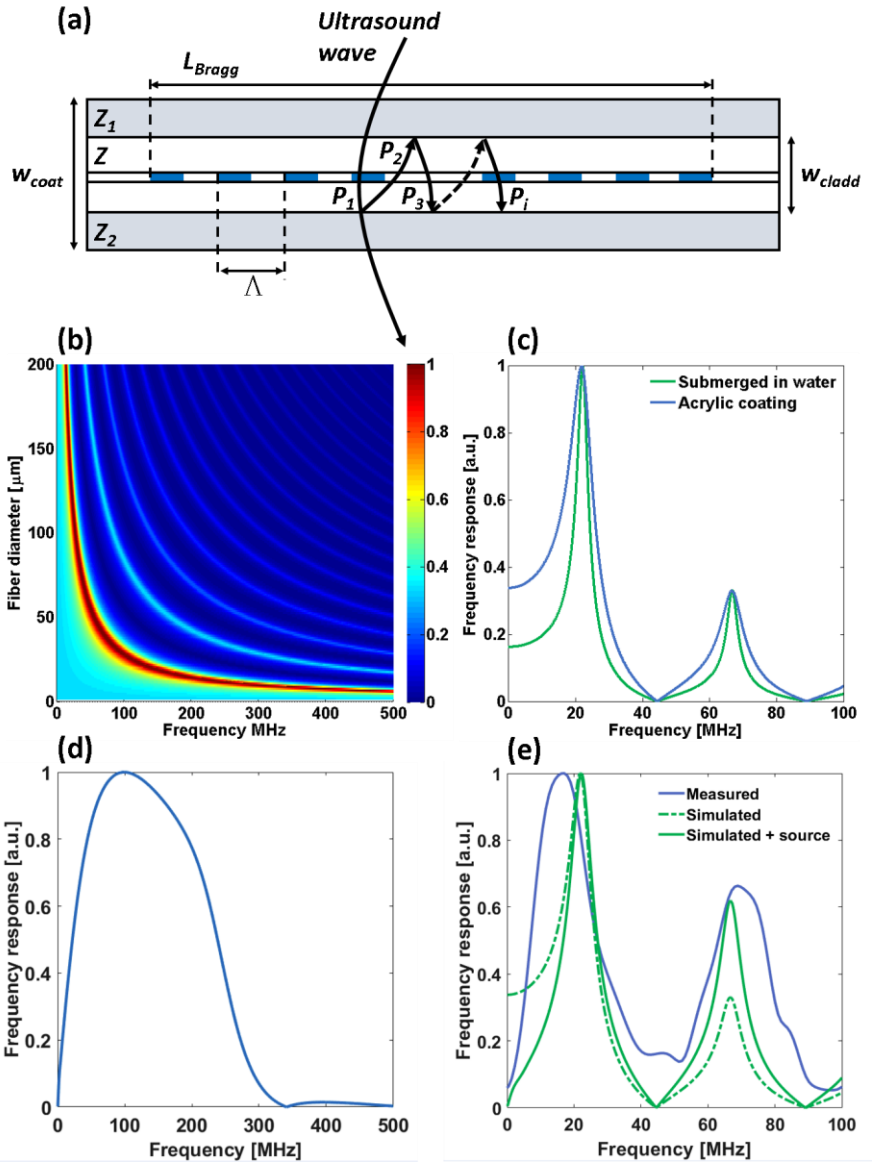

Figure 3.20 Frequency response of π-FBG sensor written in the SMF28 single-mode fiber. **(a)** schematic of the fiber and the ultrasonic wave impeding on it. Z = 14.5 MRayl, acoustic impedance of the silica fiber core and cladding; $Z_1 = Z_2 = 3.15$ MRayl, acoustic impedances of the front and back acrylic coatings of the fiber; $P_1 \ldots P_i$, ultrasonic reflections from the coating-cladding interfaces of the fiber; $W_{cladd} = 125$ μm; cladding diameter of the fiber; $W_{coat} = 250$ μm, coating diameter of the fiber; $L_B = 2$ mm, length of the Bragg grating in the fiber; Λ, period of the Bragg grating. **(b)** simulation of the spectral response of the fiber versus W_{cladd}. **(c)** Spectral response of the fiber with acrylic coating versus spectral response with no coating and being submerged in water for acoustic impedance matching. **(d)** Theoretical spectral content of an ultrasonic signal emitted via the optoacoustic effect from a 10 μm polystyrene microsphere. **(e)** Comparison of the simulated spectral response of the fiber with the same spectral response overlaid with the spectral content of the source from (d), and the measured spectral response.

3.4.5 Discussion and conclusions

This chapter starts by surveying the properties of Bragg gratings in different platforms. Specifically, we concentrate on the commercially available fiber Bragg gratings (FBG) and waveguide Bragg gratings realized in the silicon-on-insulator (SOI, also known as 'silicon photonics') platform. We show that the bandwidth (the FWHM of the band-gap) of the gratings is directly proportional to the product of κL_B where κ is the coupling coefficient of the grating which can also be interpreted as the amount of reflection per unit, and L_B is the length of the grating. κ is directly proportional to the refractive index contrast between two succeeding sections of the grating. In the fiber this contrast is achieved by exposing it to periodic patterns of UV light, in the SOI platform the width of the silicon waveguide along the optical axis is changed by adding corrugation to the size walls of the waveguide.

We also surveyed the properties of π-shifted Bragg grating etalons, which are composed of two identical Bragg gratings with a spacing between them. The gratings act as the mirrors of the etalon and the spacing is the optical cavity. Such devices are interesting for sensing applications as the optical field build-up in the cavity section greatly enhances the sensitivity. For strongest localization of the optical field the cavity should be as small as possible. The shortest possible cavity length that still fulfils the requirement of constructive interference is equivalent to half of the wavelength, or an acquired round-trip phase shift of π. The spectrum of a π-shifted Bragg grating consists of a band-gap and a resonance in the middle. The bandwidth of the resonance (the FWHM of the resonance) is inversely proportional to κL_B, and the Q-factor of the etalon is directly proportional to κL_B, because stronger gratings increase the reflectivity of the etalon's mirrors and improve the light confinement. The Q-factor is also limited by the optical propagation losses in each platform.

π-shifted Bragg gratings in the SOI platform, or π-shifted waveguide Bragg gratings (π-WBG), are very sensitive to process non-uniformities and variations in the thickness of the silicon wafer. Therefore the optical parameters (resonance wavelength, Q-factor, etc.) of the π-WBG can greatly deviate from the designed parameters. In order to characterize the process, we designed 16 π-WBG on a single silicon chip with wide spread of design parameters (waveguide cross-section corrugation depth, grating period, cavity length). Such devices were reported before in the literature but no detailed study was done on the effect of the non-uniformities on their ultrasound sensing

performance [52], [79] In addition, the previously reported devices failed to detect longitudinal ultrasound waves [52] because the top oxide cladding of the π-WBG blocked ultrasound from reaching the sensor due to the high acoustic impedance mismatch between the cladding and water. In order to be able to test the effect of optical parameters of the π-WBG on the acoustic performance (in terms of bandwidth, sensor size, sensitivity) we used a polymer I-line resist as the top cladding. The small acoustic impedance mismatch between the resist and water does not block ultrasound from reaching the sensor. We experimentally demonstrated that deeper corrugations of the grating induce redshift of the resonance wavelength and increase the Q-factor and the band-gap width of the π-WBG. This is the result of the increase in the refractive index contrast between the corrugated and un-corrugated sections, and a consequence increase in κ and the grating strength. For a π-WBG with a rectangular cross-section (**'Strip waveguide'; Fig. 3.1**) 10 nm increase in the corrugation depth was demonstrated to increase the resonance wavelength by ~5 nm, the Q-factor by ~ 0.5× 10^4, and the band-gap width by ~0.5 nm. For a π-WBG with a rib cross-section (**'Rib waveguide'; Fig. 3.1**) those values would be ~1 nm, ~0.05× 10^4, and ~0.1 nm respectively. Inter-chip variation for the strip π-WBG for a given corrugation depth resulted in resonance wavelength fluctuations of up to ~5 nm, Q-factor fluctuations of up to ~ 0.5 × 10^4, and band-gap fluctuations of up to ~0.7 nm. For the rib π-WBG those numbers are ~5 nm, ~ 0.1 × 10^4, and ~0.5 nm. Two important conclusions can be drawn from this data:

1. For both designs the inter-chip variations of the optical parameters can be as large as a change in those parameters as a results of a 10 nm increase in the corrugation depth.
2. A change of 10 nm in the corrugation depth effects the optical parameters of the rib waveguide more weakly than the optical parameters of the strip waveguide. Rib waveguides are also effected by process non-uniformities to a lesser extent.

The reason for the differences between the two waveguides lies in the stronger TE mode confinement in the rib waveguide (**Fig. 3.2a** vs **Fig. 3.3**), which makes the rib design more resilient to changes in the dimensions of the cross-section. For the same reason it is harder to achieve strong Bragg gratings with the rib waveguide. The strongest Q-factor of the π-WBG achieved in the rib design with corrugation of Δw = 160 nm was of the same magnitude as the weakest Q-factor achieved for the strip design with corrugation of Δw = 25 nm. The highest Q-factor measured was for a strip π-WBG with Δw = 40 nm and a cross-section of 220 × 500 nm^2, therefore this device was selected for acoustic characterization.

We continued by exploring the relation between the optical parameters of the π-shifted Bragg gratings and their ultrasound sensing performance. We showed that the sensitivity to ultrasound is a product of the optical phase sensitivity and the acoustic phase sensitivity. The first term is the slope of the resonance, therefore directly proportional to κL_B. The second term depends on the materials composing the sensor and its spatial orientation relative to the ultrasound source. For high sensitivity stronger Bragg gratings and materials with high photo-elastic coefficients and low Young modulus are desirable.

The sensor size determines the detection bandwidth and the image resolution, therefore small sensors are desirable. We demonstrate theoretically that the sensor size is determined by the optical field confinement around the cavity section of the π-shifted Bragg grating. This confinement (FWHM of the spatial distribution of the optical field along the optical axis of the waveguide), or the sensing length L_S, is inversely proportional to κ. Commercial π-FBGs have κ that is 11 –fold smaller than the κ of the π-WBG developed in this work, which indicates that π-WBG would have 11 –fold smaller sensing lengths. While experimental results show that L_S of the π-WBG is only 4.5 –fold smaller they also demonstrate that the SOI platform can be used for ultrasound detection and it is a promising solution for miniaturization of ultrasound sensors. The bandwidth of the π-FBG sensor has two distinct lobes, with peak sensitivity around 17 MHz. Those results are in a good agreement with a theoretical model we developed for predicting the frequency response of π-FBG sensors. The model demonstrated that the bandwidth is strongly determined by the diameter of the fiber and the acoustic impedances of the fiber and fiber coatings. The frequency response of the π-WBG sensor was demonstrated to be larger than 50 MHz [52]. The wider bandwidth is a direct result of the sensor miniaturization.

4. The silicon waveguide etalon detector: an ultrasound point sensor

In this chapter we describe the development of a new SOI sensor with sub-micron aperture. We characterize the acoustic performance of the sensors in terms of sensitivity, bandwidth, and sensor size and compare its performance to that of the π-FBG and π-WBG sensors. We perform raster-scan optoacoustic mesoscopy with the novel sensor and characterize the resolution achieved with the sensor.

4.1 Motivation

In **Section 3.2** we described how optical resonator-based sensors could be miniaturized without loss of sensitivity, and how the miniaturization often results in larger detection bandwidth that could offer improvements in imaging resolution. **Table 4.1** summarized few prominent examples found in the literature, of optical resonator-based sensors realized in the polymer, silica, and SOI platforms. For most of those examples the resolution was not reported, but we can calculate the best case theoretical resolution from **Eq. 2.1.23-24.** From examination of **Table 4.1** several interesting observations can be made:

1. Finite aperture blurs the image laterally.
2. Improvements in bandwidth alone cannot be exploited to improve the resolution.

Point (2) is especially evident in the case of the polymer MRR. Instead of isometric resolution of ~4 μm the lateral resolution is 12 –fold worse than the axial due to inability to further miniaturize the polymer MRR.

	Platform	BW [MHz]	R_A [μm]	ϕ_d [μm]	R_L [μm]	References
SU-8 MRR	Polymer	280	4	60	60	[24]
PMMA Fabry-Perot	Polymer	22	55	22	60	[28]
π-FBG	silica	20	60	280	286	[48]
OMUS	SOI	1	1200	30	1200	[53]
π-WBG	SOI	40	30	100	104	[52] and **Section 3.4.4**

Table 4.1 Characteristics of various optical resonator-based sensors of ultrasound and their corresponding theoretical axial (R_A) and lateral (R_L) resolutions.

In **Section 3.2** we described how additional miniaturization of the sensors is possible when the high index contrast SOI platform is used. Previous attempts like the OMUS (**Table 4.1**) resulted in modest reduction in size of 2 –fold, but a membrane-based design resulted in poor detection bandwidth and a sensor not usable for optoacoustic imaging. The π-WBG (**Table 4.1**) achieved a bandwidth that allows it to compete with focused piezoelectric transducers [3] but the size of its aperture was larger even compared to the sensors constructed in the low index polymer platform, which results in large deterioration of the lateral resolution.

The reason of failure to reach adequate miniaturization can be explained by comparison of **Fig. 3.18** and **Fig. 4.1**. **Fig. 3.18** depicts the spatial distribution of the optical field around the phase shifted section of the π-FBG and π-WBG sensors from **Table 4.1**. When the phase shifted Bragg grating resonator design was copied from the silica to SOI platform the resulting reduction in the sensor aperture along the optical axis was only ~11 –fold (calculated by taking the FWHM of the optical field, similar to [48]). In this design the sensor aperture along the optical axis is inversely proportional to the coupling coefficient, the ratio between the coupling coefficients of the Bragg gratings would determine the achievable reduction when moving the design from platform to platform. In the SOI platform the Bragg grating are constructed by applying corrugation to the silicon waveguide (**Section 3.3.4**). The coupling coefficient of the grating is determined by the contrast in the effective refractive index of the corrugated and uncorrugated sections (**Eq. 3.4.5**). While the SOI platform is considered high index contrast platform with $\Delta n \approx 2.5$ between the silicon core and the silica cladding the optical reflectance of such an interface is only ~24 % (calculated form Fresnel equations for normal incidence). Moreover, the index contrast between

the corrugated and uncorrugated sections of the π-WBG sensor from **Table 4.1** is only $\Delta n \approx 0.022$ which results in ever lower reflectance and weak confinement of the optical field around the phase shifted section.

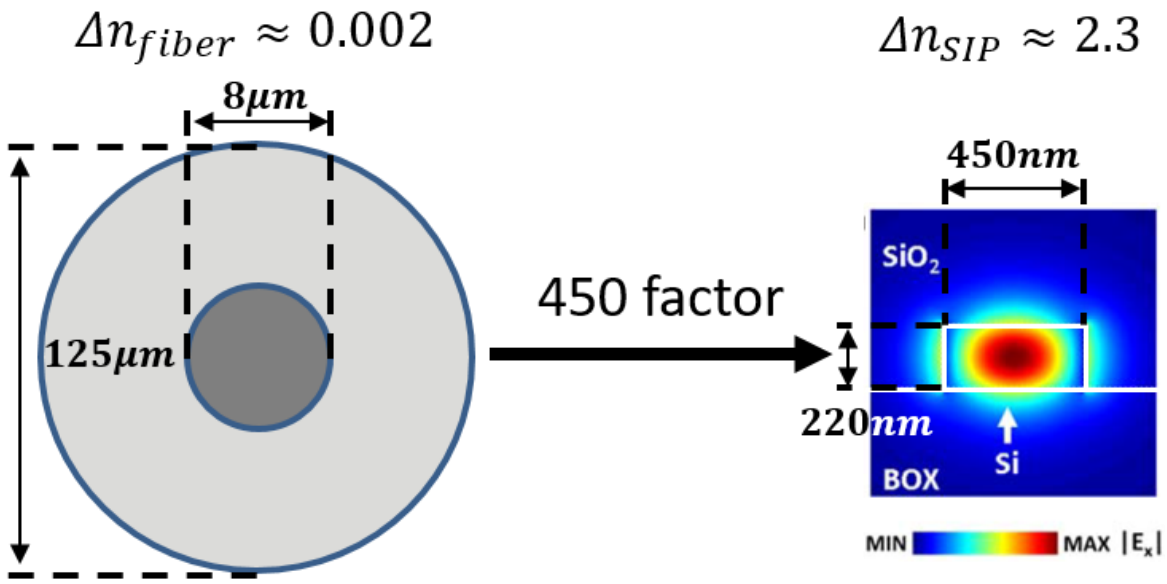

Figure 4.1 Schematic of a cross-sections of a single mode optical fiber and a rectangular silicon waveguide in the SOI platform. A mode solver [61] was used to simulate the TE mode of the silicon waveguide. The normalized profile of the horizontal component of the electric field (E_x) over an area of 1 × 1 μm is depicted. The white lines indicate the boundaries of the waveguide.

On the contrary, when the optical confinement along the cross-sections of single-mode waveguides in the silica and SOI platform is examined (**Fig. 4.1**), the index contrast of the SOI results in dramatic miniaturization of ~450 –fold. The conclusion is clear, in order to take full advantage of the high index contrast of the SOI platform the traditional resonator designs (MRR, phase shifted Bragg gratings, etc.) cannot be simply copied to the SOI platform from other platforms. The resonator design has to be adjusted in order for the ultrasound sensing to occur through the cross-section of a waveguide and not perpendicular to the optical axis as was done before [52], [53].

4.2 Design

In this work, we circumvent the flaws of the previous silicon-photonics sensor designs and take full advantage of the large index contrast by utilizing the sub-micron cross-section of a silicon

waveguide as the aperture for ultrasound detection. The subwavelength light confinement in the cross-section (**Fig. 4.1**) is at least 60-fold finer than was previously achieved by Bragg gratings [52] or ring configurations [53], in which the light confinement along the waveguide is utilized as the aperture for ultrasound detection. Our design shows no loss of sensitivity to longitudinal ultrasonic waves (L-waves). The low photo-elastic coefficients and the large Young modulus of silicon (as described in **Section 3.2**) are mitigated by directly exposing the optical mode to ultrasound without inducing additional optical losses. This results in a transduction mechanism that is 3 orders of magnitude more efficient compared to polymer MRRs [97].

Fig. 4.2 depicts the schematic of our sensor termed the silicon waveguide etalon detector (SWED). The sensor (**Fig. 4.2a**) is based on a single continuous silicon waveguide with cross-section of 220 × 500 nm^2 fabricated on an SOI chip with SiO_2 top cladding. The sensor consists of four sections: Thin metallic coating, spacer, cavity and Bragg grating. A ~200 nm thick metallic reflective layer (**'MC'; Fig. 4.2a**) was deposited onto the polished end facet of the waveguide, followed by a spacer section consisting of an ultra-short Bragg grating with a varying length of ~3 µm to ~25 µm (**'L_s'; Fig. 4.2a**). The reflective layer together with the spacer act as the first optical mirror of the etalon. By employing an ultrathin metallic layer and short L_s we were able to place the optical cavity in close proximity to the end facet of the waveguide, allowing ultrasound detection through its cross-section. The thinness of this mirror ensures that more of the confined optical field in the cavity is exposed to ultrasound [97]. A waveguide segment 320 nm long lies adjacent to the spacer, forming the etalon cavity (**'L_π'; Fig. 4.2a**). The other end of the cavity is terminated by a second optical mirror made of a second 125 µm-long Bragg grating (**'L_B'; Fig. 4.2a)**. The cavity's length was designed such that the acquired optical round-trip phase shift is π at the resonance wavelength of the etalon. The Bragg gratings were constructed by adding lateral corrugation to the waveguide with a corrugation depth of Δw **(Fig. 1a,** *bottom right*), periodicity of 320 nm and duty cycle of 50%.

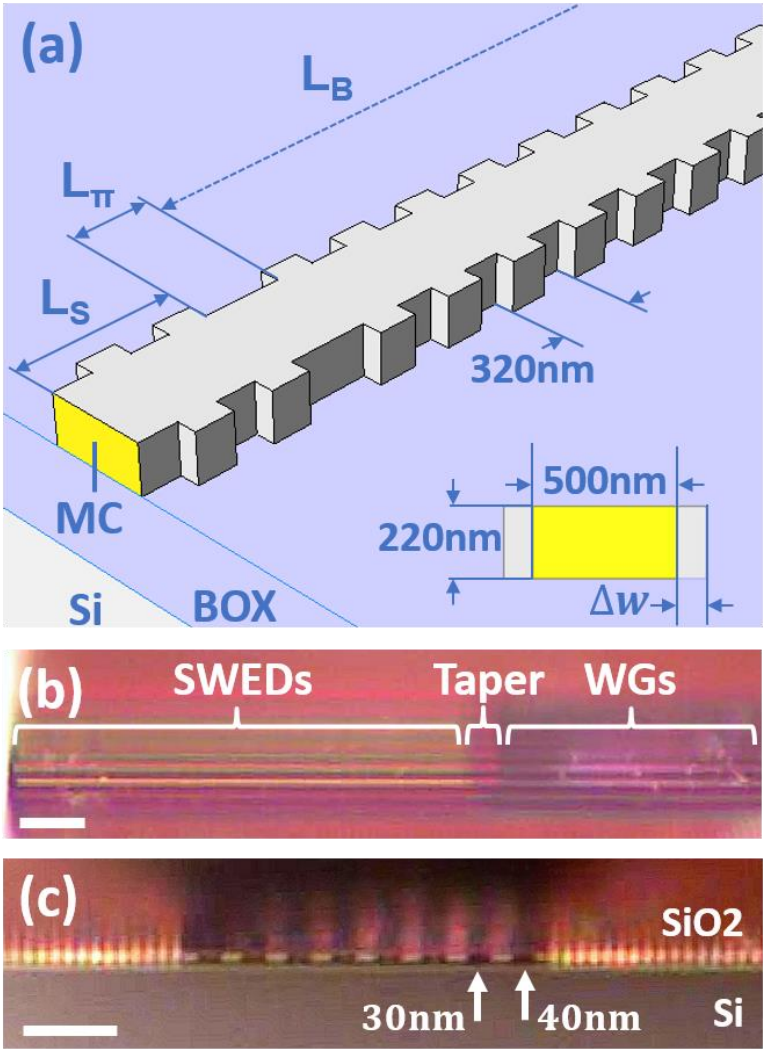

Figure 4.2 The silicon waveguide etalon detector (SWED). **(a)** Schematic of a single sensor. **(b)** brightfield micrograph of the SWED array on a chip taken perpendicularly to the optical axis. **(c)** brightfield micrograph of the SWED array on a chip taken in the direction of the optical axis before the application of the metallic coating.

In our design the reduced reflectivity of the spacer section is compensated by applying a ~200 nm silver layer on the chip facet (see **Section 6.2.2** for details), which equalizes the reflectivity of the spacer and Bragg sections and ensures large Q-factors. In addition, the silver-layer masks the optical mode (**Fig. 4.1**) from the surroundings and prevents optical losses. At the same time, the layer is sufficiently thin to prevent blocking of ultrasound waves or adding acoustic impedance mismatch. The excited TE mode (**Fig. 4.1**) is strongly confined to the cross-section of the silicon waveguide (Fig. 1c), ensuring ultrasound detection is limited to within this area.

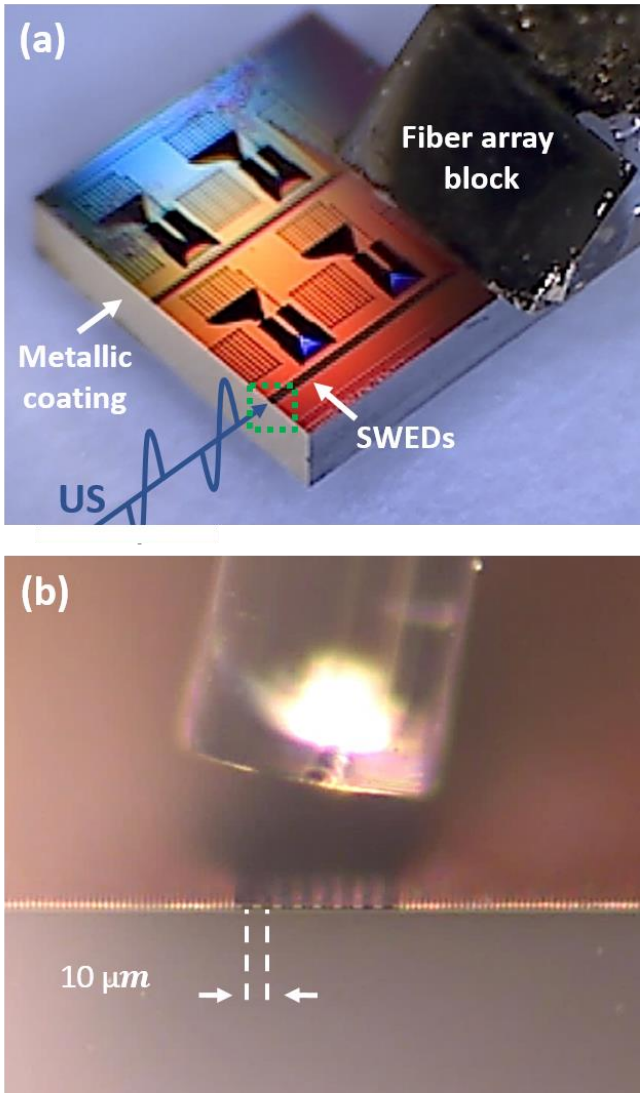

Figure 4.3 SWED sensor array on an SOI chip. **(a)** Photograph of the SOI chip facing the ultrasound source. US, ultrasound wave. **(b)** Micrograph of the area on the chip facet enclosed by the dashed green line in (b). On top a single mode fiber is visible for comparison.

In our implementation, we designed an array of eight SWEDs (see **Section 6.1** for details on the chip layout design), aligned next to each-other. A brightfield micrograph of the SWEDs on a chip taken perpendicularly to the optical axis of the SWEDs (**Fig. 4.2b**) depicts the eight SWEDs, each connected through a 15-μm adiabatic taper (**'Taper'**) to eight Si waveguides ('**WGs**') that are used to pump light into the SWEDs. A brightfield micrograph of the SWEDs taken in the direction of the optical axis of the SWEDs (**Fig. 4.2c**), obtained prior to the application of the silver coating, depicts the cross-section of the eight SWEDs, which differ in their corrugation depth Δw. **Fig. 4.2c** highlights two SWEDs that were the focus of this study, manufactured with Δw of 30 nm and 40 nm.

We manufactured four SOI chips (see **Sections 6.1** and **6.2** for chip layout design and sensor manufacturing) measuring $3 \times 3 \times 0.8$ mm^3 each (**Fig. 4.3a**), with spacer lengths of 26 µm, 14 µm, 9 µm, and 3.5 µm. Each chip comprises an array of eight SWEDs, aligned next to each-other with a pitch of 10 µm. **Fig.4.2b** shows enlargement of the area on the chip facet enclosed by the dashed green line in **Fig.4.2a**, the SWED array is clearly visible. The array is connectorized to a block containing an array of eight single-mode, polarisation-maintaining fibres ('**Fiber array block**') connecting each of the SWEDs to an interrogation setup. See **Section 2.3** for details on the interrogation of optical sensors in general, **Section 6.4** for details on the interrogation setup used in this work, and **Section 6.2.3** for sensor packaging. The fibers are oriented such as to excite the TE mode in the silicon waveguide. On each chip only the SWEDs with Δw of 40 nm were fully characterized as only those SWEDs were sufficiently sensitive to be used for imaging. The measured optical and acoustic properties of the SWEDs (see following sections for details), and their design parameters are summarized in **Table 4.2**.

			Optical Properties			Acoustic Properties	
	Spacer Length (µm)	**Δw (nm)**	**Resonance Wavelength (nm)**	**FWHM (pm)**	**Q-factor**	**f_c (MHz)**	**Bandwidth -3 dB / -6 dB (MHz)**
SWED1	26	40	1534.09	69	2.2×10^4	37	103 / 131
SWED2	14	40	1533.18	78	1.97×10^4	61	107 / 172
SWED3-40	9	40	1532.47	100	1.5×10^4	88	166 / 230
SWED3-30	9	30	1528.8	150	1.0×10^4	-	- / -
SWED4	3.5	40	1531.59	87	1.76×10^4	121	100 / 195

Table 4.2 Design parameters and measured optical and acoustic properties of the SWEDs.

4.3 Optical characterization

The SWEDs were designed with cavity length of only 320 nm resulting in a single, very narrow resonances at near-infrared wavelengths (**Fig. 4.4**), with FWHM in the range of 60-150 pm (**Table 4.2**). The resonances were recorded using the optical interrogation setup described in **Section 6.4**.

Fig. 4.4a shows the resonances of SWEDs with Δw of 40 nm and different spacer lengths. The SWEDs with shorter spacer length result in wider resonance and a lower Q-factor, this can be attributed to reduction in reflectivity of the spacer section when its length is reduced and the weaker confinement of light in the cavity. The resonances also experience a blueshift this can be explained by the tendency of the cavity to equalize the reflectivity of optical mirrors of the etalon. When the reflectivity of the spacer is reduced the resonance would shift to wavelengths on the edge of the stop-band of the Bragg grating, where the Bragg reflects less than at the Bragg wavelength (middle of the stop-band).

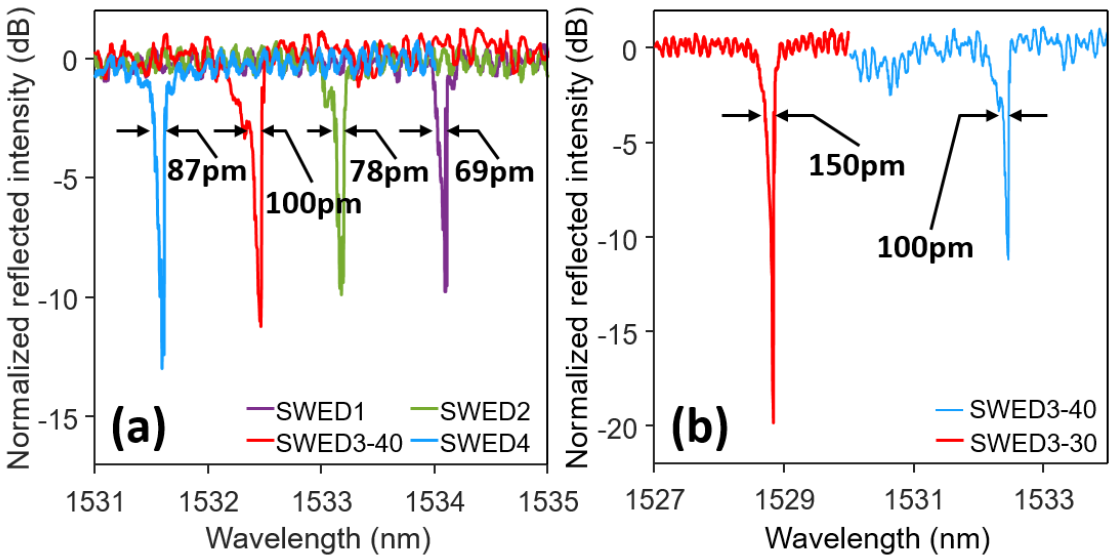

Figure 4.4 Optical resonances of various SWED sensors. **(a)** The resonance dependence on the spacer length. **(b)** the resonance dependence on the corrugation depth of the Bragg grating and the spacer.

We also serially interrogated adjacent SWEDs on the same chip. These measurements studied the effect of the corrugation depth. **Fig. 4.4b** shows the respective resonances for Δw of the 40 nm and 30 nm channels on the chip. We found that the deeper corrugation attained a higher Q-factor (**Table 4.2**) due to the increased reflectivity of the Bragg grating and the spacer sections. Comparison

between **Fig. 4.4a** and **Fig. 4.4b** reveals that changes in the corrugation depths affect Q-factor of the SWEDs much more strongly than changes in the spacer lengths. From this result we can conclude that the SWED sensitivity to ultrasound should have similar behavior.

4.4 Acoustic characterization

The SWEDs were installed in the acoustic characterization setup described in **Section 6.4** and were exposed to ultrasonic sources of micrometric size. The sources were generated through the optoacoustic effect by using a microscope objective to focus light into an absorber. By recording and analyzing the response of the SWEDs to those sources we were able to characterize the sensitivity, bandwidth, and the directivity of the SWEDs. Those are key parameters that determine image quality and resolution. The results are summarized in **Table 4.2.**

Sensor size and directivity

We selected SWED3-40 to characterize the spatial response of the detector. Using the acoustic characterization setup in **Section 6.4**, we scanned the detector along a 4 mm distance (10 µm step size) over a broadband acoustic point source. The orientation of the chip relative to the source is depicted in **Fig. 4.5a.** For each translation step the detected ultrasonic pulses were recorded as a function of time (B-scan). **Fig. 4.5b** and **Fig. 4.5c** depict the spatial response of the SWED along the *x*- and *y*-axes respectively. Both responses show curved profiles with signal velocity of ~1526 m/s, indicating direct propagation of longitudinal waves in water from the source to the aperture of the SWED (**'L-waves'**; **Fig. 4.5b** and **Fig. 4.5c**). We also observed surface acoustic waves propagating at much higher velocities (**'SAW'**; **Fig. 4.5b** and **Fig. 4.5c**). SAW are excited when L-waves are incident on the silicon-water interface at Rayleigh critical angles [52]. **Fig. 4.5b** shows that SAW are excited symmetrically around the SWED while **Fig. 4.5c** shows excitation only from one side, which is attributed to the location of the SWED on top of the SOI chip. Acoustic reflections between the chip and the cover slip are also visible in the spatial responses (**'REF'**; **Fig. 4.5b** and **Fig. 4.5c**).

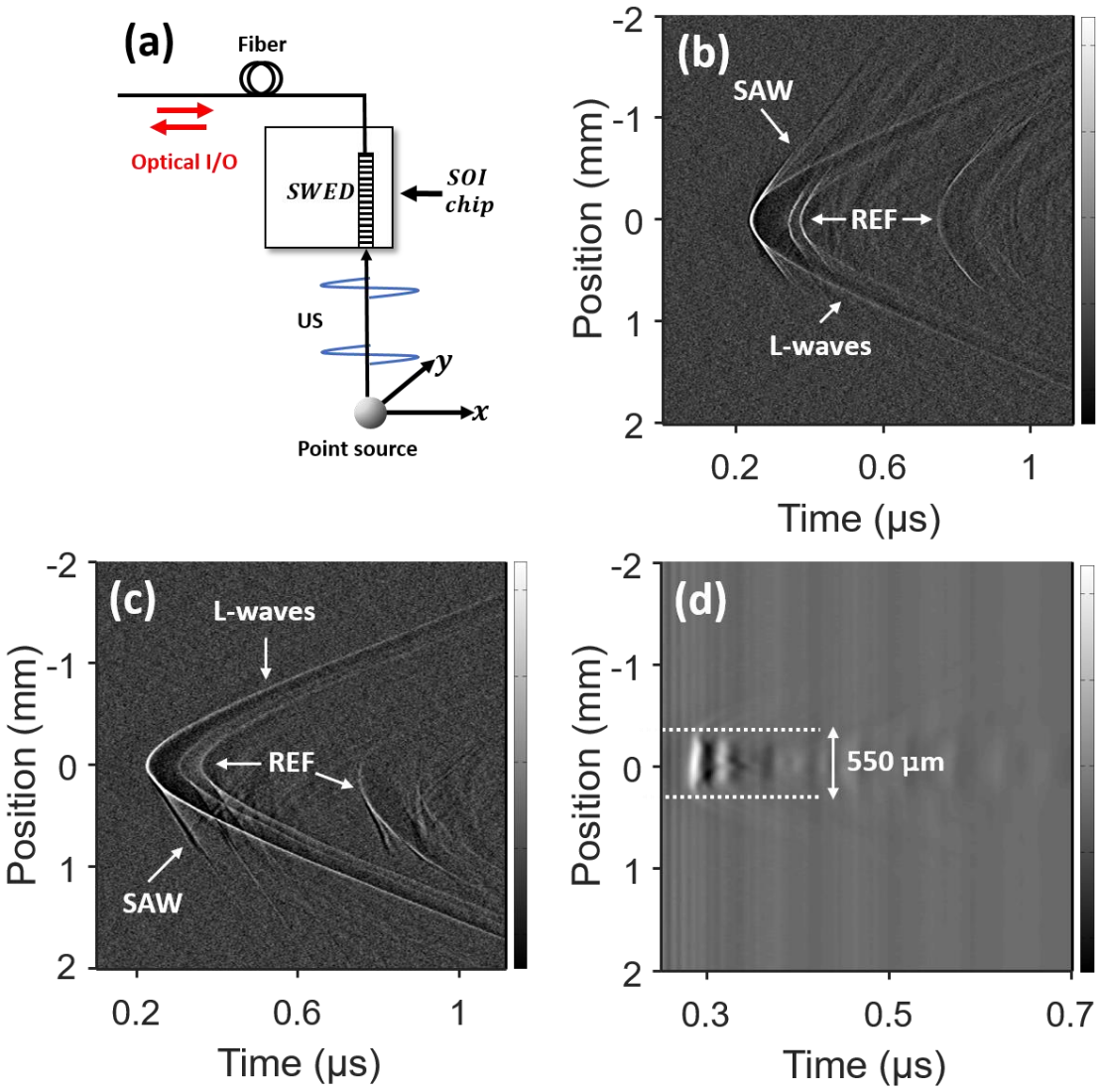

Figure 4.5 Directivity characterization of the SWED and a 0.5 mm needle hydrophone. **(a)** schematic of the SWED sensor relative to the ultrasound point source. **(b)** and **(c)** B-scans of the SWED sensor over the point source along the *x* and *y* axes respectively. SAW, surface acoustic waves; L-waves, longitudinal waves; REF, reflections. **(d)** B-scans of the needle hydrophone sensor the point source.

Comparison of the spatial responses of the SWED (**Fig. 4.5b** and **Fig. 4.5c**), the π-WBG sensor (**Fig. 3.19a**), and the π-FBG sensor (**Fig. 3.19b**) reveals no smearing of the point source by the SWED in any or the scanning directions, indicating that the SWED is sufficiently wideband to detect the high frequencies emitted from the point source and its aperture is on the size of the point source or smaller. For comparison purposes we also scanned a needle hydrophone of 0.5 mm diameter over an ultrasound point source. The spatial response of the hydrophone (**Fig. 2e**) shows

that common finite-size detectors are dominated by their aperture and the point source is smeared to a width comparable with the hydrophone aperture.

The acceptance angle of the SWED for L-waves was calculated from profile "**L-waves**" (**Fig. 4.5b**) by determining the maximum angle whereby signals with intensity of at least -6 dB of the most intense signal in **Fig. 4.5b** could be detected. We found an acceptance angle of 148°, corresponding to an acoustic numerical aperture (NA) of 0.96. This value is close to the NA = 1 of a theoretical point detector.

Frequency response and Bandwidth

The frequency response of SWED3-40 to the SAW and L-waves can be extracted from the B-scans (**Fig. 4.5c**). **Fig. 4.6a** depicts the detected ultrasonic signals at coordinates (0,0) and (0,0.3), the different shapes of L-wave and SAW are clearly visible. In addition, the L-wave at (0,0.3) is stronger by 4-fold than the L-wave at (0,0) as a result of the Rayleigh dip – a drop in the reflection coefficient of L-waves around the critical angle [98].

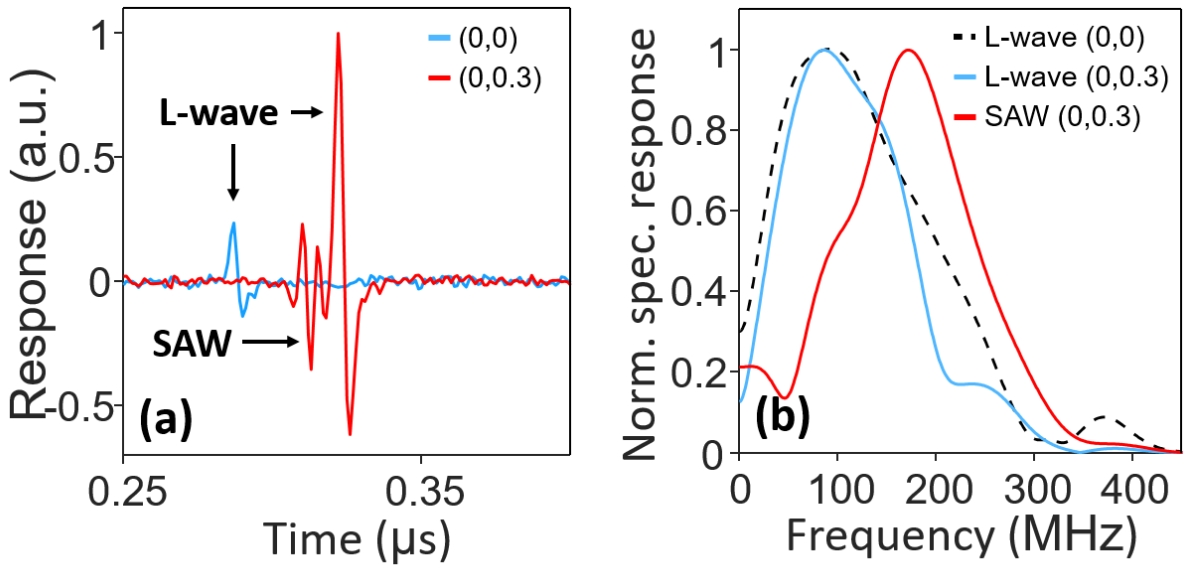

Figure 4.6 Temporal and spectral response of the SWED to an ultrasound point source at different spatial orientations. **(a)** Temporal responses of the SWED at coordinates (0,0) and (0,0.3) in **Fig. 4.5c**. L-wave, longitudinal ultrasonic waves; SAW, surface acoustic waves. **(b)** Acoustic spectrum of the signals in (a). L-waves arriving directly to the SWED at coordinates (0,0) and (0,0.3) – black-dashed and blue curves respectively, and the SAW generated at the water-silicon interface at coordinates (0,0.3) – red curve.

The spectral contents of the L-waves and the SAW (**Fig. 4.6b**), calculated by taking the Fourier transform of the signals in **Fig. 4.6a**, indicate that the SWED has a detection bandwidth of 230 MHz at -6 dB around 90 MHz for the L-waves, and a detection bandwidth of 190 MHz at -6 dB around 172 MHz for the SAW.

The results presented in **Fig. 4.6b** indicate that the SWED response to L-waves and SAW is different. Detection of L-waves predominantly occurs in response to a change in the cavity length. On the other hand, the SAW propagates at the surface and interacts with the resonator superficially, potentially through the photo-elastic effect [65]. The difference in the light confinements along the cross-section and the waveguide is responsible for the higher frequency response to SAW.

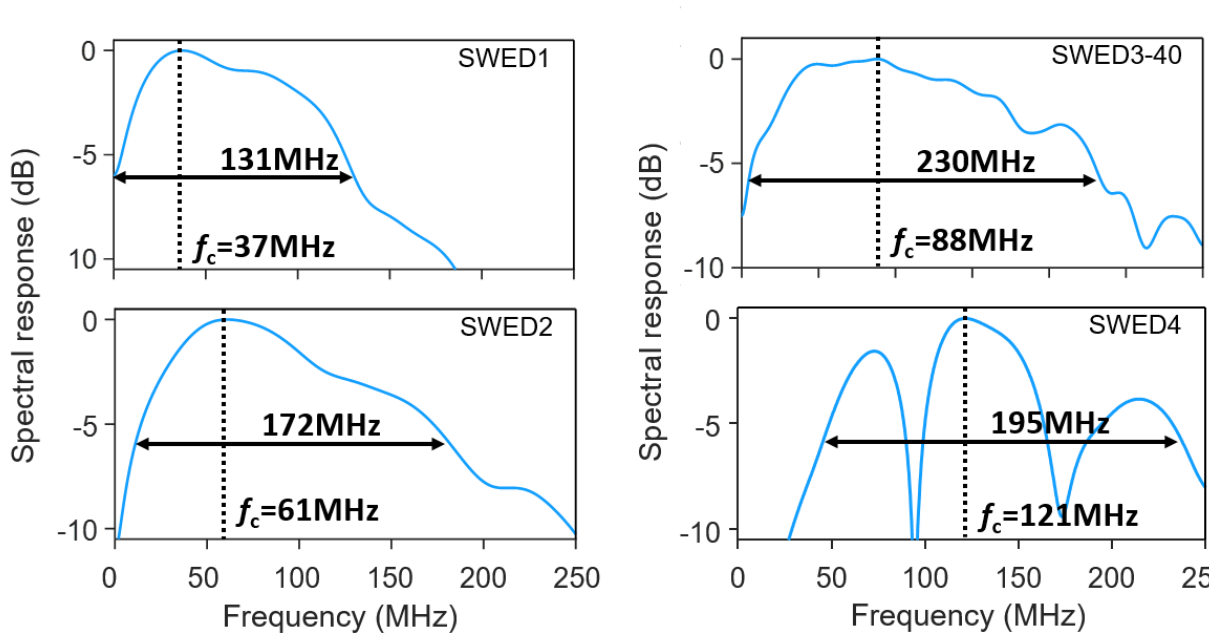

Figure 4.7 Detection bandwidth of SWEDs with Δ*w* of 40 nm and different spacer lengths.

The spectral response of the other SWEDs to L-waves at coordinate (0,0) was acquired in a similar method using the same ultrasound point source. **Fig. 4.7** shows the detection bandwidth of SWEDs with Δ*w* of 40 nm and different spacer lengths (**Table 4.2**). The SWEDs with shorter spacer tend to have a higher frequency response, this is attributed to the enhanced detection of shorter wavelengths when the optical cavity, which is the most sensitive section of the SWED, is located closer to the polished facet of the chip. **Fig. 4.7** also demonstrates that by changing the spacer

length it is possible to tune the central detection frequency (f_c) and shift the detection bandwidth by more than 80 MHz.

Sensitivity

The SWED with spacer length of 26 µm (SWED1) has a bandwidth that most closely overlaps with the calibrated bandwidth of a 0.5 mm needle hydrophone, and was therefore selected for sensitivity characterization. In order to determine the noise equivalent pressure (NEP), SWED1 and the needle hydrophone were exposed to the same ultrasonic source using the acoustic characterization setup in **Section 6.4**. The recorded signals without averaging are depicted in **Fig. 4.8**, the hydrophone signal was scaled by a factor of 30 for better representation. The spectral response of the hydrophone is approximately constant in the frequency band of [5, 30] MHz and is equal to 450 mV/MPa. Using the hydrophone we found that the source was emitting 8.4 KPa in the frequency band of [5, 30] MHz. Dividing this value by the maximum of the pressure amplitude recorded by SWED1 in the [5, 30] MHz band we determined the sensitivity of SWED1 to be 80.7 mv/KPa.

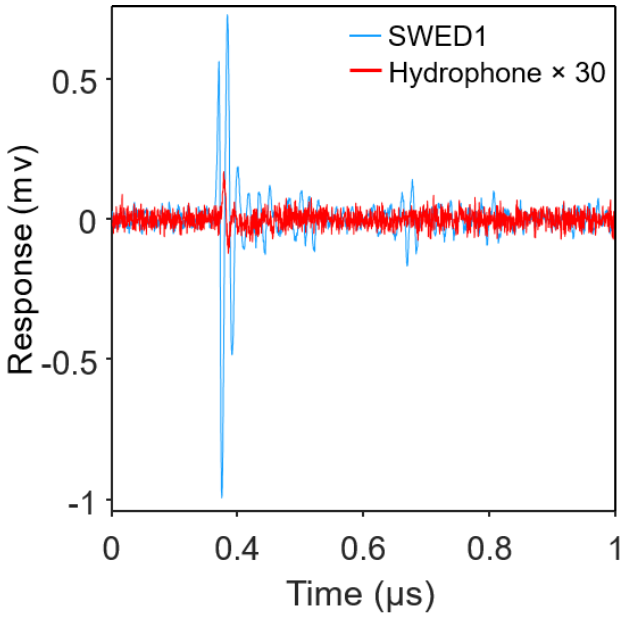

Figure 4.8 Hydrophone and SWED temporal response to an ultrasonic source over the frequency band of [2, 500] MHz. The signal recorded by the hydrophone was scaled by a factor of 30 for visibility.

The standard deviation of the noise in the [5, 30] MHz band was evaluated before the arrival of the ultrasonic signals (<0.3 µs) or long after (>2 µs), dividing it by the sensitivity we determined

$NEP_{[5,30]MHz}$= 94 Pa. Using the NEP extrapolation method described in **Appendix B** the NEP around the f_c = 37 MHz of SWED1 was determined to be $NEP_{[24.5,49.5]MHz}$ = 45 Pa (9 mPa/Hz$^{1/2}$) for detection bandwidth of 25MHz.

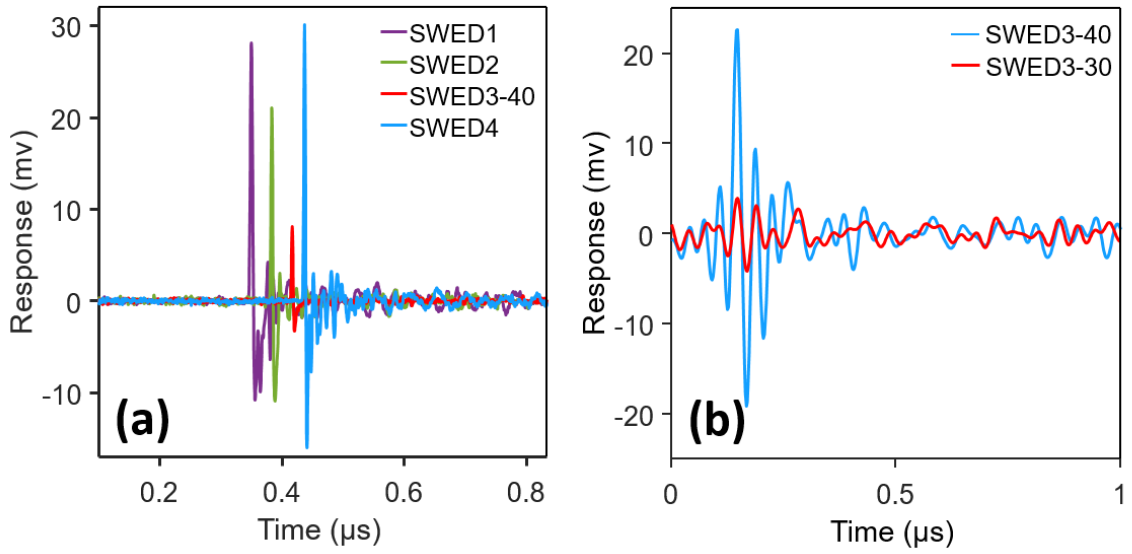

Figure 4.9 Temporal responses of SWEDs with different spacer length and corrugation depth to an ultrasonic source. **(a)** Responses of SWEDs with corrugation of 40 nm on different silicon chips with different spacer length to a broadband ultrasound source. The SWEDs were placed at the same distance from the source but each succeeding signal was shifted by 33ns for clear presentation. **(b)** Responses of two adjacent SWEDs on same silicon chip with spacer length of 9 µm and corrugation depths of 30 nm and 40 nm.

Since the bandwidths of the other SWEDs do not overlap with the calibrated bandwidth of the hydrophone, we deduced their sensitivity relative to SWED1. **Fig. 4.9a** shows the response of the SWEDs to a broadband ultrasound point source with approximately flat bandwidth. SWED2 and SWED4 exhibited similar sensitivity to SWED1 (Fig.2b). This indicates that the shift in f_c is possible without reducing the sensitivity of the SWED in each respective frequency band. SWED3 showed a 3.3-fold sensitivity drop due to a reduced Q-factor of the cavity (**Table 4.2**), likely due to inadequate metallic coating or inter-chip process nonuniformity [77].

Fig. 4.9b shows the response of two adjacent SWEDs with Δw of 40 nm and 30 nm manufactured on the same chip (**Table 4.2**) to an ultrasound point source. The deeper corrugation (SWED3-40) attained a higher Q-factor due to the increased reflectivity of the Bragg grating, resulting in a ~4 -fold improvement of the detected amplitude (**Fig. 4.9b**). A comparison between **Fig. 4.9a** and **Fig.**

4.9b reveals that changes in the corrugation depths affect the sensitivities of the SWEDs much more strongly than changes in the spacer lengths.

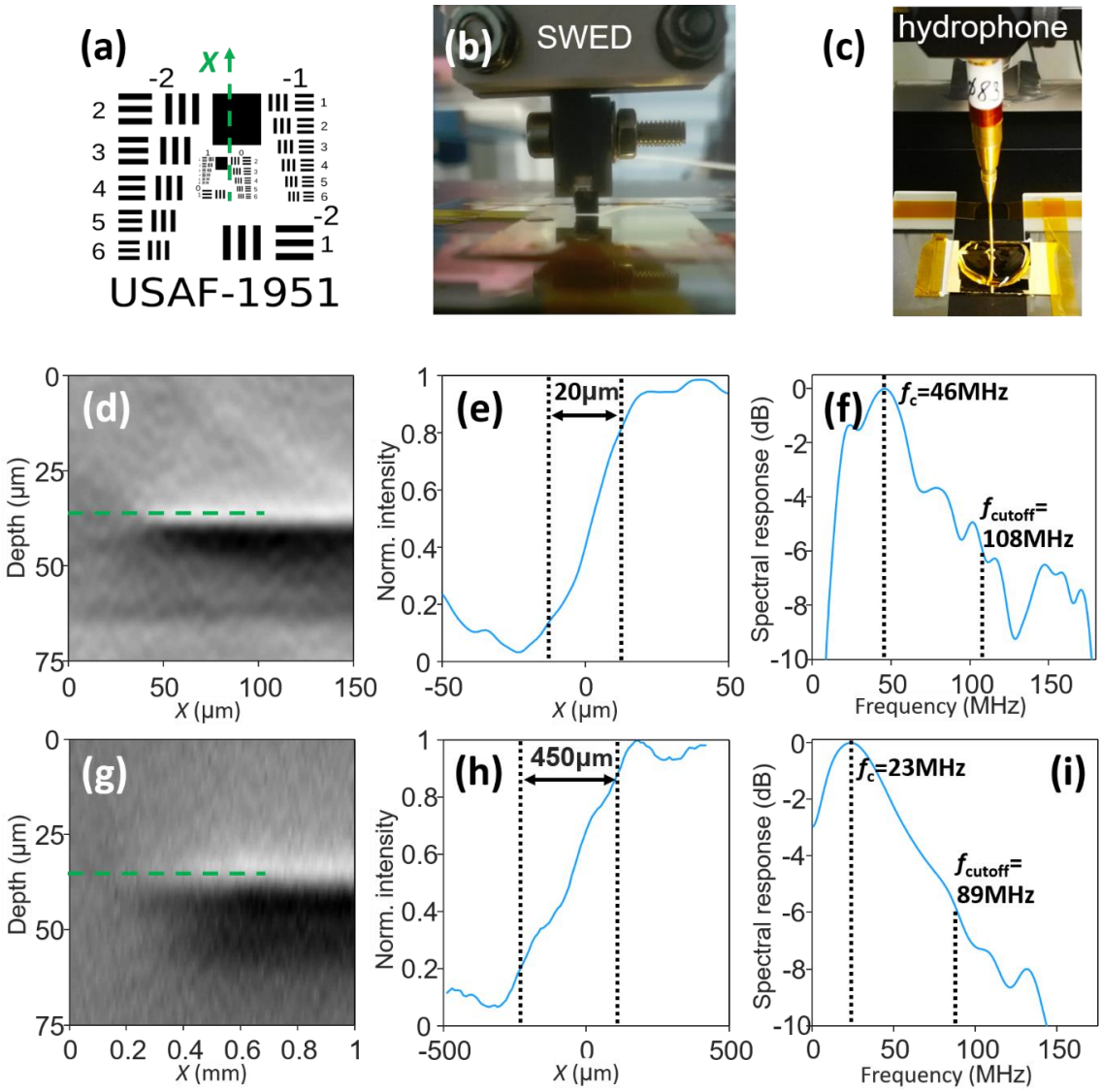

Figure 4.10 Edge spread function acquired by SWED and needle hydrophone. **(a)** Schematic of the test target sample. The scanning direction over the edge is indicated by the green dashed arrow. **(b)** Photograph of the chip **(b)** and the hydrophone **(c)** mounted over the sample. **(d)** Reconstructed B-scan of the SWED over a sharp edge on the sample. **(e)** Edge spread function (ESF) taken along the dashed line in (d). **(f)** Acoustic spectrum of the signals emitted from the target as measured by the SWED. **(d)** Reconstructed B-scan of the SWED over a sharp edge on the sample. **(e)** ESF taken along the dashed line in (d). **(f)** Acoustic spectrum of the signals emitted from the target as measured by the SWED.

4.4 Optoacoustic tomography with a point sensor

To evaluate the performance of the SWED for optoacoustic imaging we used SWED3-40 and the imaging setup described in **Section 6.5** to image resolution test target and several vasculature-mimicking phantoms.

First, we compared the lateral blurring induced by the aperture of the SWED to that induced by the aperture of a 0.5 mm needle hydrophone using the sharp edge of a 1951 USAF resolution test target (**Fig. 4.10a**). The SWED and the needle hydrophone were mounted a linear translation stages (**Fig. 4.10b-c**) and scanned over the edge with step sizes of 1 μm and 10 μm respectively. The detected signals were averaged 300 times and a [15, 350] MHz band-pass filter was applied to remove the low frequency noise generated by the direct exposure of the sensors to the laser. The images were reconstructed using a back-projection method in Fourier space [99]. **Fig. 4.10d** depicts the edge as imaged by the SWED. The edge spread function (**Fig. 4.10e**) measured along the dashed line in **Fig. 4.10d** reveals that the edge was blurred to ~20 μm. On the other hand, the edge imaged by the hydrophone (**Fig. 4.10g**) and the corresponding spread edge function (**Fig. 4.10g**) show blurring of ~450 μm, which is on the order of the hydrophone's aperture.

Next, we imaged a phantom constructed from two parallel carbon fibers with diameters of 6 – 8 μm and a 30 μm black polystyrene suture (Dafilon Polyamide, B. Braun Melsungen AG, Germany) placed diagonally across the fibers. The 3D rendering of the reconstructed 1.1×1.1 mm^2 field of view (10 μm step) is depicted in **Fig. 4.11a** and shows that the phantom is well resolved. The reconstructed lateral and axial profiles of the fiber and the suture along the dashed green line in (**Fig. 4.11a**), imaged with a finer step size of 1 μm are depicted in **Fig. 4.11c** and **Fig. 4.11d** respectively, the widths of those phantoms can be estimated from the FWHM of those profiles. We also imaged a layer of gold hexagonal mesh used to calibrate electron microscopes (G400HH, SPI Supplies; West Chester, USA) with bar width of 8 μm and sub-micron layer thickness. The 3D rendering of the reconstructed 0.4×0.4 mm^2 field of view (5 μm step size) is depicted in **Fig. 4.11b** and shows that the phantom is well resolved with no distortions to the mesh. The reconstructed lateral and axial profiles of a bar along the dashed green line in (**Fig. 4.11a**) are depicted in **Fig. 4.11e**, with the FWHMs indicated in the figure.

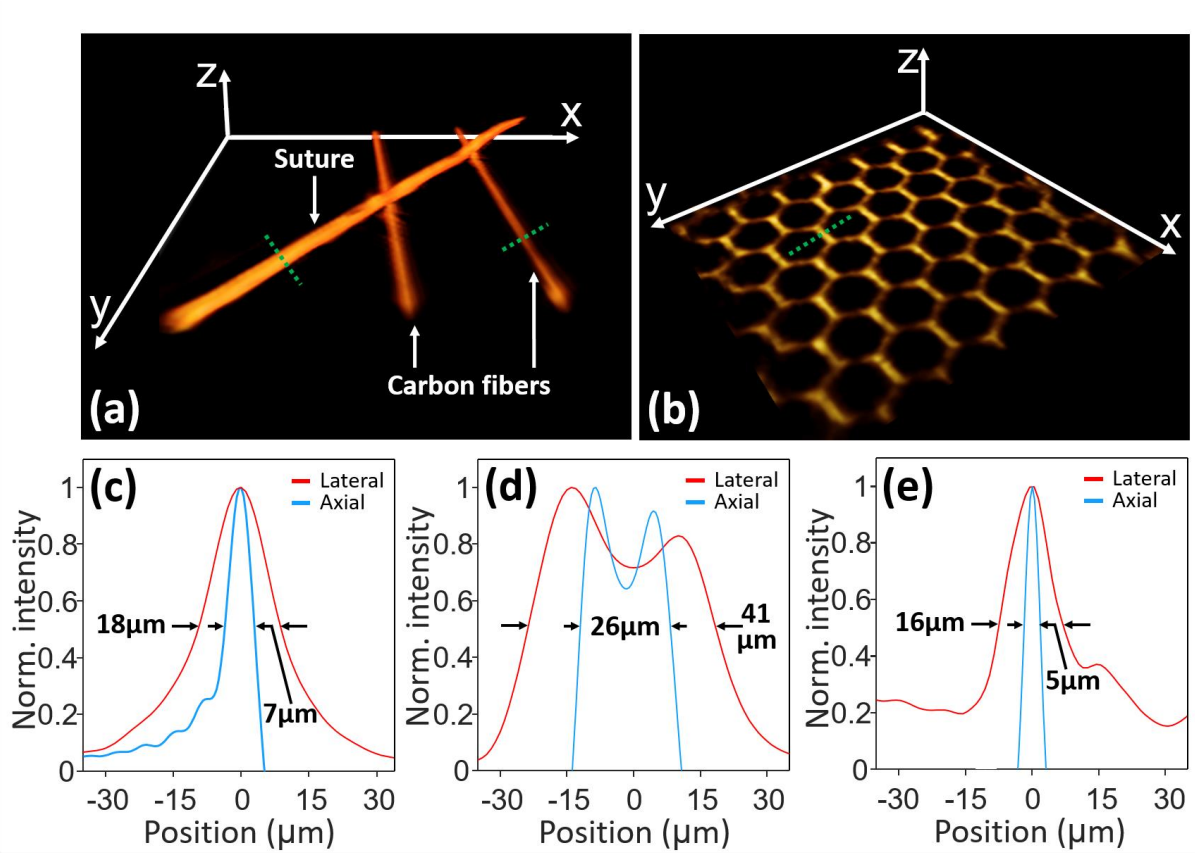

Figure 4.11 Optoacoustic tomography of vasculature-mimicking phantoms image with the SWED. **(a)** 3D rendering of a reconstructed 1.1 × 1.1 mm^2 field of view of a phantom composed of two parallel carbon fibers 6 – 8 µm in diameter, and a 30 µm polystyrene suture laying in diagonal imaged with step of 10 µm. **(b)** 3D rendering of a reconstructed 0.4 × 0.4 mm^2 field of view of a thin layer of gold hexagonal grating with bar width of 8 µm imaged with step size of 5 µm. **(c)** Reconstructed profile of a carbon fiber imaged with a step size of 1 µm along the green dashed line in (a). **(d)** Reconstructed profile of the suture imaged with a step size of 1 µm along the green dashed line in (a). **(e)** Reconstructed profile of a bar from the hexagonal grating images with a step size of 5 µm.

4.5 Discussion and conclusions

This chapter describes a novel ultrasound sensor termed the silicon waveguide etalon detector (SWED) that was developed and manufactured in the highly scalable silicon-photonics platform (silicon-on-insulator). The high refractive index contrast of this platform was exploited for ultra-miniaturization of the optical resonator-based sensor. With a sensing area at least 450 -fold smaller than that of a π-shifted waveguide Bragg grating (π-WBG) [52], nearly 2.6 x 10^4 smaller than that of polymer micro-rings [24], and 10 –fold smaller than human blood cell, the sensor is probably the smallest ultrasound sensor developed to this date. In this work, we circumvent the flaws of the

previous silicon-photonics sensor designs and take full advantage of the large index contrast by utilizing the sub-micron cross-section of a single-mode silicon waveguide as the aperture for ultrasound detection. The subwavelength light confinement in the cross-section is at least 60 -fold finer than was previously achieved by Bragg gratings [52] or ring configurations [53], in which the light confinement along the waveguide is utilized as the aperture for ultrasound detection.

The small size of the SWED aperture results in detection bandwidth as large as 230 MHz for longitudinal ultrasound waves. We demonstrated that by changing the spacer length of the SWED it is possible shift this bandwidth on demand by more than 80 MHz, moving the central frequency from 37 MHz to 121 MHz. When measuring surface acoustic waves we showed that the SWED can have even higher frequency response, reaching a bandwidth of 190 MHZ around central frequency of 172 MHz. The SWED aperture is approximately 200 –fold smaller than the acoustic wavelength at 37MHz and approximatly 60 –fold smaller than the acoustic wavelength at 121MHz, which satisfies the definition of a true point detector. The measured numerical aperture (NA) of 0.96 which is close to NA = 1 of a theoretical point sensor, confirms the point-like nature of the SWED.

We performed the first ever reported ultrasound-based imaging with a silicon-photonics sensor. The high bandwidth of the SWED improved image resolution and the sub-wavelength aperture was used to improve image quality by removing the lateral blurring associated with finite-size apertures [15], [17]. The expected theoretical blurring of the sharp edge on a 1951 USAF resolution test target when imaged by a point sensor with negligible aperture can be estimated by inserting the cutoff frequency ($\boldsymbol{f_{cutoff}}$) from the spectra emitted by the target and measured by the SWED (**Fig. 4.10f**) and the hydrophone (**Fig. 4,10i**), with $\boldsymbol{\phi_d} \approx 0$, into **Eq. 2.1.23**. The theoretical blurring expected for the SWED is ~11 µm, while the corresponding value for the hydrophone is ~14 µm. The latter value is smaller by a factor of ~30 compared to the experimental blurring measured for the hydrophone, indicating that when imaging with the hydrophone the aperture effect on the image quality cannot be neglected. In contrast, the experimental blurring recorded for the SWED was on the same order of magnitude as the theoretical value, indicating that imaging with the SWED is near diffraction-limited. When imaging the vasculature-mimicking phantoms a resolution of 16 µm laterally and 5 µm axially was achieved, this is respectively 2 – and 6 –fold better than what was achieved before with state-of-the-art sensors [3]. **Eq. 2.1.23-24** predicts isometric resolution for a point sensor, this was not achieved with the SWED and the sharp edge with the phantoms

experienced a small amount of lateral blurring. The lateral widths of the suture, carbon fiber, and the mesh are smeared by factors of ~1.4, ~2.3, and ~2, respectively. The deviation of the phantom widths from the specifications (**Fig. 4.10c-e**) can be attributed to the finite scanning range [15] and presence of surface acoustic waves during image reconstruction. Reconstruction is performed assuming all the signals propagate at the speed of longitudinal waves in water. Surface acoustic waves originating at the silicon-water interface propagate at higher velocities (**Fig. 4.5b-c**) and do not sum coherently during reconstruction, resulting in artefacts that can lead to blurring. In the axial directions, the phantoms in **Fig. 4.10a** experienced no blurring (**Fig. 4.10c-d**). This is because they are larger than the bandwidth dependent axial resolution of the SWED, which is estimated to be $\boldsymbol{R_A}$ ≈5 µm (**Eq. 2.1.24**). The sub-micron thickness of the mesh in **Fig. 4.10b** is blurred to 5 µm (**Fig. 4.10e**), which is the bandwidth dependent resolution limit of the SWED. The resolution could be further improved by characterizing the total impulse response of the sensor and deconvolving it from the images [100].

Previous silicon-photonics sensor designs experienced a sharp drop in sensitivity and were not able to detect longitudinal waves [52] because of the low photo-elastic coefficients and the large Young modulus of silicon and silica [65] (compared for example to polymer sensors [26]). Some designs mitigated the sensitivity issue by etching of a thin membrane under the sensor to improve sensitivity [53]. This resulted in a very narrow detection bandwidth (< 1 MHz), determined by the mechanical resonance of the membrane, that made sensors unusable for imaging. In **Section 3.4.4** we showed that it is possible to improve the sensitivity of a π-WBG sensor constructed on top of an SOI chip by changing the top oxide cladding to a polymer cladding made of I-line resist. The π-WBG sensor in the so called hybrid platform was able to detect ultrasound but with aperture of ~ 100 µm it is not attractive for high resolution imaging. In the SWED design we mitigated the sensitivity issue applying a thin metallic layer on the aperture, this resulted in direct exposure of the optical mode to ultrasound and exceptional gain in sensitivity without inducing additional optical losses. The product of the NEP and the sensing area allows an objective comparison of detectors with different underlying principle of operation. This figure of merit represents the efficiency of the transduction mechanism by normalizing the amplitude of the detected signal over the sensing area of the detector [23]. NEP×area has been reported to be 1.58×10^{-2} mPa×mm^2/Hz$^{1/2}$ (5.6 mPa/Hz$^{1/2}$) for polymer micro-rings employed in optoacoustic microscopy [25] and 509 mPa×mm^2/Hz$^{1/2}$ (450 mPa/Hz$^{1/2}$) for a miniaturized piezoelectric transducer for intravascular

ultrasound imaging [41]. Those values are, respectively, three and eight orders of magnitude lower than the sensitivity of 9.9×10^{-7} mPa×mm2/Hz$^{1/2}$ (9 mPa/Hz$^{1/2}$) achieved by the SWED. The NEP was demonstrated not to be strongly affected by the spacer length. On the other hand, a 10 nm reduction in the corrugation depth resulted in ~4 –fold drop in sensitivity. Smaller corrugation depth results in weaker Bragg gratings and lower Q-factors of the SWED which directly affect the sensitivity (**Eq. 3.4.16**). SWED sensitivity can be further improved by increasing the reflectivity of the Bragg grating (by increasing corrugation depth) and the reflectivity of the thin coating on the aperture of the SWED. The Q-factor can be further improved by reducing optical losses with reduction of the side-wall roughness [63] of the waveguide and exploring Rib waveguide geometries [66] which were demonstrated with lower propagation loss.

Combining many SWED elements into one array is technically feasible and could offer new sensing and imaging abilities leading to larger fields of view and faster imaging times than single element detectors. State-of-the-art piezoelectric arrays feature densities of 9.5 detectors/mm^2 [3], while arrays of capacitive micromachined ultrasound transducers have been reported with densities of 2.5 detectors/mm^2 [101]. Up-to-date arrays of polymer micro-rings were not demonstrated at all due to the poor light confinement of the polymer platform resulting in large device footprint and limited integration density. This drawback together with the luck of active functionality of polymers like emission and amplification make the platform unattractive for developing of arrays and their multiplexing. Using an array of 8 SWEDs, we preliminary managed to increase detection density by orders of magnitude, pointing to the possibility to achieve 125 detectors/mm^2. In fact, the technology showcased here could achieve densities of >1000 detectors/mm^2 since inter-SWED distances and Si wafer thickness can be further reduced with currently available manufacturing processes. In addition, 2D arrays are realizable by stacking chips on top of each other or using multilayer manufacturing processes[102].

5. Near-field scanning optoacoustic microscopy (NSOAM)

In this chapter we use the SWED sensor to perform λ/50 acoustic super-resolution optoacoustic imaging in the near-field.

5.1 Motivation

In **Section 4** we demonstrated how the sub-micron aperture of the SWED leads to improve image resolution in optoacoustic tomography. The best resolution that was achieved was 5 μm and it was limited by the bandwidth of the sensor. In order to take the full advantage of the sensor miniaturization and achieve resolutions on the order of the SWED aperture (220nm – 500 nm) the f_{cutoff} has to be larger than 2.4 GHz (**Eq. 2.1.14**). Even if it would have been possible to constructing such fast sensors the frequency dependent attenuation of ultrasound makes the possibility of imaging with such high frequencies unrealistic. The frequency dependent attenuation in tissue can be estimated as 0.5 $dB \times MHz^{-1} \times cm^{-1}$ [12], if attenuation of 10 dB can be considered as acceptable the imaging depth will be less than 80 μm.

For such shallow depths we can take advantage of the sub-wavelength aperture of the SWED to perform near-field super-resolution imaging, which would be the acoustic analogy of near-field scanning optical microscopy (NSOM) [103], [104]. The Near-field scanning optoacoustic microscopy (NSOAM), reported here for the first time, employs the SWED to sense the evenecent near-field of a sample excited by the optoacoustic effect. This is in contrast to NSOM, were the optical near-field of a probe is used to image the sample. As the acoustic wavelengths are much longer than optical, NSOAM imaging can be performed with the sensor in a distance of few to tens of microns from the sample, which does not require complex stabilization and feedback mechanisms of the like used in NSOM.

Previous implementations of near-field acoustic microcopy can be divided into few categories:

1. Piezoelectric transducers are bonded to sharp tips and are used to excite ultrasonic signals at the tip. The tip is brought very close to the sample (the distance depends on the tip size and the frequency used, typically < 1 μm) so the sample interacts with the acoustic near-field of the tip [105], [106]. Another transducer, acoustically matched to the sample, is used to collect the ultrasonic signals. The approach offers excellent resolution < 100 nm (determined by the tip size) but only elastic contrast mechanism. In addition, similar to NSOM feedback mechanisms are required to maintain the small distance between the tip and the sample.
2. Externally generated acoustic waves interact at the sample surface creating surface acoustic standing waves. Those waves carry information on the elastic properties of the surface and buried objects close to the surface (at sub-micron depth). A cantilever of an atomic force microscopes (AFM) is used to monitor local perturbations to the standing waves due to local variations in the elastic properties of the sample [107]. Similar to (2) the resolution is determined by the cantilever and the approach requires complex feedback mechanisms (for mechanic coupling between the cantilever and sample), but in contrast to (2) it also provides information on shallow buried nanostructures and not only on the sample's surface.
3. In another variant the ultrasonic waves are excited by the optoacoustic effect and detection is done by a probe made of a modified AFM cantilever with a plasmonic nano-focusing lens attached to it [108]. The lens concentrates light to a strongly localized focal spot at the tip of the prob. Image is formed by monitoring the scattering of the evanescent light at the probe tip due to vibrations at the surface of the sample, induced by ultrasound waves. This approach is based on the interaction of the optical near-field with the sample surface. Similar to NSOM it requires for the cantilever to be extremely close to the sample.

The major difference between the above approaches to NSOAM is that NSOAM uses the acoustic near-field of the sample to image the object. This near-field extends farther compared to the optical or acoustic near-fields emitted from the probe, relaxing the distance between the probe and the sample, and providing optical absorption contrast. NSOAM does not require image reconstruction as the diffracted ultrasonic waves are not recorded and the image can be formed directly form the ultrasonic amplitude of the acoustic near-field. As a result, the resolution is independent of the sensor's bandwidth and is solely define by the aperture of the SWED. With NSOAM no lateral

smearing of the image occurs and super-resolution imaging is performed, as the SWED aperture is much smaller than the wavelength emitted from the sample.

5.2 Acoustic near-field detection with a point sensor

In order to determine of the SWED can detect the acoustic near-field of a sample and perform bandwidth independent super-resolution imaging we recorded and analyzed ultrasound signals emitted from a sample at different distances.

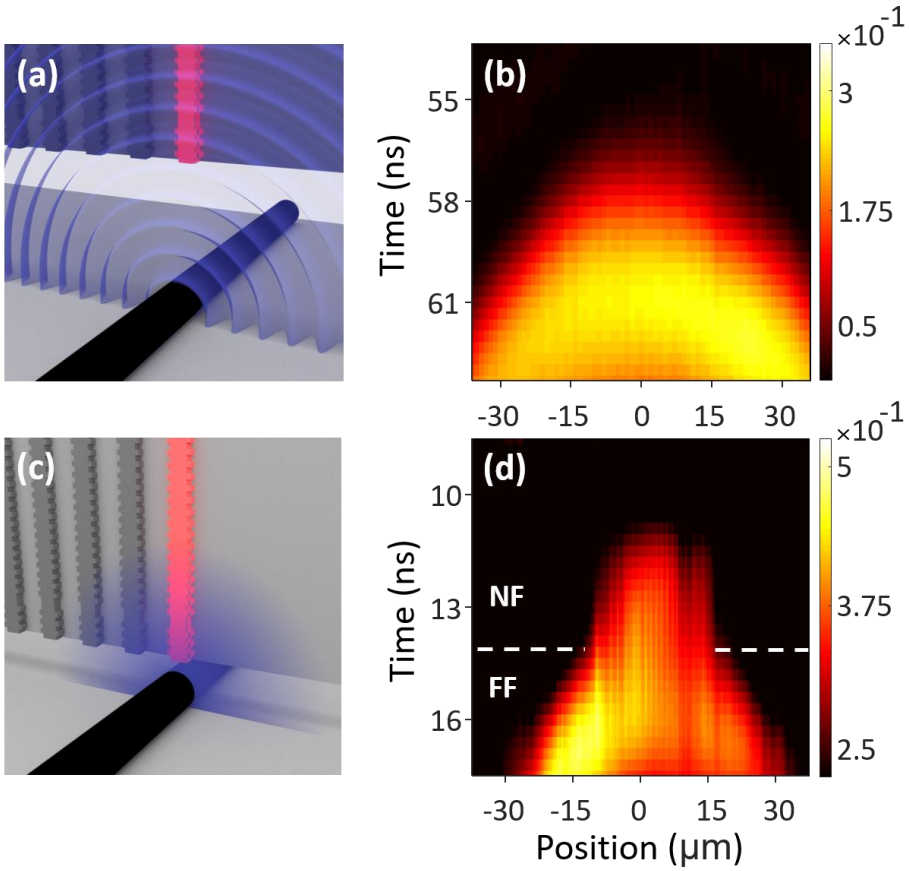

Figure 5.1 Near-field and far-field imaging with the SWED. (a) illustration of far-field imaging of a suture with the SWED. The propagating far-field is denoted in purple (excitation laser is not shown). (b) A B-scan with SWED4 over the suture when the sensor is in the far-field of the suture. (c) illustration of near-field imaging of a suture with the SWED. The evanescent near-field is denoted in purple (excitation laser is not shown). (d) A B-scan with SWED4 over the suture when the sensor is in the near-field of the suture. The white dashed line divides the arriving signals into signals detected in the near-field (NF) and signals detected in the far-field (FF).

Two B-scans with a step size of 1 µm were performed with SWED4 and the optoacoustic imaging setup described in **Section 6.5** over the cross-section of a polystyrene suture with a diameter of 30 µm (Dafilon Polyamide, B. Braun Melsungen AG, Germany). One B-scan in the acoustic far-field (**Fig. 5.1a**) 0.2 mm or 6.7λ from the sample, and the second in the near-field (**Fig. 5.1c**) 20 µm or 0.7λ away from the sample. In the far-field regime the detected acoustic signals exhibit no distinguishable features (**Fig. 5.1b**) and the B-scan has to be reconstructed in order to form an image. On the contrary, in the near-field regime a sharp transition between the acoustic signals originating in the near-field (**'NF'; Fig. 5.11d**) and the far-field is observed (**'FF'; Fig. 5.11d**) is observed. The far-field signal experiencing a time delay of ~3 ns, this differentiation enables image formation only from the evanescent signals originating in the near-field, without the need of reconstruction.

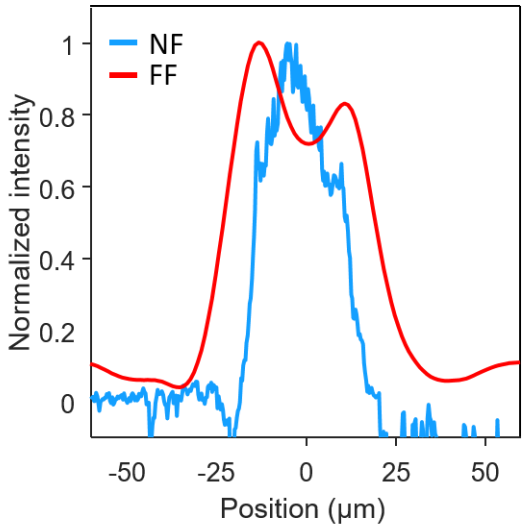

Figure 5.2 Normalized intensity profile along the cross section of a 30 µm suture, imaged with SWED4 in the far-field (FF) and the near-field (NF).

Fig. 5.2 shows the normalized intensity along the diameter of the suture in the far-field and the near-field. In the far-field case the image was reconstructed before taking the intensity profile. The FWHM of the curves shows that the far-field imaging experiences slight blurring of the resulting in a suture width of 41 µm, while the near-field imaging shows no such blurring resulting in a width of 26 µm. The latter value is somewhat smaller than the specified value, the difference is attributed to the circular shape of the suture resulting in a varying distance between the suture surface and the SWED during imaging.

5.3 Resolution characterization

In order to confirm the sub-wavelength resolution enabled by the dimensions of the SWED, we benchmarked the NSOAM with SWED4 against a high-end optical confocal microscope with 60x / NA=1.2 water immersion objective achieving lateral resolution of ~230 nm (see **Appendix C**). We measured the edge spread function (ESF) from a straight edge on a 1951 USAF resolution test target (Edmond Optics; Barrington, USA) with both systems. SWED4 resolved the edge with virtually the same ESF as the confocal microscope (**Fig. 5.3a**). Using Richardson-Lucy deconvolution and the optical point spread function (PSF) of the confocal microscope, we were able to obtain the true edge profile of the target sample. Deconvolving it from the acoustic ESF measured by SWED4, we were able to estimate the PSF of the SWED (see **Appendix C**). We found the PSF of the SWED to be 650 nm (**Fig. 5.3b**), which is close to the manufactured sensing area of the detector, confirming the sub-micron detection capability of sound.

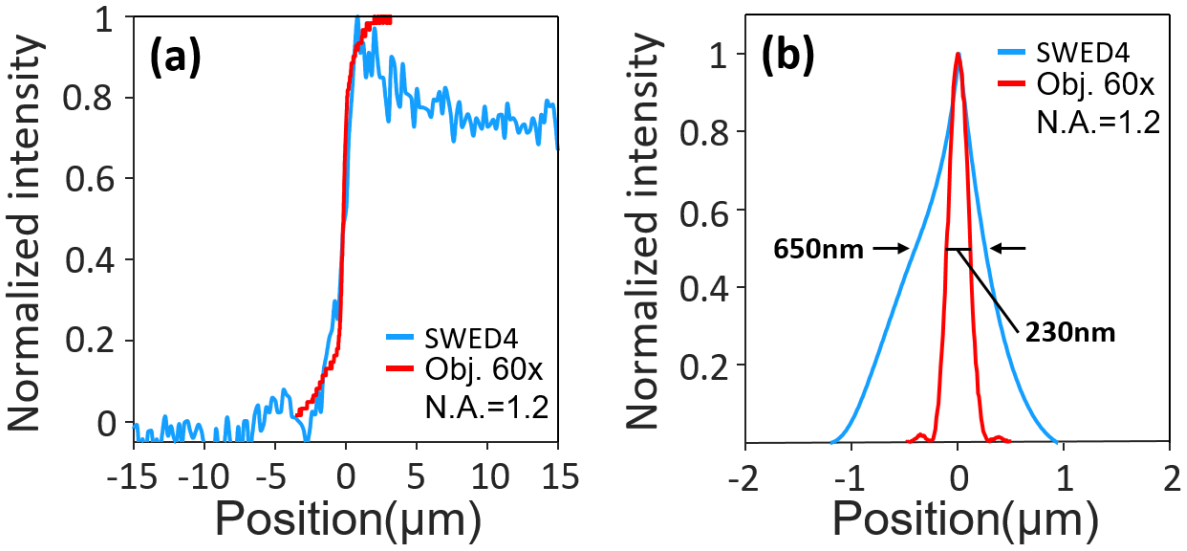

Figure 5.3 Resolution calibration of SWED4 in the near-field and confocal microscope with 60x / NA=1.2 water immersion objective. **(a)** Edge spread function of a marking with a straight edge on the 1951 USAF resolution test target acquired with SWED4 in the near-field and the confocal microscope. **(b)** Acoustic point spread functions of SWED4 and the optical point spread function of the confocal microscope.

This result showcases a key point of the SWED. Even though imaging of the edge is performed herein at 46MHz (**Fig. 4.10f**), with expected diffraction blurring of ~20 μm (**Section 4.4**), the target

is instead imaged with a resolution of 0.65 μm, exhibiting a 50-fold sub-wavelength imaging (super-resolution) performance.

5.4 NSOAM with a point sensor

We proceed by demonstrate the superior image quality offered by the NSOAM with the SWED compared to the far-field optoacoustic tomography. Using SWED4 and the system in **Section 6.5** we imaged two phantoms, the first is constructed from black circles printed onto a microscope cover slip (IMT masken und teilungen AG; Greifensee, Switzerlans). The circles are ordered in a rectangular periodic pattern with a period of 320 μm and circle diameter of 160 μm. The second is a marking in a shape of the letter '6' on a 1951 USAF resolution test target.

The first phantom was imaged both at the acoustic far-field (**Fig. 5.4a**) and near-field (**Fig. 5.4c**), 0.37 mm and ~20 μm away from the phantom respectively. In both cases area of 0.35×0.35 mm^2 around one circle was covered with a step size of 10 μm. Reconstructed Maximum intensity projection (MIP) of the far-field scan (**Fig. 5.4a**) reveals substantial blurring of the image relative to the original size of the phantom (white dashed circle in **Fig. 5.4a**). On the other hand, MIP of the near-filed scan (**Fig. 5.4c**) reveals no such blurring with well-defined and sharp boundaries of the phantom. In the near-field imaging only signals originating from the near-field of the phantom were used in image formation (**Fig. 5.1d**). **Fig. 3e** shows the edge spread function recorded along the edge of the first phantom imaged by SWED4 in the far-field and near-field (the edge is indicated by the white arrows in **Fig. 5.4c**). Here we demonstrate that the NSOAM is able to resolve the edge of the phantom much better compared to the bandwidth dependent optoacoustic tomography.

The second phantom was imaged at the acoustic far-field (**Fig. 5.4a**) and near-field (**Fig. 5.4c**) as well, 0.2 mm and ~15 μm away from the phantom respectively. In both cases area of 0.2×0.2 mm^2 around the marking was covered with a step size of 2 μm. Reconstructed MIP of the far-field scan (**Fig. 5.4b**) shows blurring of the marking due to bandwidth limited resolution and lateral smearing. On the other hand, MIP of the near-field scan (**Fig. 5.4d**) shows no such blurring and in addition reveals many features (scratches and other damage) that were not visible in the far-field. **Fig. 5.4f** shows the profiles of the target along the white dashed lines in **Fig. 3.4b,** both in the far-field and

near-field (**Fig. 3f** and **Fig. 3h** respectively). We again demonstrate that NSOAM is able to achieve superior contrasted and resolution resulting in well-defined and sharp boundaries of the target.

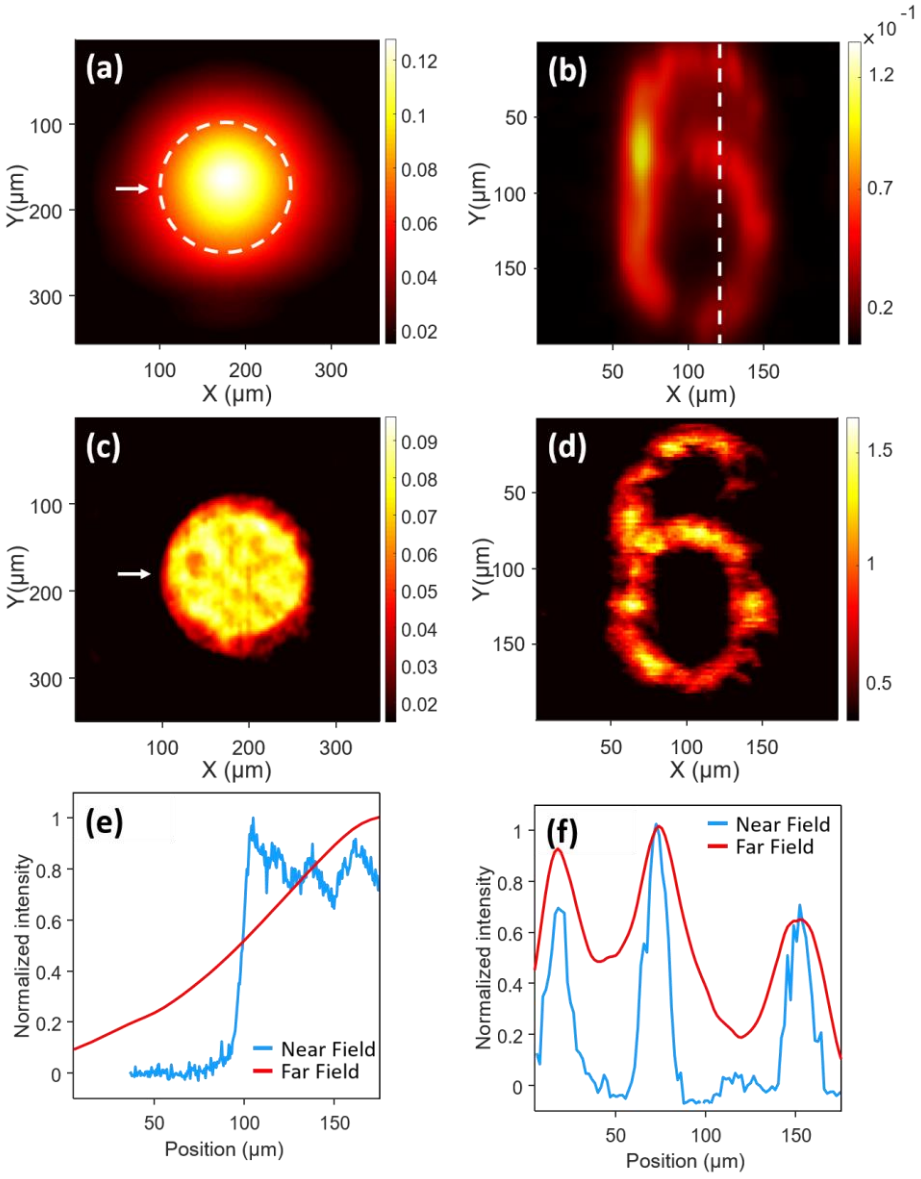

Figure 5.4 Optoacoustic tomography and NSOAM imaging with the SWED. **(a)** Maximum intensity projection (MIP) of a reconstructed image of the periodic phantom acquired with SWED4 in the far-field. The dashed circle indicates the original boundaries of the imaged phantom. **(b)** MIP of a reconstructed image of a marking on the resolution target acquired with SWED4 in the far-field. **(c)** MIP of one circle imaged by SWED4 when only the signals from the near field are used in image formation. **(d)** MIP of an image formed only from the near-field signals acquired with SWED4. **(e) c**omparison of the normalized intensity along the edges of the circles in panel (b) and (d), denoted by the white arrows in (c). **(f)** Comparison of the normalized intensity of the tomographic (b) and NSOAM (d) images along the vertical dashed lines in panel (b).

We also compare the quality of images acquired by NSAOM with SWED4, representing optical absorption contrast, to images acquired with the high-end optical confocal microscope with 60x / NA=1.2 water immersion objective, representing optical reflection contrast.

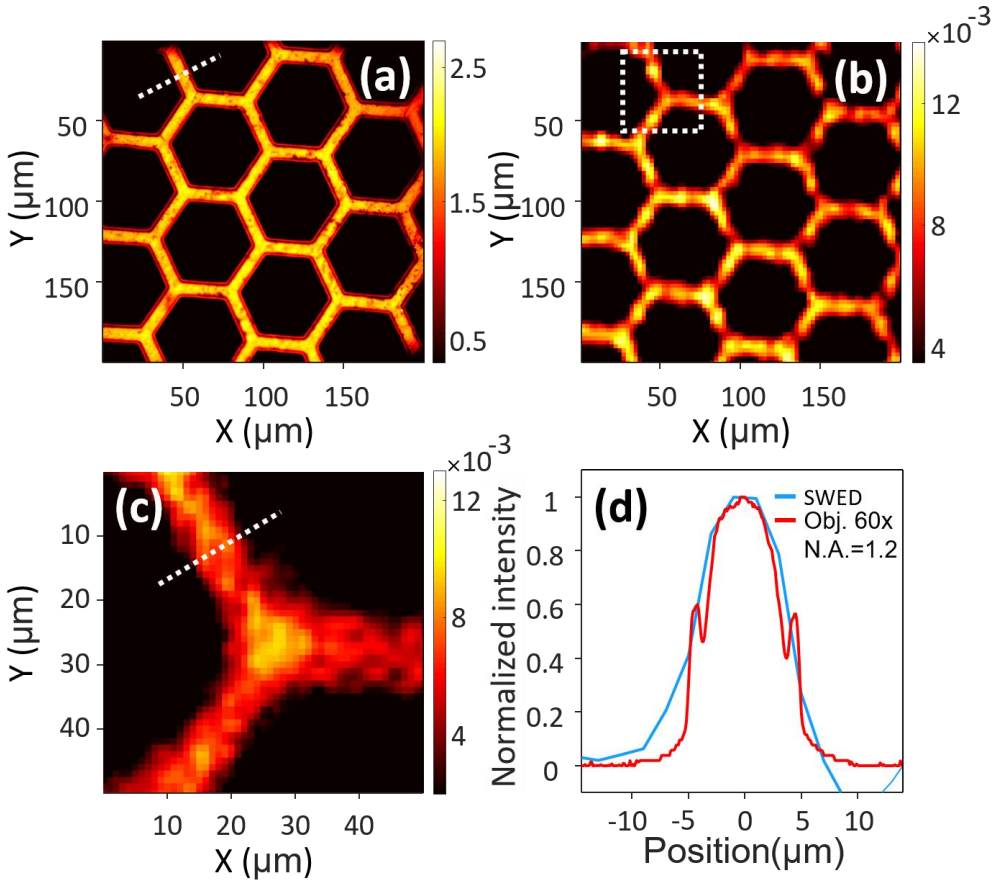

Figure 5.5 Comparison of NSOAM imaging with the SWED to imaging with optical confocal microscope with 60x / NA=1.2 water immersion objective. **(a)** Image of a gold hexagonal grid acquired by a confocal microscope. **(b)** Image of the same hexagonal grid acquired by SWED4 in the near-field. **(c)** enlargement of the section enclosed by the white dashed line in panel **(b). (d)** Comparison of the normalized intensity along the dashed lines in panel (a) and (c).

Both the optical microscope (**Fig. 5.5a**) and the SWED (**Fig. 5.5b**; 0.43λ from the sample) imaged an area of 0.2 × 0.2 mm^2 of a thin metallic hexagonal grating (G400HH, SPI Supplies; West Chester, USA) used for calibration of electron microscopes. The step size of the microscope was 100 nm and that of the SWED was 5 μm. The resolution of the SWED is ~3 -fold worse than that of the microscope, but the resolution in **Fig. 5.5b** is noticeably worse mainly because it is limited by the scanning step size. Image of the section enclosed by the white dashed line in **Fig. 5.5b** with a finer step size of 2 μm shows that the NSOAM with the SWED is able to resolve the finest

features of the sample without adding any artefacts (**Fig. 3c)**. A detailed comparison of the profiles taken along the white dashed lines in **Fig. 5.5a** and **Fig. 5.5c** reveals that both the optical microscope and the SWED produce images of similar contrast. The width of the bar determined by the FWHMs of the curves in **Fig. 5.5d** is measured to be ~ 9 μm for both the microscope and the SWED, which is in close proximity to the specs (= 8 μm).

5.5 Discussion and conclusions

This chapter describes a novel imaging modality: the near-field scanning optoacoustic microscopy (NSOAM), enabled by the sub-micron aperture of the SWED. We demonstrated acoustic resolution of 650 nm which is close to the optical resolution achieved by a high end microscope with 60x / NA=1.2 water immersion objective. The main difference of NSOAM compared to other near-field acoustic microcopy techniques and the near-field scanning optical microcopy is that NSOAM detects the acoustic evanescent near-field of the sample itself, while the other techniques use the acoustic or optical near-field emitted from a sharp tip. In the first case the sensor has to be at a distance smaller than the wavelength of the evanescent waves, which due to the long acoustic wavelengths can be between tens to hundreds of microns. In the latter case, as the waves diffract form a sub-wavelength tip, the distance to which the near-field extents from the aperture is defined by the Fraunhofer length which equals to $2 \cdot \phi_d/\lambda$, where ϕ_d is the diameter of the aperture. As the apertures in those modalities tend to be around 100 nm or less, the sharp tip has to be positions few tens to few hundreds on nanometers from the sample, this often requires complex feedback mechanisms. This requirement also poses a tradeoff between the distance of the tip from the sample (or the complexity of the system) and the achievable resolution. In NSOAM such tradeoff does not exist and the resolution is defined solely by the aperture of the sensor. Another notable difference is that NSOAM images absorption contrast while the other modalities image elastic contrast.

The NSOAM image acquired by the SWED of a flat marking on a 1951 USAF resolution test target shows $\lambda/50$ resolution and image features that could not be observed before with optoacoustic tomography. We also show that NSOAM image quality is close to the quality achieved with a high-end expensive optical confocal microscope with 60x / NA=1.2 water immersion objective. Such microscopes have a price range of few tens of thousands USD. On the contrary, the silicon-

photonics technology used to manufacture the SWED has a typical cost of few USD/mm^2. Therefore, the NSOAM modality with the SWED can be a lensless alternative to high resolution optical and optoacoustic microscopes. As the resolution of NSOAM is independent of the excitation wavelength and depends only on the aperture of the SWED, NSOAM might be very attractive for microscopy applications that utilize wide range of wavelengths for which optical system aberrations cannot be neglected.

6. Materials and Methods

In this chapter we discuss in depth the design and manufacturing methods of the π-WBG and SWED sensors. We continue by describing the various systems developed during this work and used for characterization of the π-FBG, π-WBG, and SWED sensors and imaging with the SWED sensor.

6.1 Sensor design and chip layout

In this section we start by describing the design of the basic photonic components used to assemble the chip layout (for principle of operation of those components refer to **Section 3.3**). We follow by explaining how those components were interconnected and what were the guiding principles behind their placement relative to each other on the layout.

The chip layout was designed using Optodesigner software (PhoeniX Software; Enschede, Netherlands). It consists of several components: waveguides, grating-couplers, Bragg gratings, and arrayed waveguide gratings. (The arrayed gratings were not used in the present study and are not discussed here). It is important to note that due to process variations and limited resolution of the lithography process [38] the dimensions of the components may vary which effects their operation [71]. Specifically, the corrugation of the Bragg grating is not rectangular as designed but more closely resembles sinusoidal [78]. This results in weaker grating (**Eq. 3.4.6**) and has to be accounted for during the design stage.

Fig. 6.1 and **Fig. 6.2** depicts the designs of each component. White – the 220nm Si device layer, blue – deep etch of the Si to expose the SiO_2 bottom cladding, red – shallow etch of ~ 70 nm. **Fig. 6.1a** shows a focusing grating coupler similar to the one reported in reference [70]. The dimensions of the grating are suitable for coupling of a single mode fiber with a core of ~ 9 μm ,period of $\Lambda = 630$ nm was chosen to maximize transmission around the wavelength of ~ 1550 nm for SiO_2 as top cladding, and a short taper length of only ~ 20 μm is sufficient to couple to a rectangular single mode waveguide due to the focusing properties of the grating coupler. **Fig. 6.1b** shows a curved Si

rectangular waveguide used to connect two perpendicular waveguides. The curved waveguide has identical dimensions to a straight waveguide of 220 × 450 nm^2 and curvature radius of ~9 µm, for this radius the excess bend loss (compared with a straight waveguide with the same length) was reported to be negligible [66]. Such a small radius of curvature is possible due to the high index of contrast of the SOI platform.

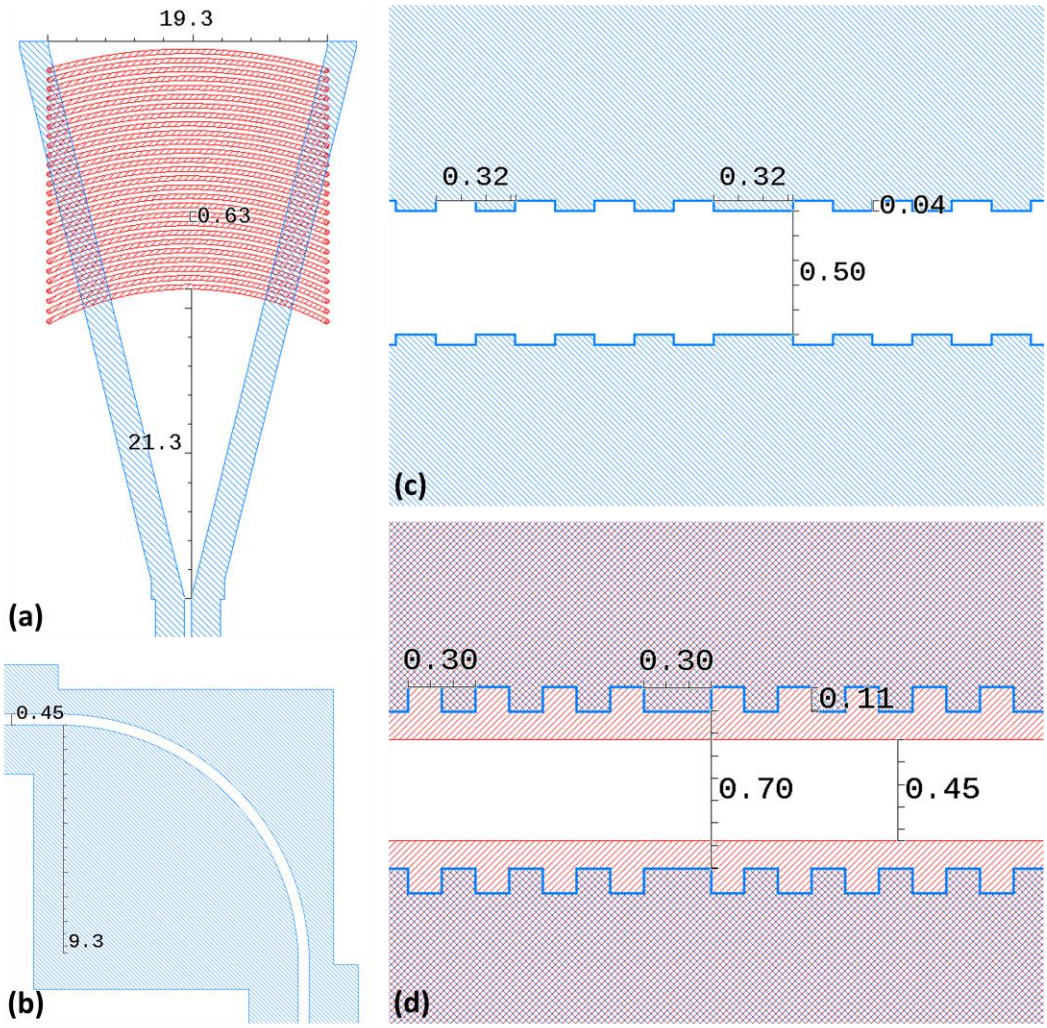

Figure 6.1 Design of basic photonic components used in assembling the chip layout. **(a)** Grating coupler. **(b)** Curved Si waveguide. **(c)** Section of a strip π-WBG. **(d)** Section of a rib π-WBG. White – the 220nm Si device layer, blue – deep etch of the Si to expose the SiO_2 bottom cladding, red – shallow etch of 70 nm.

Fig. 6.1c shows a section of a π-WBG around the phase-shifted section based on a rectangular silicon waveguide with a cross-section of 220 × 500 nm^2. The cross-section, period of the Bragg grating, and the length of the phase shifted section were chosen to be the same as reported in

references [64], [79] in order to have a resonance wavelength around 1550 nm. No corrugation larger than Δw = 40 nm was chosen, larger corrugations with similar waveguide dimensions were reported reduce the visibility of the resonance without notifiable increase in Q-factor [64]. The effect of larger corrugation on sensor performance would be reduction in the dynamic range without considerable increase in the sensitivity. **Fig. 6.1c** shows a section of a π-WBG around the phase-shifted section based on a rib silicon waveguide. The slab cross-section is 150 × 700 nm^2 and the ridge cross-section is 70 × 450 nm^2. The ridge width was chosen to be under 750 nm in order to fulfil the single mode condition [66] and the strip width was chosen to be identical to the one set for the straight and curved Si waveguides for connection without the need of a taper for the strip section. The Bragg period was reduced in order to compensate for the increase in n_{eff} compared to the rectangular waveguide (**Section 3.4.3**). Such grating with corrugation as large as Δw = 60 nm were reported before but were demonstrated to be not sufficiently strong for our applications [77], hence in this work the corrugation was increased up to Δw = 160 nm. Connection of devices with different widths was done using adiabatic tapers of ~ 15 µm (**Fig. 6.2**). Tapers of rib waveguides to rectangular strip waveguides (**Fig. 6.2** - bottom) were done by changing the width of the strip region only as demonstrated in reference [66].

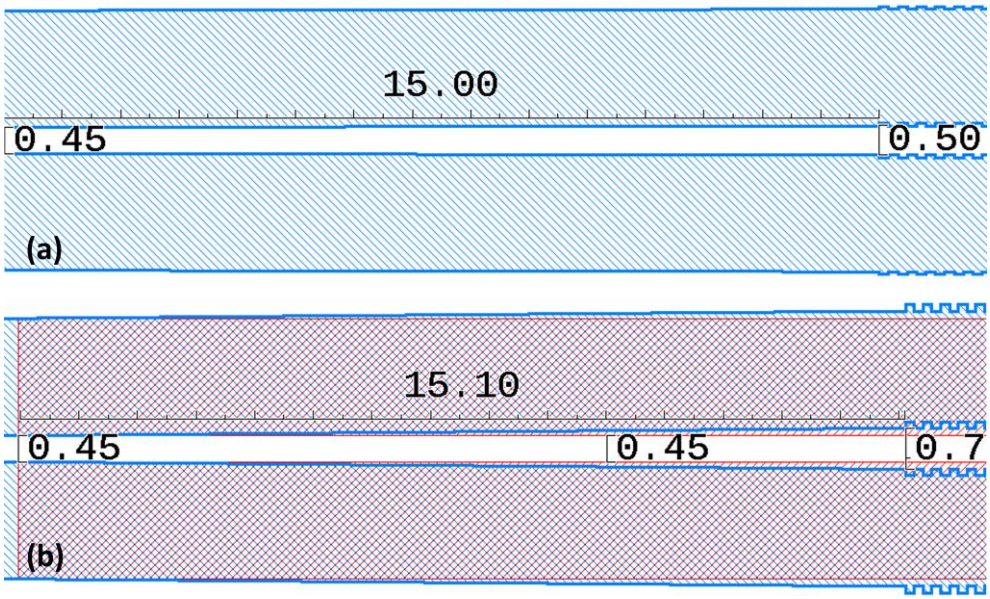

Figure 6.2 Design of adiabatic tapers used in connecting components of different cross-sections in the chip layout. **Top:** Strip taper. **Bottom:** Rib taper. White – the 220nm Si device layer, blue – deep etch of the Si to expose the SiO_2 bottom cladding, red – shallow etch of 70 nm.

Fig 6.3 depicts the chip layout assembled from the components in **Fig. 6.1** and **Fig. 6.2**. This layout appeared on the mask used for the UV-lithography and was directly imprinted on the SOI wafer. Two arrays of π-WBG sensors were placed in the centre of the layout. They are connected to arrays of input and output grating couplers that were placed close to the edges of the chip, as far as possible from the sesnors. This was done to leave room for fiber array blocks for connectorizaion of the chip. During connectorization epoxy is used to attach the blocks to the chips, if the block is too close to the sensor there is danger that the sensor would be covered in epoxy, this epoxy layer could produce acoustic index mismatch and mask the ultrasonic signal. In addition, if the blocks are too close to the sensors they can block the ultrasonic signal and reduce the sensor field of view. Other devices were inserted the empty spaces between the sensor arrays but they are not discussed in this work.

Fig 6.4a shows an enlargement of the array enclosed by the black dashed line '1' in **Fig 6.3**. The eight 250 µm-long π-WBGs are clearly visible, the pitch of the array was set to 10 µm in order to avoid potential process variations associated high loading (device density) [109]. The sensors are connected on each side to rectangular Si waveguides with cross-section of 220×450 nm^2 via a taper. **Fig 6.4b** shows an enlargement of the grating couplers enclosed by the black dashed line '2' in **Fig 6.3**. The couplers have a spacing of 127 µm in order to match the pitch of the fiber arrays. The couplers are connected to rectangular silicon waveguides leading to the sensor arrays. The rightmost coupler is connected to two sections of curved silicon waveguides that lead to a waveguide connecting to another grating coupler. This pair is required for alignment during connectorization..

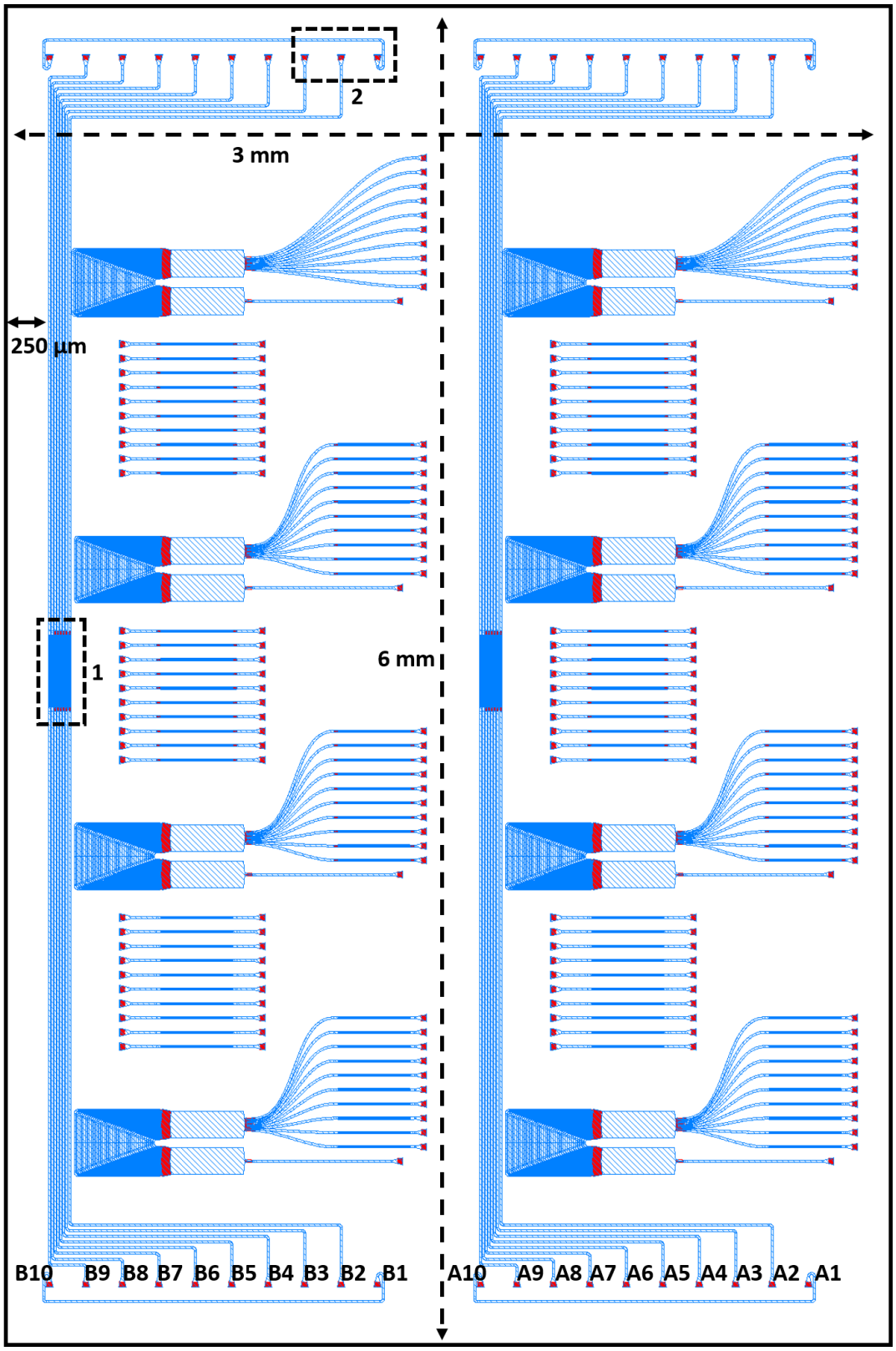

Figure 6.3 Chip layout. A2-A9 and B2-B9 are ports leading to two arrays of π-WBG sensors. A1, A2, and B1, B2 are shunt grating couplers required for fiber array block alignment during connectorization.

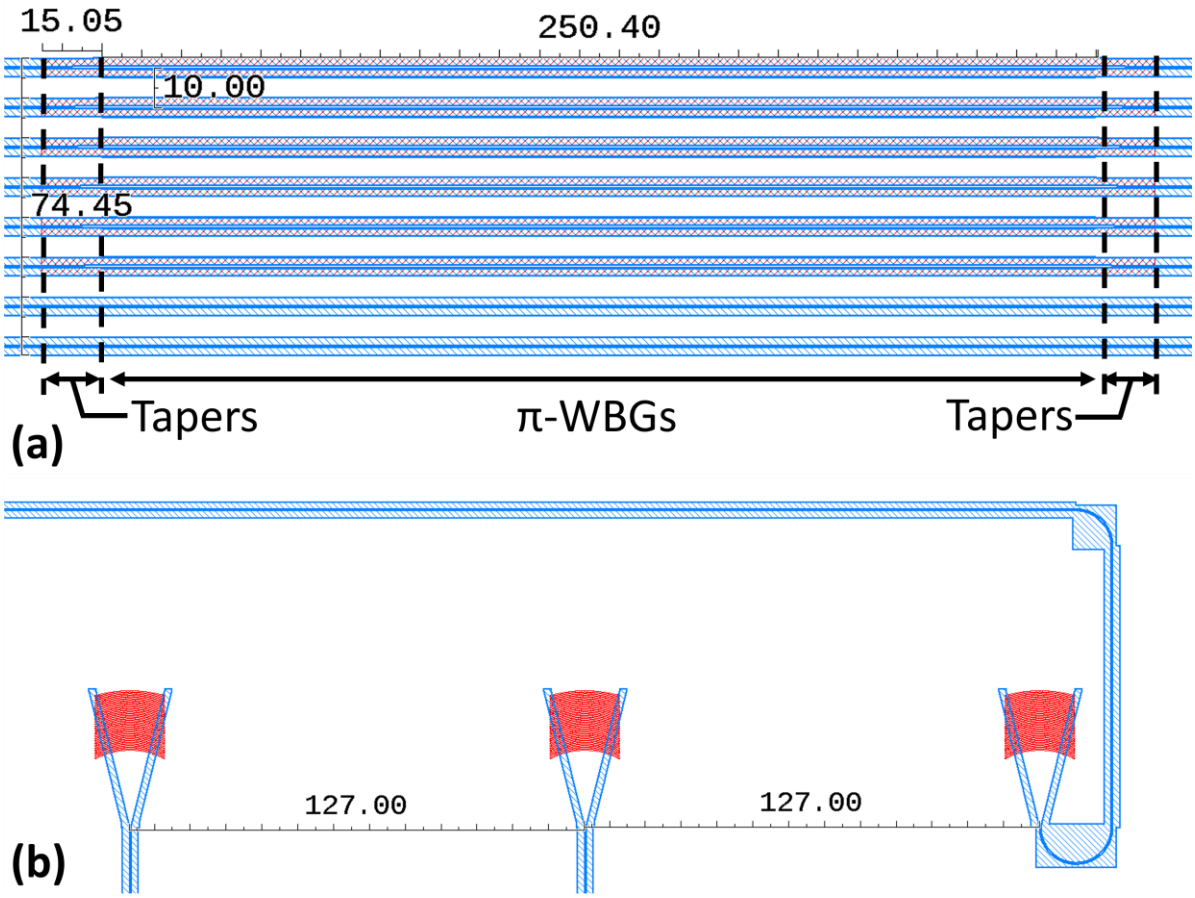

Figure 6.4 Design of the sensor arrays. **(a)** π-WBG sensor array. **(b)** grating coupler array connected to the sensor array.

6.2 Sensor manufacturing

In this section we start by describing the manufacturing process of the silicon chip as done in the foundry (**Section 6.2.1**). We also explain in details the additional steps and processes done in our lab in order to turn the raw SOI chip and the on-chip array of π-WBGs into an array of ultrasound sensors that can be directly mounted into an imaging system. **Section 6.2.2** describes the polishing process of the silicon chips and is relevant only for manufacturing of the SWED point sensors. **Section 6.2.3** describes the connectorization process of the chips to fiber array blocks, this is relevant for both the chips containing the π-WBG and SWED sensors.

6.2.1 Fabrication

The chips containing the sensors were fabricated at Interuniversity Microelectronics Centre (IMEC; Leuven, Belgium) through the ePIXfab Consortium Service on an 200mm SOI wafer with silicon orientation of (100). The wafer consisted of the following layers (**Fig. 6.5a-b**): Si substrate of ~ 700 µm, a layer of SiO_2 1.5 µm thick that functions as the bottom cladding and also known as back oxide (BOX), 200 nm Si layer known as the device layer with the layout etched on it, and a top cladding consisting of 1.25 µm SiO_2 or 5 µm polymer resist. The main fabrication techniques included UV-lithography on a standard I-Line resist followed by a two-step etch process of the silicon, involving a shallow etch (70 nm) and a deep etch (220 nm).

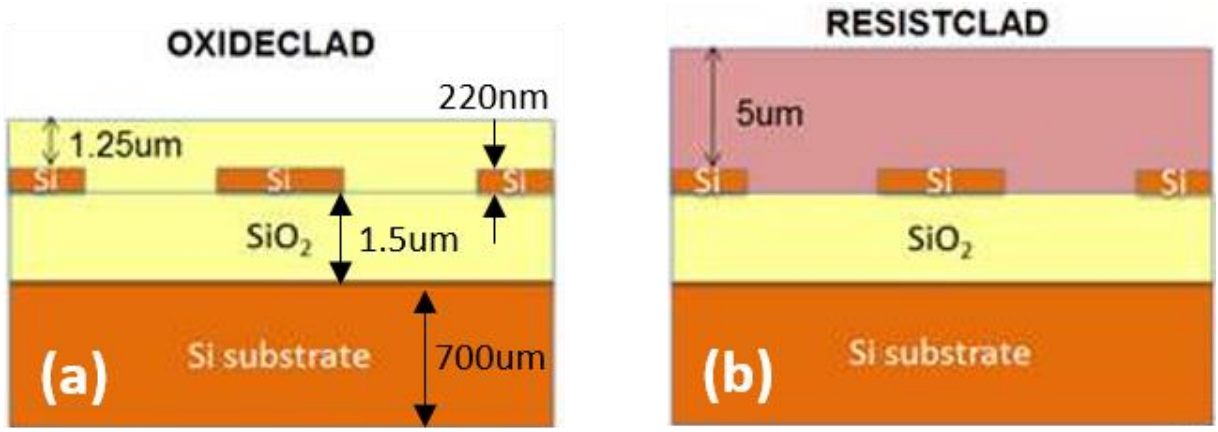

Figure 6.5 Cross-section of the SOI wafer with **(a)** SiO_2 and **(b)** polymer resist top claddings.

6.2.2 Post processing

After manufacture, the wafer was diced in fab to chips measuring 6 × 3 × 0.7 mm, where the π-WBG are located parallel to the long dimension of the chip at a distance of 250 µm from the long edge (**Fig. 6.6a**, The red arrow indicates the location of the phase shifted section).

To create the silicon waveguide etalon detector (SWED) additional process steps were performed in-house. The chip was cut perpendicular to the orientation of the π-shifted Bragg grating etalons at a distance of approximately 500 µm from the phase shifted region (**Fig. 6.6a**, red arrow). The cut was performed by fixing one side of the chip in a specially designed clamps with soft tips manufactured by the workshop of Helmholtz Zentrum München, and scribing the top cladding with a ruby fibre scribe (S90R, Thorlabs). Then the chip was cleaved by exhorting pressure on the

exposed side. After optical grade polish of the cleaved faced the chip would approximately measure 3 × 3 × 0.7 mm (**Fig. 6.6b**).

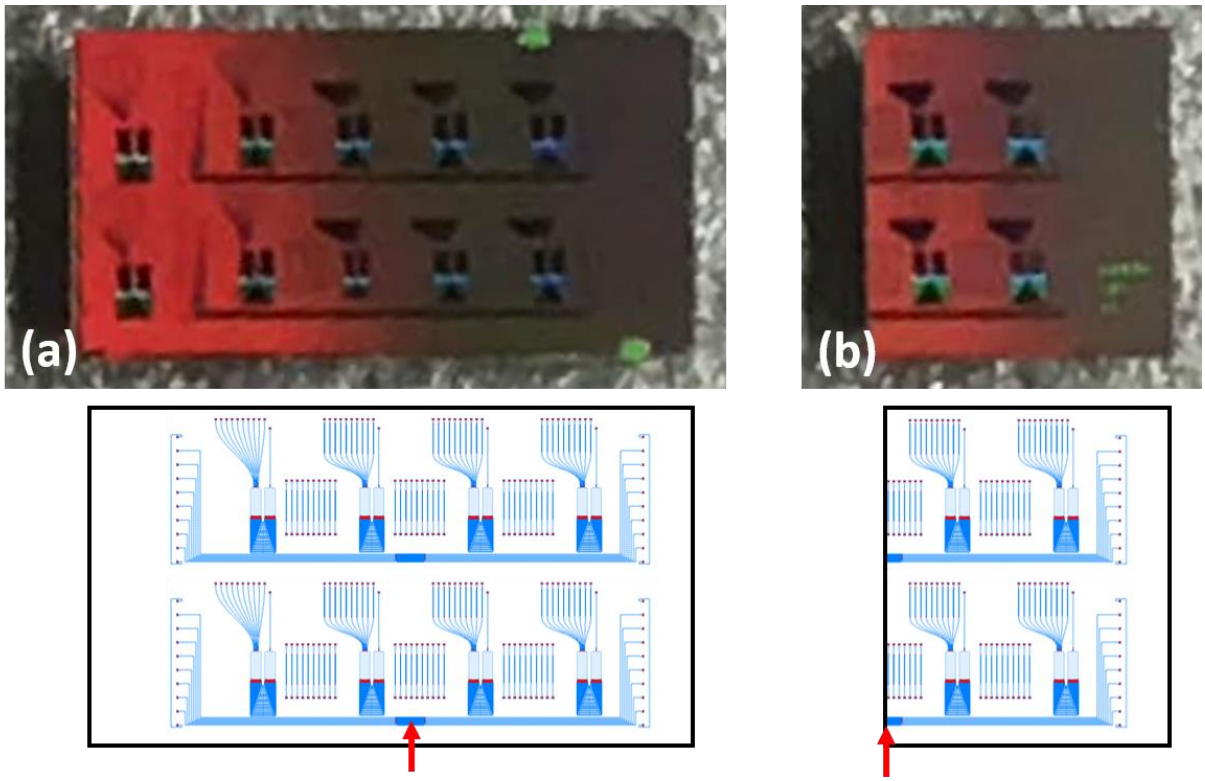

Figure 6.6 Diced SOI chips. **(a)** As delivered from the fab. **(b)** After in-house dicing and polishing. The layouts are depicted at the bottom for orientation. The red arrow indicate the location of the phase shifted sections.

The polish process was performed with progressively finer diamond-grit polishing films (grit size from 0.1 to 30 µm), followed by a final polish with SiO_2 lapping film (grit size 0.02 µm). **Fig 6.7** depicts the facet of the chip during the polish process. **Fig 6.7a** shows the fast just after the cleaving, the facet is not flat and great amount of damage is visible close to the line of scribing. The 8 waveguides forming the sensor array are also visible in the device layer. Array width of ~80 µm is visibly smaller than the 125 µm single mode fibre present in the top right of the figure for comparison. **Fig 6.7b** shows the same facet after the polish with 0.1 µm film. The facet is flat but not of optical grade due to the many scratches and polish residue. **Fig 6.7c** shows the same after the last polishing step with the 0.02 µm film, now the facet is of optical grate and an image of a light spot formed by the illumination lamp is formed on the facet. The edge where the sensor array terminates has polish residue and must be cleaned before proceeding. The cleaning was performed

by sonication in distilled water, isopropanol, and acetone subsequently. The result is shown in **Fig 6.7d**, individual waveguides and their facets that terminate at the edge are clearly distinguishable.

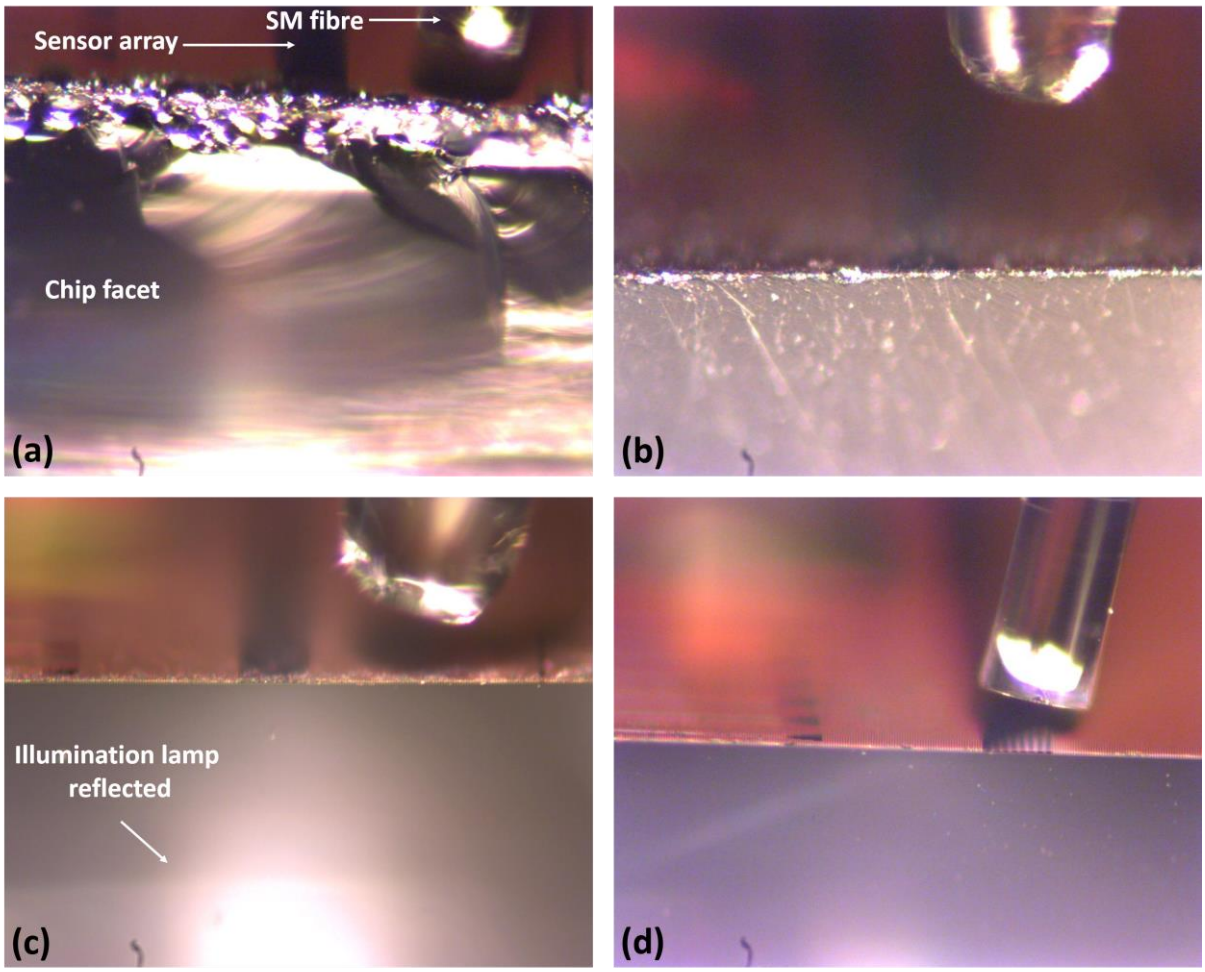

Figure 6.7 Polishing of the cleaved facet of the SOI chip. **(a)** After the cleaving before the polishing. **(b)** After polishing with progressively finer diamond-grit polishing films (grit size from 0.1 to 30 µm). **(c)** after the last polishing step with the 0.02 µm film. **(d)** After cleaning with sonication. 125 µm single mode fibre present in the top right of each figure for size comparison.

After polishing, the polished facet was coated by with a method that utilizes Ag diamine solution, which is also known as Tollen's reagent, and dextrose that reduces Ag ions to elemental Ag nanoparticles. Before applying the electroless wet chemical deposition solution, the polished facet was cleaned by sonication in distilled water, isopropanol, and acetone subsequently. The facet was immersed into Ag diamine solution and the reaction was activated by adding dextrose solution with 1:1 ratio to Ag diamine solution, resulting in an Ag thickness of ~200nm[110]. The changes in reflection spectra of the SWED were continuously monitored during the chemical deposition

process. The chip was removed from the chemical solution after obtaining a resonance within the reflection band, the coated chip was cleaned by rinsing with an adequate amount of distilled water in order to remove the residue from the chemical reaction.

The spectral responses of the devices were continuously monitored during the polishing process. **Fig. 6.8a** shows the reflection spectra of a π-WBG with Δw = 40 nm. A characteristic bandgap with a width of ~5 nm (at FWHM) is visible and can be attributed to the Bragg gratings. In addition, there is a 94 pm-wide resonance (at FWHM) in the middle of the bandgap attributed to the cavity section. When one of the Bragg gratings is almost entirely polished away, the confinement efficiency of the light in the cavity is drastically reduced and the resonance vanishes, as depicted in **Fig. 6.8b**. This indicated that the optical cavity is close to the polished facet. The distance between the cavity and the polished facet ("Spacer") was set to different values for each chip in the study. When the facet of the chip is coated with a thin reflective film (~200 nm Ag), the

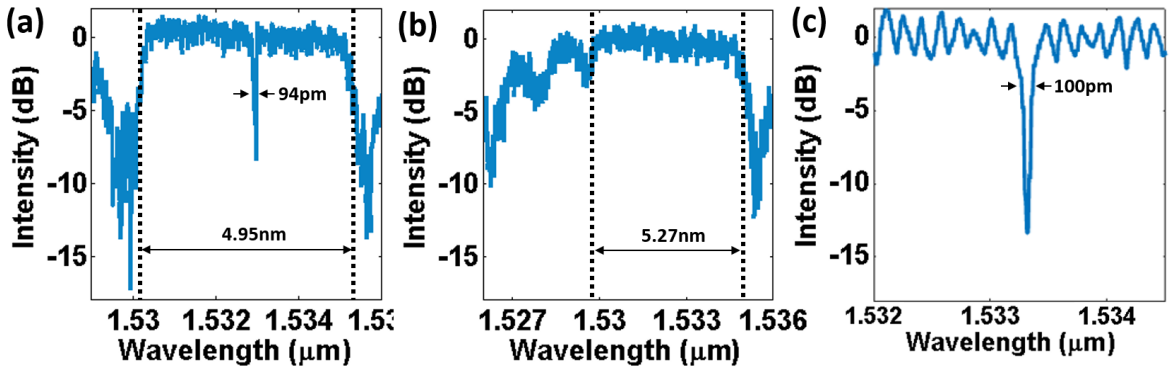

Figure 6.8 Monitoring the reflection spectrum of π-WBG with Δw = 40 nm during the polishing process of the SOI chip. **(a)** Before the start of polishing. **(b)** At the end of polishing. **(c)** After application of the reflective coating on the polished facet.

6.2.3 Packaging

Connectorization of the chips optical fibers was performed in-house using two types of fiber arrays both with a pitch of 127 μm. **Fig. 6.9a** depicts a schematic of a fiber array embedded in a planar block (PLC Connections; Columbus, USA) and **Fig. 6.9b** depicts a schematic of a fiber array embedded in a vertical block (Meisu Technology; Zhongshan, PRC). The main differences between approaches are:

1. The planer fiber array operates on the principle of the total internal reflection from the facet of the block. Hence if incident angle of θ on the fiber coupler is required the block facet has to be polished to an angle of:

$$\alpha = (90 - \theta)/2 \tag{6.2.2}$$

   While the vertical fiber array has a direct contact of block facet with the fiber coupler hence the facet has to be polished to an angle of θ.
2. As the sensors often operate in aquatic environment the facets of the planer blocks have to be coated with a reflective coating in order to maintain the total internal reflection condition.
3. Planar fiber arrays offer smaller device footprint but the vertical fiber arrays offer more stability and device robustness as a larger area of the block is in contact with the chip.

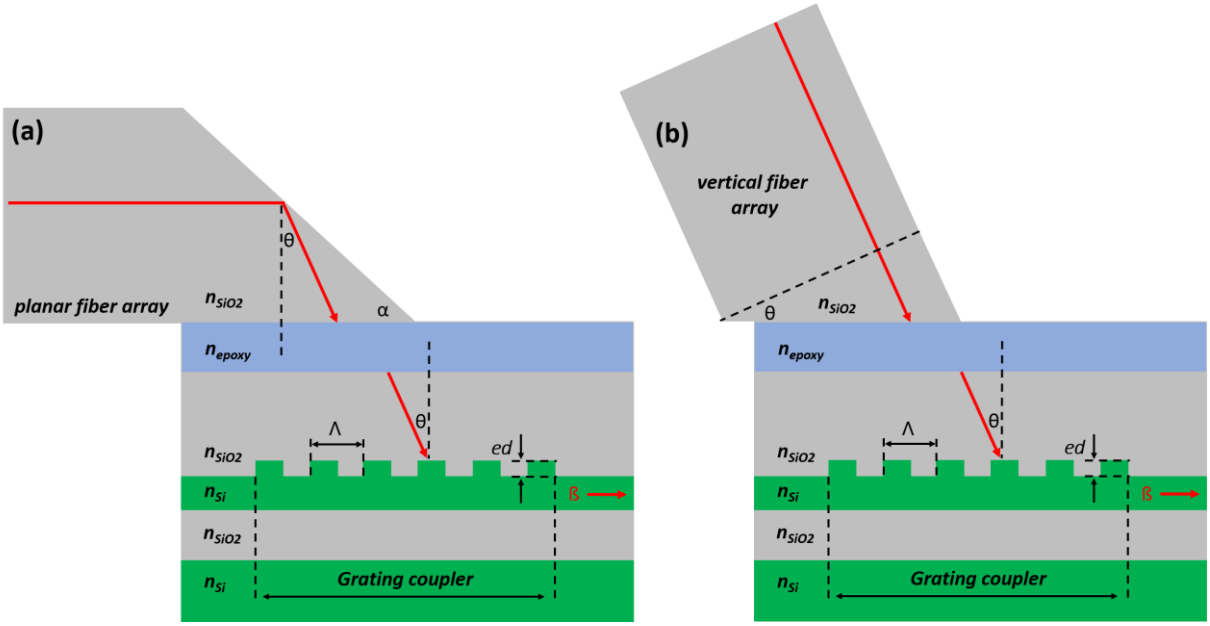

Figure 6.9 Schematic of a cross-section of a grating coupler on an SOI chip with SiO_2 cladding connectorized to fiber arrays with **(a)** planar fiber block **(b)** vertical fiber block. Blue layer depicts the epoxy glue, grey layer depicts SiO_2, and green layer depicts Si. The red arrow indicates the direction of the incident light. Λ – period of the grating coupler, θ – incident angle of the light, α – polish angle of the planar block, β – propagation constant, *ed* – depth of shallow etch.

In this work all the arrays composed of ten single-mode polarisation-maintaining fibres designed to excite the transverse electric mode. The fibres in the array act as input/output ports for the interrogation of each sensor and were individually connected to an interrogation scheme based on a tuneable CW laser in the C-band**.** The fiber arrays were glued to the chips using a UV-curable

epoxy (NOA81; Norland products, USA) that is transparent in the C-band with refractive index of $n_{epoxy} = 1.56$. The slight mismatch to the refractive index of SiO_2, $n_{SiO2} = 1.56$, merely results in lateral shift of the incident beam (**Fig. 6.9a-b**), which can be compensated for during the alignment procedure.

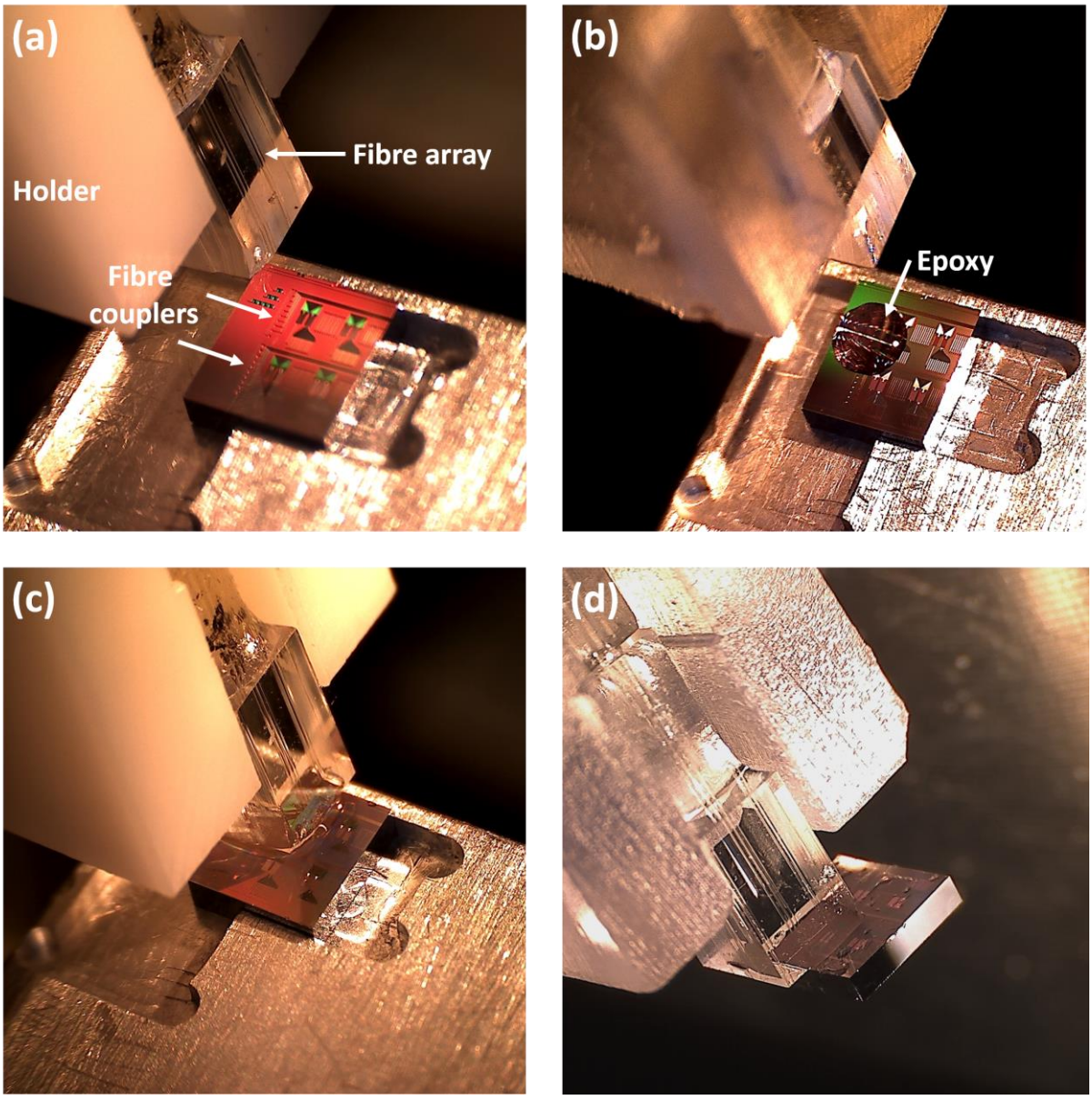

Figure 6.10 Aliment and gluing procedure of a vertical fiber array to a chip. **(a)** The array is held in a 3D printed holder and is aligned over the chip. The fiber couplers (grating couplers) are visible on the chip surface as glowing dots. **(b)** A drop of epoxy is deposited on the chip facet in the region of the fiber couplers. **(c)** The array is lowered and additional adjustment are done to the position to maximize the transmission. **(d)** After UV curing the device can be lifted from the chip holder and can be directly mounted onto an imaging system.

Fig. 6.10 depicts the aliment and gluing procedure of a vertical fiber array to a chip. **Fig. 6.10a** shows the fiber array mounted to a 3D printed holder and the chip is placed in a trench curved on an aluminium block with width of ~ 3mm and depth of ~ 0.5mm. The array holder is mounted on 2-axis manual translation stages (PT1; Thorlabs) and the aluminium block is mounted on a motorized translation stages in the z-axis (MTS50-Z8; Thorlabs). During the alignment procedure the two utmost fibers of the array are aligned using the stages with the two utmost grating couplers on the chip (**Fig. 6.3**, A1 and A10 or B1 and B10). Those shunt grating couplers are connected between themselves with a waveguide that closes the optical circuit and provide a transmission line for monitoring of the alignment efficiency. The position of the array over the grating couplers (**Fig. 6.10a**, 'fiber couplers') is adjusted to maximize the transmission between the utmost fibers and couplers. When the two utmost fibers are aligned this guarantee alignment of the other fibers, nevertheless the reflection spectrum from selected devices is fine-tuned by additional adjustment to the position with the stages.

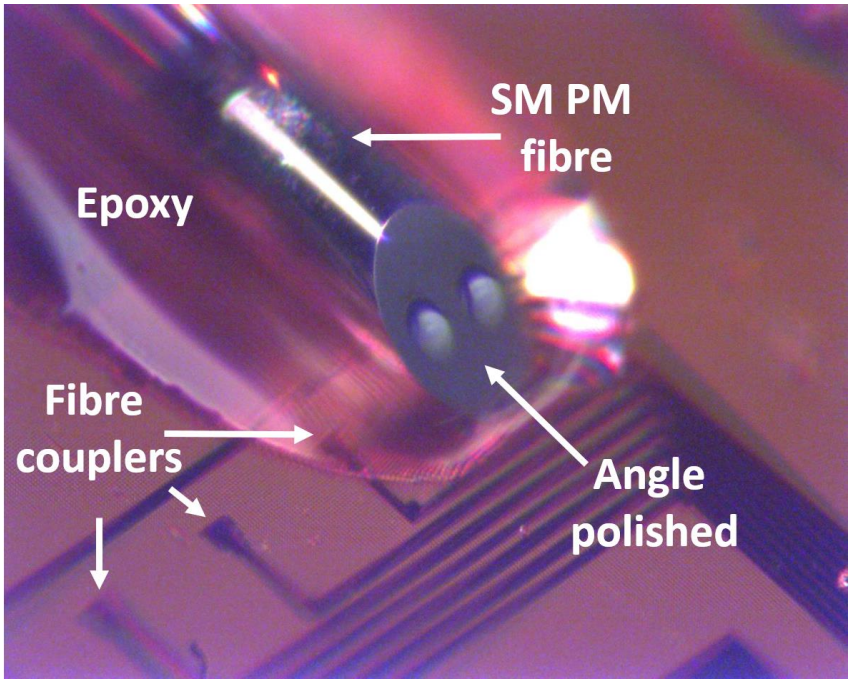

Figure 6.11 A micrograph of a chip connectorized to a single-mode (SM) polarization-maintaining (PM) fiber. The stress rods are visible as two circles on the angle polished fiber facet. Other fiber couplers (grating couplers) are visible to the left.

When the alignment is satisfactory the position of the z-axis stage is recorded and the stage is lowered to allow a drop of epoxy to be deposited on the chip facet (**Fig. 6.10b**). Then the z-axis

stage is returned to its original position (**Fig. 6.10c**) and slight position adjustments are made in direction of the optical axis of the waveguides leaving the grating couplers to account for the change in lateral shift of the optical beam due to the epoxy layer (**Fig. 6.9b**). When the transmission is satisfactory the epoxy is cured with a UV source. The resulting device is not removed from the 3D printed holder (**Fig. 6.10d**) and can mounted directly to an imaging system.

Connectorization of the chip to a single fiber is also possible. Similar to the planner array the facet of the fiber has to be polished to an angle (**Eq. 6.2.2**) and coated with reflective coating to ensure reflection from the facet. **Fig. 6.11** depicts a polarization-maintaining fiber oriented over a grating coupler, the stress rods (the two circles on the fiber facet in **Fig. 6.11**) are aligned horizontally over the chip to ensure excitation of the TE mode. By changing the orientation of the polished facet it is possible to selectively excite either TE or TM modes [51], [65]. The fiber is attached to the chip with a drop of UV curable epoxy (**Fig. 6.11**, 'Epoxy'). In general, this type of connectorization is less stable because of the smaller contact area between the fiber and the chip compared to the block in the fiber arrays.

6.3 Optical characterization setup

In this section we start by describing the setup used to readout the spectrum of the π-WBG and SWED devices on unconnectorized chips. The spectrum of the devices on the raw chips received from the foundry was recorded in order to confirm successful manufacturing and to estimate divergence from design parameters due to process variation.

In addition, this setup was used to monitor the shape of the spectrum during different post processing steps (**Fig. 6.8**), the spectrum is changing with each step and its shape has direct correlation to the sensor performance (**Section 3.4.4**).

Free space optical characterization is possible using the setup depicted in **Fig. 6.12**. List of equipment used to construct this setup can be found in **Table 6.1**. **Fig. 6.12a** depicts the general schematic of the setup. A continues-wave tunable laser in the C-band ('CW laser') with a polarized beam in the output is connected through an FC/APC connector to a single-mode non polarization-maintaining fiber, the other side of the fiber is cleaved and is mounted on top of the chip.

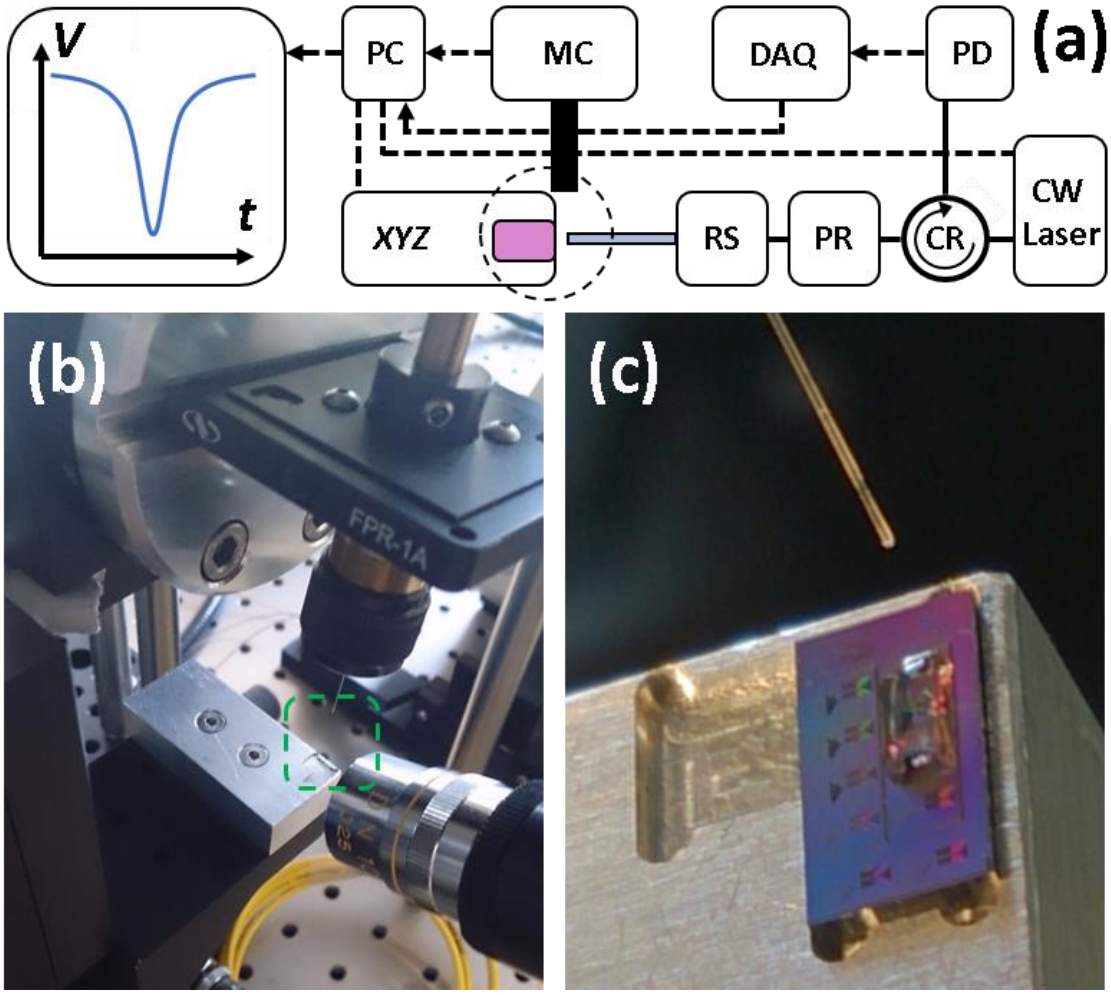

Figure 6.12 Optical characterization setup. **(a)** General schematic and principle of operation: CW, continuous-wave; CR, fiber circulator; PR, polarization controller; RS, rotational stage; XYZ, linear translation stages; PD, photodiode; DAQ, data acquisition card; MC, microscope cameras; PC, computer. **(b)** Micrograph of the section highlighted by the dashed circle in (a). **(c)** Micrograph of the chip in the holder (the area in (b) highlight by the green frame) with index matching fluid on its surface, the interrogating fiber is visible on the top.

The polarization orientation in the fiber is adjusted using a polarization controller ('PR') and the angle of the fiber relative to the chip is adjusted with a rotational stage ('RS'). The chip is specially oriented under the fiber using 3D stages ('xyz') over the grating coupler. The reflected light from the device attached to the grating coupler is collected by the same fiber and diverted using a fiber circulator ('CR') to a photodetector ('PD'). The signal from the photodetector is recorded with a digitizer ('DAQ') and the spectrum is analyzed on a computer ('PC'). The relative position of the chip and the fiber is visually adjusted using a microscope camera ('MC') connected to a microscope objective with a long working distance. **Fig. 6.12b** shows a photograph of the microscope camera,

the fiber help by the rotational stage, and the aluminum block with the trench used to hold the chip. **Fig. 6.12c** is an enlargement of the area enclosed by the green dashed line in **Fig. 6.12b**, the fiber and the chip held by the aluminum block are clearly visible. A drop of liquid on the chip in **Fig. 6.12c** is also visible, and is sometimes used to better match the optical refractive indexes of the fiber and the top cladding of the chip.

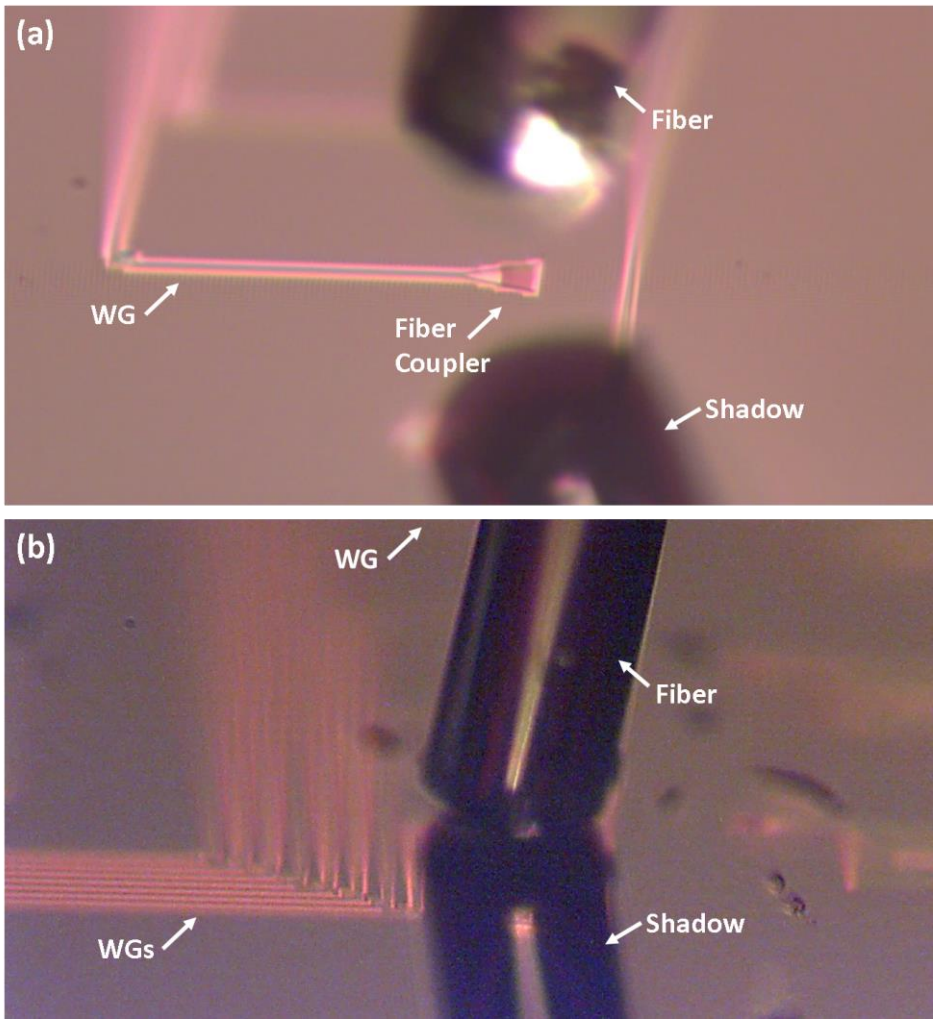

Figure 6.13. Alignment procedure of the interrogating fiber over a fiber coupler (grating coupler). **(a)** Micrograph of the fiber being roughly positioned on top of the fiber coupler by manual movements of the translational stages in the *x* and *y* directions. A waveguide leading from the fiber coupler to a resonator and the fiber's shadow are also visible. **(b)** Micrograph of the fiber and its shadow meet over the fiber coupler after movement of the translational stages in the *z* direction.

The alignment procedure of the cleaved fiber tip over a grating coupler is depicted in **Fig. 6.13.** First using the rotational stage the angle of the pitch angle is adjusted to the desired value. The yaw

angle of the fiber is not important as it can be compensated using the polarization controller. The system described in **Fig. 6.12** does not have the degree of freedom to adjust the roll angle but it was found experimentally that the relative alignment of chip and fiber holders is sufficiently good to neglect this degree of freedom. Using the linear translation stages the chip is moved so the desired grating coupler is found in close proximity to the fiber and the illumination lamp adjusted so a shadow of the fiber is formed on the surface of the chip (**Fig. 6.13a**). The fiber would couple to the chip when the image of the fiber and its shadow meet exactly on top of the grating coupler (**Fig. 6.13b**). During the aliment procedure the CW laser works in sweeping mode and the reflected light from the chip surface is collected and the spectrum is analyzed. When the fiber is well aligned over the grating coupler a recognizable shape of the spectrum appears. Fine tuning of the position might be required to improve the transmission efficiency.

Table 6.1: List of equipment for optical characterization

CW Tunable laser TL1550-B-INTUN-PM (Thorlabs). Wavelength span 1519-1630 nm (C band); Optical power 20 mW; Effective linewidth 1.5 MHz; Wavelength repeatability 10 pm; Wavelength resolution 0.5pm.
Photodetector PDB480C-AC (Thorlabs). Wavelength 1200 -1700 nm; Bandwidth 30 KHz – 1.6 GhZ; Transimpedance gain 16 x 10^3 V/A.
Microscope Camera EO-1312C color USB camera (Edmund optics) coupled to a microscope objective DIN x10, NA = 0.25, WD = 10.8 mm (Edmund optics) through a 16mm C-mount tube assembly.
Rotational stage M-481-A (Newport) with M-481 screw.
Fiber holder FPR-1A XYZ fiber optic positioner (Newport) with a FPH-S (Newport) chuck for bare fibers.
Polarization controller FPC561 (Thorlabs). SMF-28e+; Wavelength 1260-1625 nm; Connectors FC/PC; Bend loss < 0.1 dB.
XYZ Motorized linear translation stages MTS50-Z8 (Thorlabs) mounted in 3-axis XYZ configuration. Travel range 50mm; repeatability 1.6 μm; Minimal achievable incremental movement 0.05 μm; Minimal repeatable incremental movement 0.8 μm.
Data acquisition card PCI-6229 (National Instruments). Resolution 16 bits; Sample rate 250kS/s; 32 channels.
Illumination KL1500LCD (Leica Schott) portable fiber optics lamp.

6.4 Acoustic characterization setup

In this section we describe the setup used to characterize the sensitivity (in terms of noise equivalent pressure), the acoustic detection bandwidth, and the directivity of the sensors. The ultrasound was generated by the optoacoustic effect and the size and intensity of the ultrasonic source were modified by changing the absorbing material and the optical fluence of the excitation laser.

Acoustic characterization of the sensor was performed using the setup depicted in **Fig. 6.14**. List of equipment used to construct this setup can be found in **Table 6.2**. **Fig. 6.14a** depicts the general schematic of the setup. The sensor is connected to a CW tunable laser ('Laser 2') that pumps light to the sensor through a single-mode polarization-maintaining fiber. The wavelength is tuned off-resonance to the point of the maximum slope to increase the sensitivity of the sensor (**Section 2.3**). The reflected intensity from the sensor carrying the ultrasound induced modulations is diverted to a photodetector ('PD') using a fiber circulator ('CR'), the signal from the photodetector is recorded with a digitizer (not showed in the figure). Ultrasound waves are excited using a pulsed laser ('Laser1'), the beam laser is resized by a telescopic system (lenses 'L1' and 'L2') and spatially filtered with a pinhole ('PH'). The ultrasound point source is created by placing an absorber on the microscope cover slip ('CS') located under the sensor and adjusting the height of the microscope objective ('OBJ') so the optical focal spot coincides with the absorbers. Alignment and scanning of the sensor relative to the ultrasound source was realized using linear translation stages (not showed in the figure). **Fig. 6.14b** shows a photograph of the sensor mounted in the characterization system on top of the absorber. The sensor is still mounted to a holder that was used for connectorization of the chip with a vertical fiber array (**Fig. 6.10**), the holder is attached to 3-axis scanning stages trough a 3D printed adapted (**Fig. 6.14b**, the white device). Under the sensor a sample made of the gold film is visible, the sample is mounted on a 2-axis linear translation stage ('*xy* stages') and acoustically coupled to the sensor with few drops of water. Before measurements the sensor is lowered so it is contact with the water.

The sensitivity of the sensors was determined using vinyl black tape 125 µm thick (Type 764, 3M; Neuss, Germany) as an optical absorber illuminated by an average optical power of 0.64 mW. The tape was glued to a microscope coverslip of 150 µm thickness and a 0.5-mm needle hydrophone (Precision Acoustics; Dorchester, UK) was used for calibration of the acoustic source. The spectral response of the needle is approximately constant in the frequency band of [5, 30] MHz and is equal

to 450 mV/MPa. The signals emitted from the tape and detected by the sensors were recorded without averaging and passed through a [5, 30] MHz band pass filter to spectrally match it with the needle hydrophone for noise equivalent pressure calibration (see **Appendix B** for details).

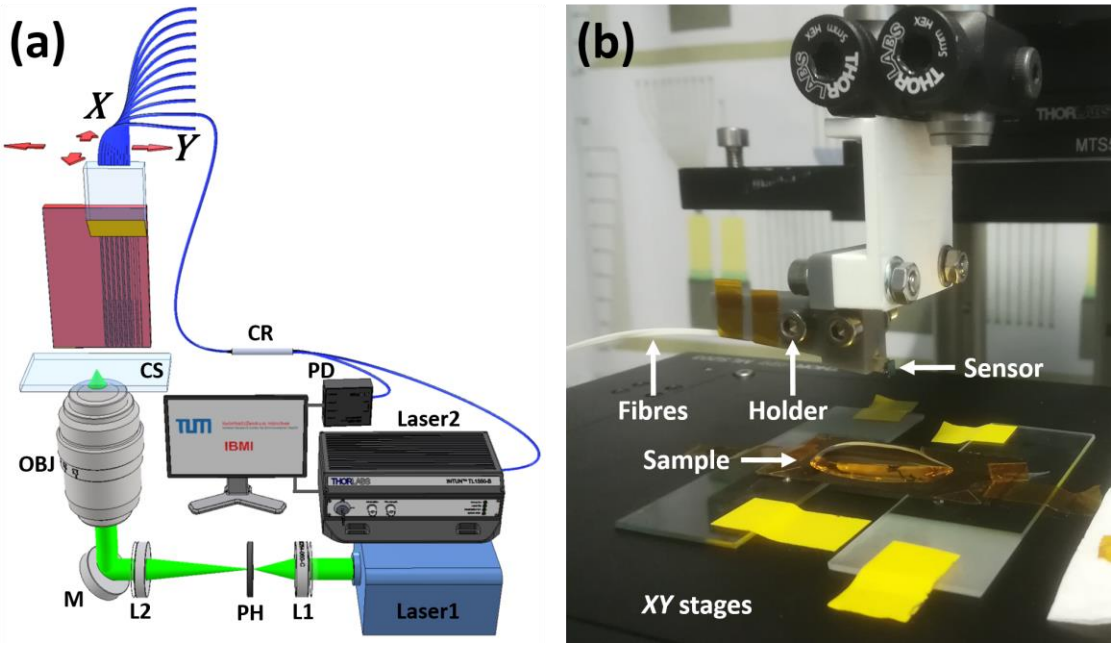

Figure 6.14. Acoustic characterization setup. **(a)** General schematic and principle of operation: Laser1, 515 nm pulsed laser for the excitation of ultrasonic signals; Laser2, tuneable CW laser in the C-band for the interrogation of the sensor; PD, photodiode; CR, fiber circulator; CS, microscope coverslip; OBJ, microscope objective; M, mirror; PH, pinhole; L1 and L2, telescope lenses. **(b)** photograph of the sensor mounted in a holder on top of a sample.

For characterisation of sensors' bandwidth, a thin gold film (200 nm) was sputtered onto a microscope coverslip in order to serve as optical absorber and ultra-broad acoustic frequency source [111]. The gold film was illuminated by average optical power of 0.1mW. The signals emitted from the old film and detected by the sensors were recorded and passed through a bandpass filter of [2, 500] MHz. The signals were averaged 1×10^3 times in order to compensate for the extremely weak signals generated from the point.

Table 6.2: List of equipment for acoustic characterization

CW Tunable laser TL1550-B-INTUN-PM (Thorlabs). Wavelength span 1519-1630 nm (C band); Optical power 20 mW; Effective linewidth 1.5 MHz; Wavelength repeatability 10 pm; Wavelength resolution 0.5pm.
Pulsed laser Flare PQ HP GR 2k-500 (Innolight, Germany). Wavelength 515 nm; Repetition rate 1.2 KHz; Pulse width 1.2 nm;
Photodetector PDB480C-AC (Thorlabs). Wavelength 1200 -1700 nm; Bandwidth 30 KHz – 1.6 GhZ; Transimpedance gain 16 x 10^3 V/A.
Fibre circulator CIR1550PM-APC (Thorlabs). Polarization maintaining single mode; Wavelength span 1520-1580 nm.
Telescope lenses Pair or lenses producing magnification of 5.
Pinhole P25C (Thorlabs). High power; 25 μm diameter.
Microscope objective PLN 10× (Olympus). NA = 0.25; Working distance 10.6 mm; Focal length 14 mm; Field of view 2.2 mm.
XYZ Motorized linear translation stages (Sensor) MTS50-Z8 (Thorlabs) mounted in 3-axis XYZ configuration. Travel range 50mm; repeatability 1.6 μm; Minimal achievable incremental movement 0.05 μm; Minimal repeatable incremental movement 0.8 μm.
XY Motorized linear translation stages (Sample) MLS203-1 (Thorlabs). Travel range 110 mm × 75 mm; repeatability 0.25 μm; Minimal achievable incremental movement 0.1 μm.
Data acquisition card CSE123G2 (GaGe , USA). Resolution 12 bits; Sample rate 6GS/s; 2 channels.

6.5 Imaging setup

In this section we describe the setup used for optoacoustic tomography with planar configuration. The major difference between this setup and the setup in **Section 6.4** is that the sample illumination is performed from the same side of the plane as ultrasound sensing (epi-illumination). The sensor interrogation and signal recording parts of the systems are identical.

Optoacoustic epi-illumination tomography was performed using the setup depicted in **Fig. 6.15**. List of equipment used to construct this setup can be found in **Table 6.3**. **Fig.** The interrogation of the sensor and recording of the ultrasonic signals is performed as described in **Section 6.4**. Ultrasound waves are excited using a pulsed laser ('Laser1') coupled to a multi-mode illumination fiber using a collimator ('COL'). The other end of the fiber is cleaved and the beam leaving it forms a spot on the sample plane. The sensor holder is attached to a manual goniometer stage above the sample plane that can adjust the angle of the sensor relative to the plane (θ). Alignment and scanning of the sensor relative to the ultrasound source was realized using linear translation stages (not showed in the figure). Acoustic coupling of the samples to the sensor is done with few drops of water.

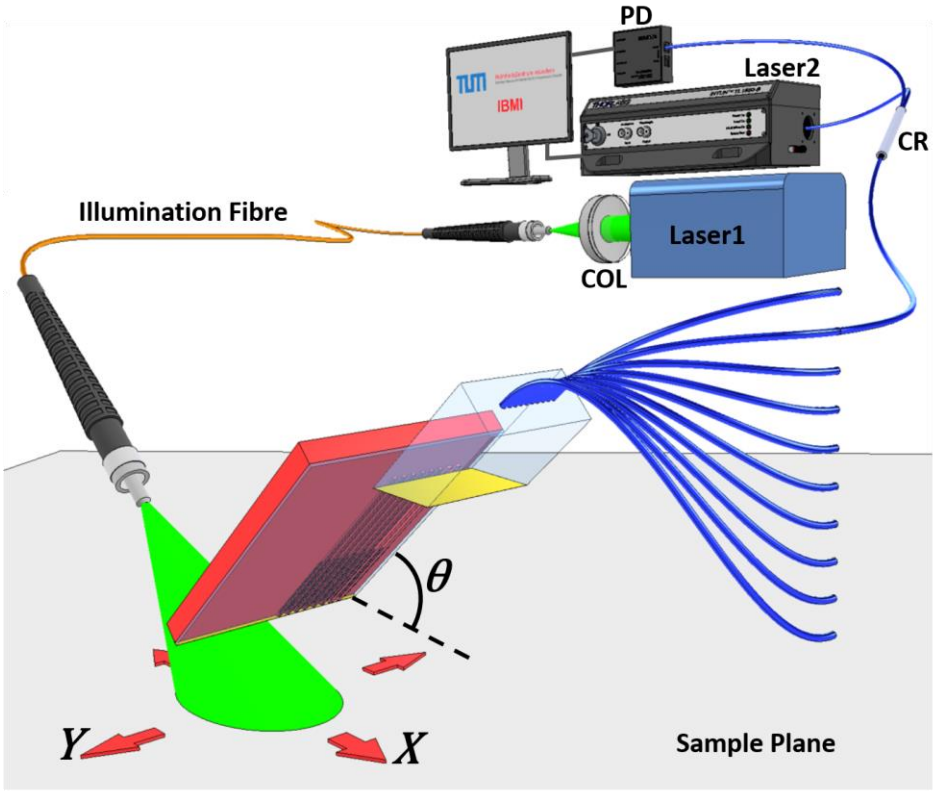

Figure 6.15. General schematic of an optoacoustic epi-illumination tomography setup. Laser1, 515 nm pulsed laser for the excitation of ultrasonic signals; Laser2, tuneable CW laser in the C-band for the interrogation of the sensor; PD, photodiode; CR, fiber circulator; COL, Fiber collimator.

Before imaging the sensor is centered over the illumination spot by acquiring B-scans of a black vinyl black 125 µm thick (Type 764, 3M; Neuss, Germany) and determining the coordinates of the

spot's center. Then the tape is removed and the phantoms are placed on the sample plane. Imaging of the phantoms was performed by linearly translating the sample plane while the sensor remains stationary relative to the fiber. During imaging the excitation laser was diffracted to a spot of ~1 mm in diameter and the average optical power was set to 3.2 mW. Image reconstruction is performed using the back-projection algorithm (see **Section 2.2**).

Table 6.3: List of equipment for epi-illumination imaging

CW Tunable laser TL1550-B-INTUN-PM (Thorlabs). Wavelength span 1519-1630 nm (C band); Optical power 20 mW; Effective linewidth 1.5 MHz; Wavelength repeatability 10 pm; Wavelength resolution 0.5pm.
Pulsed laser Flare PQ HP GR 2k-500 (Innolight, Germany). Wavelength 515nm; Repetition rate 1.2 KHz; Pulse width 1.2 nm;
Photodetector PDB480C-AC (Thorlabs). Wavelength 1200 -1700 nm; Bandwidth 30 KHz – 1.6 GhZ; Transimpedance gain 16 x 10^3 V/A.
Fibre circulator CIR1550PM-APC (Thorlabs). Polarization maintaining single mode; Wavelength span 1520-1580 nm.
Fibre collimator F810SMA-543 (Thorlabs). NA = 0.26; f = 34.74 mm.
Ilumination fibre M92L02 (Thorlabs). NA 0.22; core diameter 200 μm.
XYZ Motorized linear translation stages (Sensor) MTS50-Z8 (Thorlabs) mounted in 3-axis XYZ configuration. Travel range 50mm; repeatability 1.6 μm; Minimal achievable incremental movement 0.05 μm; Minimal repeatable incremental movement 0.8 μm.
XY Motorized linear translation stages (Sample) MLS203-1 (Thorlabs). Travel range 110 mm × 75 mm; repeatability 0.25 μm; Minimal achievable incremental movement 0.1 μm.
Goniometer stage GNL10 (Thorlabs)
Data acquisition card CSE123G2 (GaGe , USA). Resolution 12 bits; Sample rate 6GS/s; 2 channels.

7. Conclusive remarks and outlook

During this work we designed, build, and characterized several novel optical ultrasound sensors. We demonstrated how the silicon photonics platform can be used to miniaturize the sensors. We showed that traditional resonator designs like the π-phase shifted Bragg grating achieve miniaturization of only ~4.5 –fold when copied from the silica to the silicon platform. In order to take the full advantage of the strong light confinement in the silicon platform we developed a new sensor that exploits the sub-micron cross-section of a silicon waveguide as the aperture for ultrasound detection. The silicon waveguide-etalon detector (SWED) achieved drastic aperture miniaturization of 200 –fold over a π-phase shifted Bragg grating implemented in the silicon photonics platform.

The SWED was used to improve the resolution of raster-scan optoacoustic microscopy demonstrating 16 µm lateral and 5 µm axial resolutions which is 2 - and 6 -fold better that that achieved with state-of-the-art focused piezoelectric sensors. The sub-micron aperture of the SWED was used to develop a new imaging modality, the near-field scanning optoacoustic microscopy (NSOAM) offering absorption contrast with λ/50 acoustic super-resolution. This resolution (650 nm) is close to the resolution achieved with high-end optical microscopes. Considering the low cost of the SWED, NSOAM can be a lensless and alternative to optical and optoaocustic microscopy.

Future work and development of the sensor would focus on the following topics:

Sensitivity

The sensitivity per-area of the SWED is 10^8 –fold higher than for piezoelectric sensors but the absolute sensitivity is 9 mPa/Hz$^{1/2}$ (**chapter 4.4**) which is 45 –fold lower than of a focused

ultrasound sensor utilized in clinical RSOM (**Table 2.1**), note that this figure would be lower if the calibration bandwidth is take into account. In order for the SWED to be successfully implemented in clinical RSOM the sensitivity has to be improved. This can be done by increasing the Q-factor of the SWED, which can be achieved with stronger reflectivity of the Bragg grating and the reflective coating. Q-factor will also increase when with reduction of optical losses by smoothing side-wall roughness[63] and using rib waveguide geometries[66]. Acoustical matching between the impedances of silicon (~20 MRayls) and biological samples (~1.4 MRayls) by application of thin layers will also improve sensitivity.

Improving image quality

In addition to longitudinal surface acoustic waves the SWED also detects surface acoustic waves that propagate at the water-silicon interface with higher velocities than the longitudinal waves. During image reconstructions those waves reconstruct as artefacts around the object which blur the object and reduce image resolution. By characterising the total impulse response of the SWED, in a similar manner described in **Fig. 4.5**, and deconvolving it from the image the resolution can be substantially improved [100].

Multiplexing

Large-scale array multiplexing is challenging for optical resonator-based devices. One of the challenges of many photonic platforms is the strong dependence of the resonance on device size. The latter cannot be precisely controlled due to process-dependent variations[71], challenging the interrogation of large number of resonators with a single CW laser. The SOI platform also offers advantages over other photonic approaches, which may lead to practical solutions for multiplexing. On-chip photodetectors[54] and tunable Mach-Zander interferometers[34], that are fully compatible with the SWED manufacturing process, can be placed alongside the SWEDs and significantly reduce the costs of multiplexing when using pulse interferometry[112]. The intra-chip uniformity of the SOI platform[109] and the large integration density of the SWEDs, compared for example to polymer-based platforms, can also be exploited to reduce resonance wavelength

variability and laser tuning requirements, enabling multiplexing of several tens of SWEDs with a single CW-laser.

Implementations in other platforms

The SWED design can be easily copied to the fiber platform. There the diameter of the fiber core would determine the resolution lateral resolution. A typical core dimeter of a single mode fiber is 4 – 10 μm which can be a cheap, lower resolution, single sensor alternative to the SWED. Other platforms like the SiN (lower propagation losses) or hybrid silicon-polymer platforms (large photo-elastic constants) can be explored for increasing SWED sensitivity.

New applications

The biggest advantage of the SWED over focused piezoelectric transducers is the low footprint which makes it ideal for endoscopic and intravascular applications. Future interesting combination of SWEDs with SOI-based integrated bio-sensors [36] or on-chip microscopes [113], could lead to new clinical applications.

Appendix A: Critical dimension uniformity

The resonance frequency of any microfabricated resonator is highly dependent on the critical dimensions of the waveguides (width, thickness, side wall angle, etc.) which are difficult to control [71]. This is in particular a big issue with polymer mirroring sensors that are manufactured by imprint lithography (contact imprint) [24] as often critical dimension distortion occurs during mold separation process [114]. Critical dimensions uniformity is also a challenge with silicon waveguides mainly due to thickness variations along the wafer and etch-depth nonuniformities [71]. Those effects might be weaker within the same chip when the resonators are placed close to each other. Adjacent Silicon track-ring resonators with width of 10 µm, manufactured with the same standard high-volume CMOS fabrication tools as the SWEDs, were demonstrated to experience resonance shifts as low as 20pm for 25µm spacing [109]. Currently, as all the SWEDs on a single chip have different corrugation depth by design, their resonances cannot overlap. Yet we can calculate the inter-reticle resonance shift and extrapolate the result. **Fig. A.1a** shows the 200 mm SOI wafer used for the SWED manufacturing, it contains 64 chips. Each with 8 π-phase-shifted waveguide Bragg gratings (π-WBG) resonators that were characterized. The location of the pre-polished chips relative to the reticles are indicated on the figure. The resonance wavelengths of the π-WBGs with corrugation depth of 40nm were measured across the whole wafer, and the process-dependent resonance shifts were calculated between pairs of neighboring reticles. **Fig. A.1b** and **Fig. A.1c** respectively show the maps of the inter-reticle resonance shift (nm) along the rows and columns of **Fig. A.1a**. The box plots of those maps (**Fig. A.1d**) shows a median of 1.63 nm along the rows and a median of 1.03 nm along the columns, by extrapolating this trend we can expect intra-chip resonance shifts of 1.6 pm / 25 µm and 1.9 pm / 25 µm which are an order of magnitude smaller than the results for the 10 µm silicon track-ring resonators [109]. The outlines in **Fig. A.1d** are indicated by red dots, their corresponding locations on the maps are indicated by red rectangles, as expected the location of the outliners is at the wafer edge due to process non-uniformity at this location.

Currently with π-WBG resonance FWHM of ~100pm, resonance shifts of 20 pm / 25 µm are tolerable. This opens the door for the possibility of using a low-cost CW laser to multiplex 25 π-WBGs or SWEDs (with 1 µm spacing) with uniformity estimation of [109]. This uniformity and the

number of SWEDs multiplexed by a single CW laser can be further improved by wafer post-processing with electron beam lithography [115] or thermal tuning [116], both are fully compatible with SWED manufacturing process.

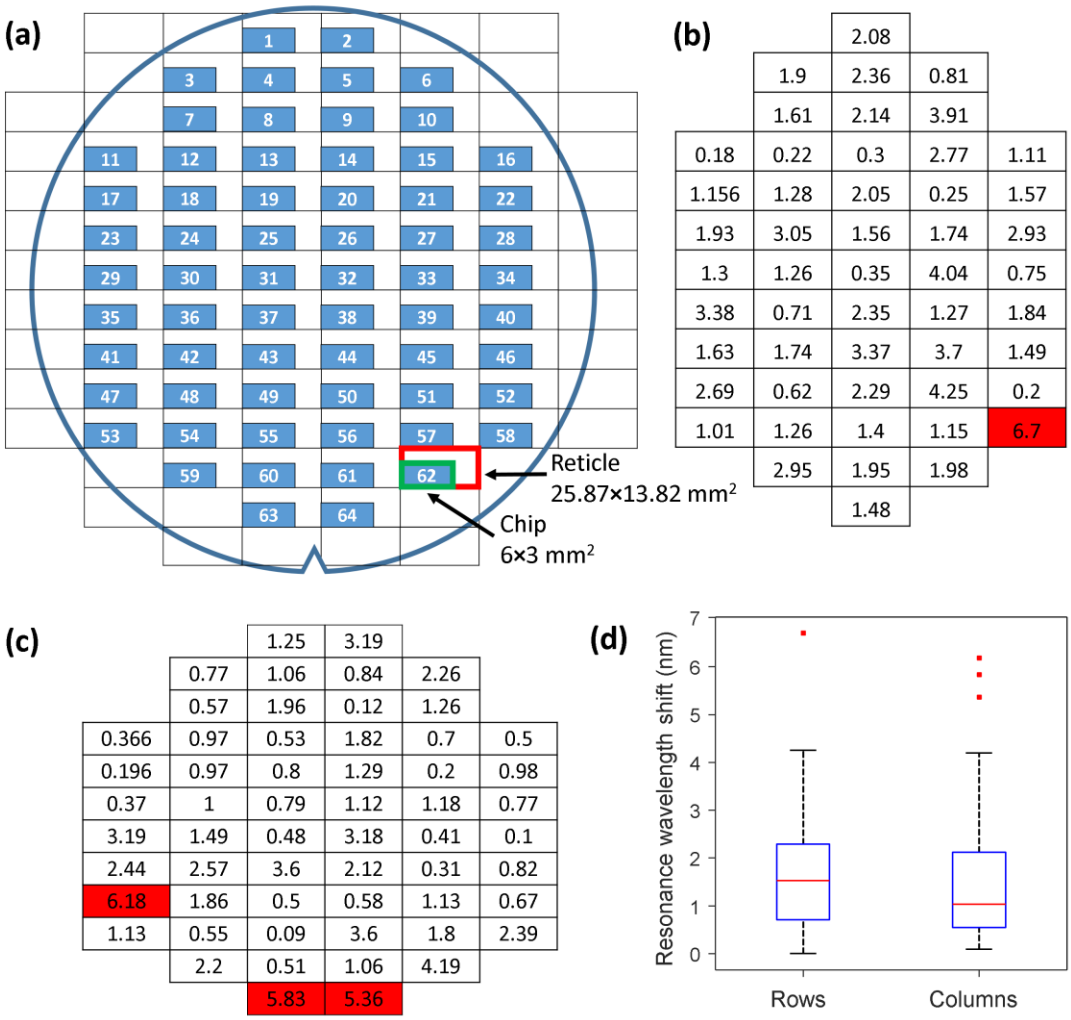

Figure A.1. Optical resonance uniformity across a 200 mm SOI wafer. **(a)** Location of the pre-polished chips that are the basis for the SWEDs on the SOI wafer relative to the reticle. **(b)** Optical resonance wavelength shift (nm) map of the resonators with corrugation depth of 40nm relative to the same resonator on a neighboring reticle along the rows. **(c)** Optical resonance wavelength shift (nm) map of the resonators with corrugation depth of 40nm relative to the same resonator on a neighboring reticle along the columns. **(d)** Box plot of the optical resonance wavelength shifts in (b) and (c). Outliners are indicated by red dots in (d) and their respective locations on the wafer are indicated by red rectangles in (b) and (c).

Appendix B: Extrapolation of noise equivalent pressure

The needle hydrophone employed for the source calibration in this work has an approximately constant spectral response in the frequency band of [5, 30] MHz. Because calibrated ultrasound transducers in higher frequencies and wider frequency bands are not available the noise equivalent pressure (NEP) of the SWED in higher frequency bands has to be extrapolated. We divide the large bandwidth of the SWED into smaller sections of the same width equal to the calibrated band of the hydrophone (25 MHz). The NEP in each frequency band can be written as:

$$NEP_i = N_i/S_i \cdot P_i \tag{B.1}$$

Where *i* is the index indicating the frequency band, N_i is the noise in band *i*, S_i is the signal in band *i*, and P_i is the acoustic pressure in band *i*. If band *i* overlaps with the frequency response of a calibrated transducer NEP_i can be measured. In order to calculate the NEP of the SWED in a different frequency band *j* we make two assumptions:

1. $N_i \approx N_j$
2. $P_i \approx P_j$

Then NEP_j can be extracted from:

$$NEP_i/NEP_j \approx S_j/S_i \tag{B.2}$$

The assumptions holds true particularly for the point source used in this work for bandwidth characterization[117]. Applying a band pass filter to the signal recorded by SWED1 in **Fig. 4.9a** we get: $NEP_{[5,30]MHz} = 2.1 \cdot NEP_{[24.5,49.5]MHz}$. This result means that if a source would emit the same amount of pressure first in the [5, 30] MHz band and then in the [25.5, 49.5] MHz band the SWEDs response would be stronger by a factor of 2.1 in the latter case.

Appendix C: Point spread functions

Optical point spread function

The confocal microscope used in this work was Olympus IX-83 (Olympus, Japan) with UPLSAPO60XW 1.2 NA water immersion objective (Olympus, Japan). The point spread function (PSF) of the confocal microscope (**Fig. 5.3b**) was obtained by raster scanning and collecting the reflected light from a single 150 nm gold nanoparticle (part no. 746649, Sigma Aldrich, USA) immobilized on 170 um coverglass (No. 1.5H, Paul Marienfeld GmbH, Germany) using a layer of poly-l-lysine (part no. P8920-100ML, Sigma Aldrich, USA). The nanoparticle was illuminated by a pulsed laser with a wavelength of 485 nm (LDH-D-C-485, PicoQuant, Berlin, Germany) driven by a corresponding driver (PDL 800-D, PicoQuant, Berlin, Germany), collimated and then coupled to the side port of the confocal microscope. The reflected light was separated from the illumination light using a 2 µm thin pellicle beamsplitter (BP108, Thorlabs, USA) and redirected towards a PMT module (H10723-01, Hamamatsu Photonics, Japan). The voltage signal from the PMT was digitalized by a DAQ card (PCIe-6353, National Instruments, USA) and the raster scanning was performed with scanning mirrors (dynAXIS 421, ScanLab GmbH, Munich, Germany).

Acoustic point spread function

In order to estimate the acoustic PSD of the SWED the following procedure was performed: The optical edge spread function (ESF) of a straight edge on a 1951 USAF resolution test target (Edmond Optics; Barrington, USA) and optical PSF were acquired with the confocal microscope with pixel size of 50 nm and 10nm respectively, and the acoustic ESF was acquired with SWED4 in the near-field with pixel size of 200 nm. The optical ESF and the acoustic ESF were interpolated to match the sampling rate of the optical PSF, then the optical PSF was deconvoluted from the optical ESF using the Richardson-Lucy algorithm with 10 iterations to obtain the true edge profile of the target sample. The profile and the acoustic ESF were normalized and their slopes were linearly fitted with $R2 > 0.92$, then the profile was deconvoluted from the acoustic ESF using the Richardson-Lucy algorithm with 10 iterations to obtain an estimate of the acoustic PSF (**Fig. 5.3b**).

Publications and patents

Patents submitted related to this work:

R. Shnaiderman, V. Ntziachristos, and G. Wissmeyer, *Sensor for tissue measurements*. Patent application no. EP 18 16 0940.5, 2018.

R. Shnaiderman, G. Wissmeyer, and V. Ntziachristos. *Sensor comprising a waveguide with optical resonator and sensing method*. Patent application no. EP 18 16 0946.2, 2018.

Journal publications related to this work:

Rami Shnaiderman, Qutaiba Mustafa, Okan Ülgen, Georg Wissmeyer, Okan Ülgen, Hector Estrada, Daniel Razansky, Andriy Chmyrov, Vasilis Ntziachristos, *Silicon-photonics point sensor for high-resolution optoacoustic imaging*, **Advanced Optical Materials** 2100256 (2021).

Okan Ülgen, **Rami Shnaiderman**, Christian Zakian, Vasilis Ntziachristos, *Interferometric optical fiber sensor for optoacoustic endomicroscopy*, **Journal of Biophotonics** e202000501 (2021).

Wouter J Westerveld, Md Mahmud-Ul-Hasan, **Rami Shnaiderman**, Vasilis Ntziachristos, Xavier Rottenberg, Simone Severi, Veronique Rochus, *Sensitive, small, broadband and scalable optomechanical ultrasound sensor in silicon photonics*, **Nature Photonics** 15 (5), 341-345 (2021).

Rami Shnaiderman, Georg Wissmeyer, Okan Ülgen, Qutaiba Mustafa, Andriy Chmyrov, Vasilis Ntziachristos, *A submicrometre silicon-on-insulator resonator for ultrasound detection*, **Nature** 585, 372–378 (2020).

Rami Shnaiderman, Georg Wissmeyer, Markus Seeger, Dominik Soliman, Hector Estrada, Daniel Razansky, Amir Rosenthal, and Vasilis Ntziachristos, *Fiber interferometer for hybrid optical and optoacoustic intravital microscopy*, **Optica** 4, 1180-1187 (2017).

Georg Wissmeyer, Dominik Soliman, **Rami Shnaiderman**, Amir Rosenthal, and Vasilis Ntziachristos**,** *All-optical optoacoustic microscope based on wideband pulse interferometry*, **Optics Letters** 41, 1953-1956 (2016).

Conference papers related to this work:

Rami Shnaiderman, Georg Wissmeyer, Héctor Estrada, Daniel Razansky, Qutaiba Mustafa, Andriy Chmyrov, and Vasilis Ntziachristos, *Ultrasound point detectors in the silicon photonics platform for high frequency optoacoustic tomography (Conference Presentation)*, Proc. SPIE 10878, Photons Plus Ultrasound: Imaging and Sensing 2019, 108780P (4 March 2019);

R. Shnaiderman, G. Wissmeyer, H. Estrada, M. Seeger, and V. Ntziachristos, *Intravital hybrid optical-optoacoustic microscopy based on fiber-Bragg interferometry*, in Proc. SPIE 10494, p. 104942M (2018).

G. Wissmeyer*, **R. Shnaiderman***, D. Soliman, and V. Ntziachristos, *Optoacoustic microscopy based on pi-FBG ultrasound sensors*, in Proc. SPIE10064, p. 1006423 (2017).

Conference talks related to this work:

Rami Shnaiderman, Georg Wissmeyer, Héctor Estrada, Daniel Razansky, Qutaiba Mustafa, Andriy Chmyrov, Vasilis Ntziachristos, *Ultrasound point detectors in the silicon photonics platform for optoacoustic imaging* (conference talk), European Conferences on Biomedical Optics, Opto-Acoustic Methods and Applications in Biophotonics, Novel Detectors and Systems I, 24 Jun 2019, Munich, Germany.

Rami Shnaiderman, Georg Wissmeyer, Héctor Estrada, Daniel Razansky, Qutaiba Mustafa, Andriy Chmyrov, Vasilis Ntziachristos, *Ultrasound point detectors in the silicon photonics platform for high frequency optoacoustic tomography (Conference Presentation)*, Proceedings Volume 10878, Photons Plus Ultrasound: Imaging and Sensing 2019; 108780P (2019), San-Francisco, USA.

Rami Shnaiderman, Georg Wissmeyer, Markus Seeger, Hector Estrada, Vasilis Ntziachristos, *Intravital hybrid optical-optoacoustic microscopy based on fiber-Bragg interferometry*, Proceedings Volume 10494, Photons Plus Ultrasound: Imaging and Sensing 2018; 104942M (2018), San-Francisco, USA.

Rami Shnaiderman, *Intravital hybrid optical-optoacoustic microscopy*, Spring school for advanced imaging in biological research, March 15-16, 2017, Weizmann institute of science, Israel.

Reprint permissions

Parts of this work have been published in peer-review journals or are currently in the process of submission. These elements were included in this thesis as granted through the author rights in the copyright transfer agreements of the respective publishing journals. Specifically, the figures in chapters 4 and 5 were adapted from [118].

Reprints:

Chapter 2, Figure 2.1: taken from [14]. Permission provided by Dr. Murad Omar, via email.

References

[1] V. Ntziachristos, “Going deeper than microscopy : the optical imaging frontier in biology,” *Nat. Methods*, vol. 7, no. 8, pp. 603–614, 2010, doi: 10.1038/nmeth.1483.

[2] A. Taruttis and V. Ntziachristos, “Advances in real-time multispectral optoacoustic imaging and its applications,” *Nat. Photonics*, vol. 9, no. April, pp. 219–227, 2015, doi: 10.1038/nphoton.2015.29.

[3] M. Omar, J. Aguirre, and V. Ntziachristos, “Optoacoustic mesoscopy for biomedicine,” *Nat. Biomed. Eng.*, vol. 3, no. 5, pp. 354–370, 2019, doi: 10.1038/s41551-019-0377-4.

[4] J. Aguirre *et al.*, “Precision assessment of label-free psoriasis biomarkers with ultra-broadband optoacoustic mesoscopy,” *Nat. Biomed. Eng.*, vol. 1, no. 5, p. 0068, May 2017, doi: 10.1038/s41551-017-0068.

[5] K. Haedicke *et al.*, “High-resolution optoacoustic imaging of tissue responses to vascular-targeted therapies,” *Nat. Biomed. Eng.*, vol. 4, no. 3, pp. 286–297, Mar. 2020, doi: 10.1038/s41551-020-0527-8.

[6] A. Liu *et al.*, “A high-speed silicon optical modulator based on a metal-oxide-semiconductor capacitor,” *Nature*, vol. 427, no. 6975, pp. 615–618, 2004, doi: 10.1038/nature02310.

[7] Z. Zhou, B. Yin, and J. Michel, “On-chip light sources for silicon photonics,” *Light Sci. Appl.*, vol. 4, no. 11, pp. 1–13, 2015, doi: 10.1038/lsa.2015.131.

[8] L. V Wang, *Photoacoustic Imaging and Spectroscopy*. CRC Press, 2009.

[9] L. V. Wang, “Photoacoustic microscopy and computed tomography,” *Biomed. Opt. BIOMED 2008*, vol. 14, no. 1, pp. 171–179, 2008, doi: 10.1364/biomed.2008.bma1.

[10] J. Yao and L. V. Wang, “Sensitivity of photoacoustic microscopy,” *Photoacoustics*, vol. 2, no. 2, pp. 87–101, 2014, doi: 10.1016/j.pacs.2014.04.002.

[11] E. V. Savateeva, A. A. Karabutov, S. V. Solomatin, and A. A. Oraevsky, “Optical properties of blood at various levels of oxygenation studied by time-resolved detection of laser-induced pressure profiles,” in *Proc. SPIE , , Biomedical Optoacoustics III*, Jun. 2002, vol. 4618, pp. 63–75, doi: 10.1117/12.469849.

[12] X. L. Deán-Ben, D. Razansky, and V. Ntziachristos, “The effects of acoustic attenuation in optoacoustic signals.,” *Phys. Med. Biol.*, vol. 56, no. 18, pp. 6129–48, 2011, doi: 10.1088/0031-9155/56/18/021.

[13] G. J. Diebold, T. Sun, and M. I. Khan, “Photoacoustic monopole radiation in one, two, and three dimensions,” *Phys. Rev. Lett.*, vol. 67, no. 24, pp. 3384–3387, Dec. 1991, doi: 10.1103/PhysRevLett.67.3384.

[14] M. d A. Omar, “Multi-scale thermoacoustic imaging methods of biological tissues,” Technical university Munich, 2015.

[15] Y. Xu, D. Feng, and L. V Wang, “Exact Frequency-Domain Reconstruction for Thermoacoustic Tomography—I: Planar Geometry,” *Ieee*, vol. 21, no. 7, pp. 823–828, 2002, doi:

10.1109/TMI.2002.801172.

[16] M. Xu and L. V. Wang, “Universal back-projection algorithm for photoacoustic computed tomography,” *Phys. Rev. E - Stat. Nonlinear, Soft Matter Phys.*, vol. 71, no. 1, pp. 1–7, 2005, doi: 10.1103/PhysRevE.71.016706.

[17] M. Xu and L. V. Wang, “Analytic explanation of spatial resolution related to bandwidth and detector aperture size in thermoacoustic or photoacoustic reconstruction,” *Phys. Rev. E - Stat. Physics, Plasmas, Fluids, Relat. Interdiscip. Top.*, vol. 67, no. 5, p. 15, 2003, doi: 10.1103/PhysRevE.67.056605.

[18] M.-L. Li, H. E. Zhang, K. Maslov, G. Stoica, and L. V Wang, “Improved in vivo photoacoustic microscopy based on a virtual-detector concept.,” *Opt. Lett.*, vol. 31, no. 4, pp. 474–476, 2006, doi: 10.1364/OL.31.000474.

[19] L. V. W. Junjie Yao, “Photoacoustic microscopy,” *Laser Photonics Rev.*, vol. 1, no. 21, 2012, doi: 10.1002/lpor.201200060.

[20] A. A. Vives, *Piezoelectric transducers and applications*. 2008.

[21] J. Zhu, “OPTIMIZATION OF MATCHING LAYER DESIGN FOR MEDICAL ULTRASONIC TRANSDUCER,” The Pennsylvania State University, 2008.

[22] B. T. Khuri-Yakub and Ö. Oralkan, “Capacitive micromachined ultrasonic transducers for medical imaging and therapy,” *J. Micromechanics Microengineering*, vol. 21, no. 5, pp. 54004–54014, 2011, doi: 10.1088/0960-1317/21/5/054004.

[23] G. Wissmeyer, M. A. Pleitez, A. Rosenthal, and V. Ntziachristos, “Looking at sound: optoacoustics with all-optical ultrasound detection,” *Light Sci. Appl.*, vol. 7, no. 1, p. 53, Dec. 2018, doi: 10.1038/s41377-018-0036-7.

[24] C. Zhang, S. L. Chen, T. Ling, and L. J. Guo, “Review of imprinted polymer microrings as ultrasound detectors: Design, fabrication, and characterization,” *IEEE Sens. J.*, vol. 15, no. 6, pp. 3241–3248, 2015, doi: 10.1109/JSEN.2015.2421519.

[25] H. Li, B. Dong, Z. Zhang, H. F. Zhang, and C. Sun, “A transparent broadband ultrasonic detector based on an optical micro-ring resonator for photoacoustic microscopy.,” *Sci. Rep.*, vol. 4, p. 4496, 2014, doi: 10.1038/srep04496.

[26] B. Dong *et al.*, “Isometric multimodal photoacoustic microscopy based on optically transparent micro-ring ultrasonic detection,” *Optica*, vol. 2, no. 2, p. 169, Feb. 2015, doi: 10.1364/OPTICA.2.000169.

[27] B. Dong, S. Chen, Z. Zhang, C. Sun, and H. F. Zhang, “Photoacoustic probe using a microring resonator ultrasonic sensor for endoscopic applications,” *Opt. Lett.*, vol. 39, no. 15, p. 4372, 2014, doi: 10.1364/ol.39.004372.

[28] A. P. Jathoul *et al.*, “Deep in vivo photoacoustic imaging of mammalian tissues using a tyrosinase-based genetic reporter,” *Nat. Photonics*, vol. 9, no. April, pp. 239–246, 2015, doi: 10.1038/nphoton.2015.22.

[29] G. E. Moore, “Cramming more components onto integrated circuits,” *Proc. IEEE*, vol. 86, no. 1, pp. 82–85, 1998, doi: 10.1109/JPROC.1998.658762.

[30] G. T. Reed, *Silicon Photonics: The State of the Art*. John Wiley & Sons, 2008.

[31] L. Vivien and L. Pavesi, *Handbook of Silicon Photonics*. CRC Press, 2013.

[32] D. J. Lockwood and L. Pavesi, *Silicon Photonics II: Components and Integration*, vol. 119. 2011.

[33] A. N. Tait *et al.*, "Neuromorphic photonic networks using silicon photonic weight banks," *Sci. Rep.*, vol. 7, no. 1, pp. 1–10, 2017, doi: 10.1038/s41598-017-07754-z.

[34] Y. Shen *et al.*, "Deep learning with coherent nanophotonic circuits," *Nat. Photonics*, vol. 11, no. 7, pp. 441–446, Jul. 2017, doi: 10.1038/nphoton.2017.93.

[35] S. M. Turkane and A. K. Kureshi, "Emerging interconnects: a state-of-the-art review and emerging solutions," *Int. J. Electron.*, vol. 104, no. 7, pp. 1107–1119, 2017, doi: 10.1080/00207217.2017.1285436.

[36] S. Sang, Y. Wang, Q. Feng, Y. Wei, J. Ji, and W. Zhang, "Progress of new label-free techniques for biosensors: a review," *Crit. Rev. Biotechnol.*, vol. 36, no. 3, pp. 465–481, 2016, doi: 10.3109/07388551.2014.991270.

[37] P. Abgrall and A. M. Gué, "Lab-on-chip technologies: Making a microfluidic network and coupling it into a complete microsystem - A review," *J. Micromechanics Microengineering*, vol. 17, no. 5, 2007, doi: 10.1088/0960-1317/17/5/R01.

[38] W. Bogaerts and L. Chrostowski, "Silicon Photonics Circuit Design: Methods, Tools and Challenges," *Laser Photonics Rev.*, vol. 1700237, pp. 1–29, 2018, doi: 10.1002/lpor.201700237.

[39] P. Dumon, W. Bogaerts, A. Tchelnokov, J. Fedeli, and R. Baets, "Silicon Nanophotonics," *Futur. Fab Int.*, no. 25, pp. 29–36, 2008.

[40] C. Zemzemi, A. Zorgani, L. Daunizeau, S. Belabhar, R. Souchon, and S. Catheline, "Super-resolution limit of shear-wave elastography," *EPL (Europhysics Lett.*, vol. 129, no. 3, p. 34002, Mar. 2020, doi: 10.1209/0295-5075/129/34002.

[41] A. Rosenthal *et al.*, "Sensitive interferometric detection of ultrasound for minimally invasive clinical imaging applications," *Laser Photon. Rev.*, vol. 8, no. 3, pp. 450–457, May 2014, doi: 10.1002/lpor.201300204.

[42] C. E. Munding *et al.*, "Development of a 3 French Dual-Frequency Intravascular Ultrasound Catheter," *Ultrasound Med. Biol.*, vol. 44, no. 1, pp. 251–266, 2018, doi: 10.1016/j.ultrasmedbio.2017.09.015.

[43] P. Morris, A. Hurrell, A. Shaw, E. Zhang, and P. Beard, "A Fabry–Pérot fiber-optic ultrasonic hydrophone for the simultaneous measurement of temperature and acoustic pressure," *J. Acoust. Soc. Am.*, vol. 125, no. 6, pp. 3611–3622, Jun. 2009, doi: 10.1121/1.3117437.

[44] X. Chen *et al.*, "The Emergence of Silicon Photonics as a Flexible Technology Platform," *Proc. IEEE*, vol. 106, no. 12, pp. 2101–2116, 2018, doi: 10.1109/JPROC.2018.2854372.

[45] A. Marinins, *Polymer Components for Photonic Integrated Circuits*. 2017.

[46] R. Baets *et al.*, "Silicon photonics: Silicon nitride versus silicon-on-insulator," *2016 Opt. Fiber Commun. Conf. Exhib. OFC 2016*, pp. 3–5, 2016, doi: 10.1364/ofc.2016.th3j.1.

[47] T. Ling, S.-L. Chen, and L. J. Guo, "Fabrication and characterization of High Q polymer micro-ring resonator and its application as a sensitive ultrasonic detector," *Opt. Express*, vol. 19, no. 2, p. 861, Jan. 2011, doi: 10.1364/OE.19.000861.

[48] A. Rosenthal, D. Razansky, and V. Ntziachristos, “High-sensitivity compact ultrasonic detector based on a pi-phase-shifted fiber Bragg grating,” *Opt. Lett.*, vol. 36, no. 10, pp. 1833–1835, 2011.

[49] Y. A. Vlasov and S. J. McNab, “Losses in single-mode silicon-on-insulator strip waveguides and bends,” *Opt. Express*, vol. 12, no. 8, p. 1622, 2004, doi: 10.1364/OPEX.12.001622.

[50] T. Ling, S.-L. Chen, and L. J. Guo, “High-sensitivity and wide-directivity ultrasound detection using high Q polymer microring resonators.,” *Appl. Phys. Lett.*, vol. 98, no. 20, p. 204103, 2011, doi: 10.1063/1.3589971.

[51] R. Ravi Kumar, E. Hahamovich, S. Tsesses, Y. Hazan, A. Grinberg, and A. Rosenthal, “Enhanced Sensitivity of Silicon-Photonics-Based Ultrasound Detection via BCB Coating,” *IEEE Photonics J.*, vol. 11, no. 3, pp. 1–11, Jun. 2019, doi: 10.1109/JPHOT.2019.2908013.

[52] A. Rosenthal, M. Omar, H. Estrada, S. Kellnberger, D. Razansky, and V. Ntziachristos, “Embedded ultrasound sensor in a silicon-on-insulator photonic platform,” *Appl. Phys. Lett.*, vol. 104, no. 2, p. 021116, Jan. 2014, doi: 10.1063/1.4860983.

[53] S. M. Leinders *et al.*, “A sensitive optical micro-machined ultrasound sensor (OMUS) based on a silicon photonic ring resonator on an acoustical membrane.,” *Sci. Rep.*, vol. 5, no. August, p. 14328, 2015, doi: 10.1038/srep14328.

[54] J. Michel, J. Liu, and L. C. Kimerling, “High-performance Ge-on-Si photodetectors,” *Nat. Photonics*, vol. 4, no. 8, pp. 527–534, 2010, doi: 10.1038/nphoton.2010.157.

[55] A. W. Fang, H. Park, R. Jones, O. Cohen, M. J. Paniccia, and J. E. Bowers, “A continuous-wave hybrid AlGaInAs - Silicon evanescent laser,” *IEEE Photonics Technol. Lett.*, vol. 18, no. 10, pp. 1143–1145, 2006, doi: 10.1109/LPT.2006.874690.

[56] R. Won, “Integrating silicon photonics,” *Nat. Photonics*, vol. 4, no. 8, pp. 498–499, Aug. 2010, doi: 10.1038/nphoton.2010.189.

[57] J. V. Galan, “Addressing Fiber-to-Chip Photonics Jose Vicente Gal ´,” 2010.

[58] S. Pathak, “Silicon nano-photonics based arrayed waveguide gratings,” 2014.

[59] X. Wang, “Silicon Photonic Waveguide Bragg Gratings,” 2013.

[60] H. Nikkhah, “Optical Switch on a Chip: The Talbot Effect, Lüneburg Lenses & Metamaterials Hamdam,” 2013.

[61] A. B. Fallahkhair, K. S. Li, and T. E. Murphy, “Vector Finite Difference Modesolver for Anisotropic Dielectric Waveguides,” *J. Light. Technol.*, vol. 26, no. 11, pp. 1423–1431, Jun. 2008, doi: 10.1109/JLT.2008.923643.

[62] “Optical Eigenmode Solver for Dielectric Waveguides.” https://www.photonics.umd.edu/software/wgmodes/.

[63] F. Gao, Y. Wang, G. Cao, X. Jia, and F. Zhang, “Reduction of sidewall roughness in silicon-on-insulator rib waveguides,” *Appl. Surf. Sci.*, vol. 252, no. 14, pp. 5071–5075, 2006, doi: 10.1016/j.apsusc.2005.07.070.

[64] Y. Painchaud, M. Poulin, C. Latrasse, N. Ayotte, M.-J. Picard, and M. Morin, “Bragg grating notch filters in silicon-on-insulator waveguides,” *Adv. Photonics Congr.*, vol. 21, p. BW2E.3, 2012, doi: 10.1364/BGPP.2012.BW2E.3.

[65] S. Tsesses, D. Aronovich, A. Grinberg, E. Hahamovich, and A. Rosenthal, “Modeling the sensitivity dependence of silicon-photonics-based ultrasound detectors,” *Opt. Lett.*, vol. 42, no. 24, p. 5262, 2017, doi: 10.1364/OL.42.005262.

[66] W. Bogaerts and S. K. Selvaraja, “Compact single-mode silicon hybrid rib/strip waveguide with adiabatic bends,” *IEEE Photonics J.*, vol. 3, no. 3, pp. 422–432, 2011, doi: 10.1109/JPHOT.2011.2142931.

[67] X. Wang *et al.*, “A silicon photonic biosensor using phase-shifted Bragg gratings in slot waveguide,” *J. Biophotonics*, vol. 6, no. 10, pp. 821–828, 2013, doi: 10.1002/jbio.201300012.

[68] Y. Fu, T. Ye, W. Tang, and T. Chu, “Efficient adiabatic silicon-on-insulator waveguide taper,” *Photonics Res.*, vol. 2, no. 3, p. A41, 2014, doi: 10.1364/PRJ.2.000A41.

[69] K. Shiraishi, H. Yoda, A. Ohshima, H. Ikedo, and C. S. Tsai, *A silicon-based spot-size converter between single-mode fibers and Si-wire waveguides using cascaded tapers*, vol. 91, no. 14. 2007.

[70] F. Van Laere, W. Bogaerts, D. Taillaert, P. Dumon, D. Van Thourhout, and R. Baets, “Compact Focusing Grating Couplers Between Optical Fibers and Silicon-on-Insulator Photonic Wire Waveguides,” in *OFC/NFOEC 2007 - 2007 Conference on Optical Fiber Communication and the National Fiber Optic Engineers Conference*, Mar. 2007, pp. 1–3, doi: 10.1109/OFC.2007.4348869.

[71] A. V. Krishnamoorthy *et al.*, “Exploiting CMOS Manufacturing to Reduce Tuning Requirements for Resonant Optical Devices,” *IEEE Photonics J.*, vol. 3, no. 3, pp. 567–579, Jun. 2011, doi: 10.1109/JPHOT.2011.2140367.

[72] B. Snyder and P. O’Brien, “Packaging Process for Grating-Coupled Silicon Photonic Waveguides Using Angle-Polished Fibers,” *IEEE Trans. Components, Packag. Manuf. Technol.*, vol. 3, no. 6, pp. 954–959, Jun. 2013, doi: 10.1109/TCPMT.2012.2237052.

[73] X. Chen and H. K. Tsang, “Polarization-independent grating couplers for silicon-on-insulator nanophotonic waveguides,” *Opt. Lett.*, vol. 36, no. 6, p. 796, 2011, doi: 10.1364/ol.36.000796.

[74] X. Wei and S. M. Weiss, “Guided mode biosensor based on grating coupled porous silicon waveguide,” *Opt. Express*, vol. 19, no. 12, p. 11330, 2011, doi: 10.1364/oe.19.011330.

[75] V. Muniswamy, P. K. Pattnaik, and N. Krishnaswamy, “Modeling and analysis of SOI gratings-based opto-fluidic biosensor for lab-on-a-chip applications,” *Photonics*, vol. 6, no. 2, 2019, doi: 10.3390/PHOTONICS6020071.

[76] D.-X. Xu *et al.*, “Silicon photonic integration platform – Have we found the sweet spot?,” *IEEE J. Sel. Top. Quantum Electron.*, vol. 20, no. 4, pp. 1–1, 2014, doi: 10.1109/JSTQE.2014.2299634.

[77] X. Wang, W. Shi, H. Yun, S. Grist, N. a. F. Jaeger, and L. Chrostowski, “Narrow-band waveguide Bragg gratings on SOI wafers with CMOS-compatible fabrication process,” *Opt. Express*, vol. 20, no. 14, pp. 15547–15558, 2012, doi: 10.1364/OE.20.015547.

[78] X. Wang *et al.*, “Lithography simulation for the fabrication of silicon photonic devices with deep-ultraviolet lithography,” in *The 9th International Conference on Group IV Photonics (GFP)*, Aug. 2012, pp. 288–290, doi: 10.1109/GROUP4.2012.6324162.

[79] Y. Painchaud, M. Poulin, C. Latrasse, and M. J. Picard, “Bragg grating based Fabry-Perot filters for characterizing silicon-on-insulator waveguides,” in *IEEE International Conference on Group IV Photonics GFP*, 2012, vol. 5, no. 4, pp. 180–182, doi: 10.1109/GROUP4.2012.6324126.

[80] C. Klitis, G. Cantarella, M. J. Strain, and M. Sorel, “High-extinction-ratio TE/TM selective Bragg grating filters on silicon-on-insulator,” *Opt. Lett.*, vol. 42, no. 15, p. 3040, 2017, doi: 10.1364/OL.42.003040.

[81] D. T. H. Tan, K. Ikeda, and Y. Fainman, “Cladding-modulated Bragg gratings in silicon waveguides.,” *Opt. Lett.*, vol. 34, no. 9, pp. 1357–1359, 2009, doi: 10.1364/OL.34.001357.

[82] J.-L. Kou, M. Ding, J. Feng, Y.-Q. Lu, F. Xu, and G. Brambilla, “Microfiber-Based Bragg Gratings for Sensing Applications: A Review,” *Sensors*, vol. 12, no. 12, pp. 8861–8876, 2012, doi: 10.3390/s120708861.

[83] R. Kashyap, *Fiber Bragg Gratings*. 2010.

[84] A. Yariv and P. Yeh, *Photonics: optical electronics in modern communications*, no. 6th. 2007.

[85] R. Kashyap, *Fiber Bragg Gratings*. .

[86] G. D. Marshall, R. J. Williams, N. Jovanovic, M. J. Steel, and M. J. Withford, “Point-by-point written fiber-Bragg gratings and their application in complex grating designs,” *Opt. Express*, vol. 18, no. 19, pp. 1864–1866, 2010.

[87] T. A. B. Artulevicius *et al.*, “Compact fiber CPA system based on a CFBG stretcher and CVBG compressor with matched dispersion profile,” *Opt. Express*, vol. 25, no. 17, pp. 22806–22812, 2017.

[88] N. M. Litchinitser, M. Sumetsky, and P. S. Westbrook, “Fiber-based tunable dispersion compensation,” *Opt. fiber Commun. Rep.*, vol. 4, pp. 41–85, 2007, doi: 10.1007/s10297-006-0072-6.

[89] X. Wang, W. Shi, R. Vafaei, N. a F. Jaeger, and L. Chrostowski, “Uniform and sampled Bragg gratings in SOI strip waveguides with sidewall corrugations,” *IEEE Photonics Technol. Lett.*, vol. 23, no. 1, pp. 290–292, 2011, doi: 10.1109/LPT.2010.2103305.

[90] H. Grün, T. Berer, P. Burgholzer, R. Nuster, and G. Paltauf, “Three-dimensional photoacoustic imaging using fiber-based line detectors.,” *J. Biomed. Opt.*, vol. 15, no. 2, p. 021306, 2010, doi: 10.1117/1.3381186.

[91] G. Wissmeyer, D. Soliman, R. Shnaiderman, A. Rosenthal, and V. Ntziachristos, “All-optical optoacoustic microscope based on wideband pulse interferometry,” *Opt. Lett.*, vol. 41, no. 9, p. 1953, 2016, doi: 10.1364/OL.41.001953.

[92] M. Rattier *et al.*, “Performance of waveguide-based two-dimensional photonic-crystal mirrors studied with Fabry-Perot resonators,” *IEEE J. Quantum Electron.*, vol. 37, no. 2, pp. 237–243, 2001, doi: 10.1109/3.903074.

[93] P. Prabhathan, V. M. Murukeshan, and Z. Jing, “Compact SOI nanowire refractive index sensor using phase shifted Bragg grating,” *Opt. Express*, vol. 17, no. 17, pp. 1488–1490, 2009, [Online]. Available: Br.

[94] C. Chao, S. Ashkenazi, S. Huang, M. O. Donnell, and L. J. Guo, “High-Frequency Ultrasound Sensors Using Polymer Microring Resonators,” *IEEE Trans. Ultrason. Ferroelectr. Freq. Control*, vol. 54, no. 5, pp. 957–965, 2007.

[95] B. Dong, C. Sun, and H. Zhang, “Optical detection of ultrasound in photoacoustic imaging,” *IEEE Trans. Biomed. Eng.*, vol. 64, no. 1, pp. 4–15, 2017, doi: 10.1109/TBME.2016.2605451.

[96] P. C. Beard, “Transduction mechanisms of the Fabry-Perot polymer film sensing concept for wideband ultrasound detection,” *IEEE Trans. Ultrason. Ferroelectr. Freq. Control*, vol. 46, no. 6, pp. 1575–1582, 1999, doi: 10.1109/58.808883.

[97] R. Shnaiderman, G. Wissmeyer, O. Ülgen, Q. Mustafa, A. Chmyrov, and V. Ntziachristos, “A submicrometre silicon-on-insulator resonator for ultrasound detection,” *Nature*, vol. in press, doi: 10.1038/s41586-020-2685-y.

[98] J. David and N. Cheeke, *Fundamentals and Applications of Ultrasonic Waves Fundamentals and Applications of Ultrasonic Waves*. 2002.

[99] P. K. Köstl, F. Martin, B. Hans, and W. P. Heinz, “Temporal backward projection of optoacoustic pressure transients using Fourier transform methods,” *Phys. Med. Biol.*, vol. 46, pp. 1863–1872, 2001.

[100] M. Omar *et al.*, “Optical imaging of post-embryonic zebrafish using multi orientation raster scan optoacoustic mesoscopy,” *Light Sci. Appl.*, vol. 6, no. 1, pp. e16186–e16186, Jan. 2017, doi: 10.1038/lsa.2016.186.

[101] X. Huang, J. H. a. Cheong, H. K. Cha, H. Yu, M. Je, and H. Yu, “A high-frequency transimpedance amplifier for CMOS integrated 2D CMUT array towards 3D ultrasound imaging,” in *Proceedings of the Annual International Conference of the IEEE Engineering in Medicine and Biology Society, EMBS*, 2013, vol. 2013, pp. 101–104, doi: 10.1109/EMBC.2013.6609447.

[102] W. D. Sacher *et al.*, “Monolithically Integrated Multilayer Silicon Nitride-on-Silicon Waveguide Platforms for 3-D Photonic Circuits and Devices,” *Proc. IEEE*, vol. 106, no. 12, 2018, doi: 10.1109/JPROC.2018.2860994.

[103] E. A. ASH and G. NICHOLLS, “Super-resolution Aperture Scanning Microscope,” *Nature*, vol. 237, no. 5357, pp. 510–512, Jun. 1972, doi: 10.1038/237510a0.

[104] A. Harootunian, E. Betzig, M. Isaacson, and A. Lewis, “Super-resolution fluorescence near-field scanning optical microscopy,” *Appl. Phys. Lett.*, vol. 49, no. 11, pp. 674–676, 1986, doi: 10.1063/1.97565.

[105] B. T. Khuri-Yakub, S. Akamine, B. Hadimioglu, H. Yamada, and C. F. Quate, “Near-field acoustic microscopy (Invited Paper),” in *Proc. SPIE 1556, Scanning Microscopy Instrumentation*, Feb. 1992, vol. 1556, pp. 30–39, doi: 10.1117/12.134885.

[106] A. Kulik, J. Attal, and G. Gremaud, *Nearfield Scanning Acoustic Microscopy*, vol. 20. Springer US, 1993.

[107] G. S. Shekhawat, “Nanoscale Imaging of Buried Structures via Scanning Near-Field Ultrasound Holography,” *Science (80-.).*, vol. 310, no. 5745, pp. 89–92, Oct. 2005, doi: 10.1126/science.1117694.

[108] P. Ahn, Z. Zhang, C. Sun, and O. Balogun, “Ultrasonic near-field optical microscopy using a plasmonic nanofocusing probe,” *J. Appl. Phys.*, vol. 113, no. 23, 2013, doi: 10.1063/1.4810925.

[109] S. K. Selvaraja, W. Bogaerts, P. Dumon, D. Van Thourhout, and R. Baets, “Subnanometer Linewidth Uniformity in Silicon Nanophotonic Waveguide Devices Using CMOS Fabrication Technology,” *IEEE J. Sel. Top. Quantum Electron.*, vol. 16, no. 1, pp. 316–324, Jan. 2010, doi: 10.1109/JSTQE.2009.2026550.

[110] Y. Shacham-Diamand, A. Inberg, Y. Sverdlov, and N. Croitoru, “Electroless silver and silver with

tungsten thin films for microelectronics and microelectromechanical system applications," *J. Electrochem. Soc.*, vol. 147, no. 9, pp. 3345–3349, 2000, doi: 10.1149/1.1393904.

[111] E. M. Strohm, E. S. L. Berndl, and M. C. Kolios, "High frequency label-free photoacoustic microscopy of single cells," *Photoacoustics*, vol. 1, no. 3–4, pp. 49–53, 2013, doi: 10.1016/j.pacs.2013.08.003.

[112] A. Rosenthal, D. Razansky, and V. Ntziachristos, "Wideband optical sensing using pulse interferometry.," *Opt. Express*, vol. 20, no. 17, pp. 19016–29, 2012, doi: 10.1364/OE.20.019016.

[113] R. Diekmann *et al.*, "Chip-based wide fi eld-of-view nanoscopy," *Nat. Photonics*, vol. 11, pp. 322–328, 2017, doi: 10.1038/nphoton.2017.55.

[114] X. Y. Han *et al.*, "Recent progress of imprinted polymer photonic waveguide devices and applications," *Polymers (Basel).*, vol. 10, no. 6, 2018, doi: 10.3390/polym10060603.

[115] J. Schrauwen, D. Van Thourhout, and R. Baets, "Trimming of silicon ring resonator by electron beam induced compaction and strain," *Opt. Express*, vol. 16, no. 6, p. 3738, Mar. 2008, doi: 10.1364/OE.16.003738.

[116] J. E. Cunningham *et al.*, "Highly-efficient thermally-tuned resonant optical filters," *Opt. Express*, vol. 18, no. 18, p. 19055, 2010, doi: 10.1364/oe.18.019055.

[117] E. M. Strohm, M. J. Moore, and M. C. Kolios, "High resolution ultrasound and photoacoustic imaging of single cells," *Photoacoustics*, vol. 4, no. 1, pp. 36–42, Mar. 2016, doi: 10.1016/j.pacs.2016.01.001.

[118] R. Shnaiderman, G. Wissmeyer, O. Ülgen, Q. Mustafa, A. Chmyrov, and V. Ntziachristos, "A submicrometre silicon-on-insulator resonator for ultrasound detection," *Nature*, vol. 585, no. July 2018, 2020, doi: 10.1038/s41586-020-2685-y.